学 位 論 文

Dual inhibition of GPx4 and MEK

suppresses pancreatic ductal adenocarcinoma

by inducing ferroptosis

（GPx4 と MEK の共阻害によるフェロトーシス

誘導を介した膵管腺がんの抑制）

2025 年 9 月

北海道大学

JIANG HUI

ショウ　キ

学 位 論 文

Dual inhibition of GPx4 and MEK

suppresses pancreatic ductal adenocarcinoma

by inducing ferroptosis

（GPx4 と MEK の共阻害によるフェロトーシス

誘導を介した膵管腺がんの抑制）

2025 年 9 月

北海道大学

JIANG HUI

ショウ　キ

Contents

List of Publications and Presentations

Part of this research has been published in the following papers:

1. Hui Jiang, Taku Kimura, Han Hai, Ryodai Yamamura and Masahiro Sonoshita. (2022) *Drosophila* as a toolkit to tackle cancer and its metabolism. Frontiers in Oncology, 12:982751.

2. Hui Jiang, Yusuke Satoh, Ryodai Yamamura, Takako Ooshio, Yang Luo, Han Hai, Takuya Otsuka, Soichiro Hata, Reo Sato, Taiga Hirata, Tsuyoshi Osawa, Keisuke Goda and Masahiro Sonoshita. Inhibition of NAD-GPx4 axis and MEK triggers ferroptosis to suppress pancreatic ductal adenocarcinoma. Molecular Therapy, in Press.

Summary

[Background and Objectives]

Pancreatic ductal adenocarcinoma (PDAC) is a highly aggressive malignancy with a 5-year survival rate of only 10%. Due to late diagnosis, surgical resection is optional for only 20% of patients, while chemotherapy and radiation demonstrate limited efficacy because of poor response rates and high toxicity. This emphasizes the urgent need for novel treatment regimens.

Traditional approaches in drug development using cell cultures and mouse models have notable limitations: cultured cells often fail to replicate dynamic microenvironments within the body, while mouse models are costly and time-consuming. In contrast, *Drosophila melanogaster*, the fruit fly, serves as a complementary platform, offering a cost-effective and time-efficient whole-body organism. To investigate PDAC, we developed a '*4-hit*' *Drosophila* model that mirrors genetic alterations of *KRAS*, *TP53*, *CDKN2A*, and *SMAD4*, which are observed in a patient population with the poorest clinical outcome among PDAC patients.

Using the *4-hit* flies, we discovered that reducing the gene dosage of *Riboflavin kinase* (*RFK*) improved the survival of *4-hit* flies, highlighting the significance of riboflavin (RF, also known as vitamin B2) in PDAC. RF and its metabolized forms, flavin mononucleotide (FMN) and flavin adenine dinucleotide (FAD), are critical for metabolic redox and the metabolism of other B vitamins. Hence, I hypothesize that RF-related vitamin metabolism plays a key role in PDAC pathogenesis, although its detailed mechanisms remain unclear. This study aims to identify vitamin metabolism pathways involved in PDAC progression and explore their potential as therapeutic targets.

[Materials and methods]

To investigate vitamin metabolism (VM) pathways in PDAC, I performed genetic screening using *Serrate* (*Ser*) driver-induced *4-hit* flies (*Ser>4-hit*), introducing either heterozygous mutation or siRNA for each VM-related gene. I compared the viability of resulting offspring with that of control flies to identify potential therapeutic targets.

After identifying potential targets, I focused on developing therapeutic strategies for PDAC. I conducted chemical testing by adding small-molecule inhibitors targeting the candidate targets, either alone or in combination with the MEK inhibitor trametinib, into the food for *Ser>4-hit* flies. I compared the viability of *Ser>4-hit* flies treated with these chemicals to that of the vehicle group. I also identified GPx4 as a potential therapeutic target and the combination of ML210, a GPx4 inhibitor, and trametinib as a novel therapeutic strategy. To investigate the role of GPx4 in PDAC, I used RNA interference in human PDAC cells and evaluated the impact of *GPx4* knockdown on cell proliferation.

Given the GPx4's involvement in GSH (glutathione) metabolism and its role in ferroptosis, I assessed its clinical relevance in human PDAC by single-cell RNA sequencing (scRNA-seq). I obtained scRNAseq gene-barcode matrices from Gene Expression Omnibus (GEO) and examined the relative expression of genes involved in GSH metabolism, including *GPx4*, across cell clusters and calculated module scores for GSH metabolism and ferroptosis evaluating the susceptibility of PDAC to GSH interference and ferroptosis induction.

To validate efficacy of ML210 and its combination with trametinib, I employed cultured human PDAC cells. Human PDAC cell lines AsPC-1, Capan-1, and Panc-1 were cultured in spheroid and soft agar assays, and then treated with ML210 and trametinib. Additionally, an orthotopic xenograft mouse model was developed by inoculating AsPC-1 cells labeled with luciferase (AsPC-1-Luc) into the pancreas of immunodeficient mice. Subsequently, the mice were treated with 10 or 40 mg/kg of

ML210 intraperitoneally and/or 0.5 mg/kg trametinib orally for four weeks. Tumor progression was monitored weekly via bioluminescence imaging with luciferin.

Finally, I determined the type of cell death that the treatment induces using the ferroptosis inhibitor Ferrostatin-1 (Fer-1) and the iron chelator Deferoxamine mesylate (DFO). Flow cytometry was used to measure reactive oxygen species (ROS) and iron levels in human PDAC cells. I also evaluated the anti-tumor mechanisms of the seed through immunohistochemical (IHC) and immunofluorescence (IF) staining of tumor samples in mice.

[Results]

I identified 23 VM-related genes whose functional deficiencies rescued the lethality of *Ser>4-hit* flies, indicating their potential as therapeutic targets for PDAC. Notably, 10 of these 23 genes, including GPx4, are part of NAD synthesis pathway, highlighting the critical role of the vitamin B3 (VB3) metabolism pathway in regulating *Ser>4-hit* fly viability. In chemical testing, ML210, a covalent GPx4 inhibitor, significantly improved the survival of *Ser>4-hit* flies when combined with the MEK inhibitor drug trametinib, highlighting GPx4 as a compelling therapeutic target. In human AsPC-1 cells, knockdown of *GPx4* reduced spheroid growth, which was more pronounced in the presence of trametinib.

Additionally, scRNAseq analysis of human PDAC samples revealed high GPx4 expression in cancer epithelial cells. These cells also scored significantly higher in both GSH and ferroptosis modules, indicating that cancer epithelial cells are particularly vulnerable to ferroptosis induction in PDAC.

In soft agar assays, the combination of ML210 and trametinib (hereafter abbreviated as MT), significantly reduced the number and size of AsPC-1 colonies compared to ML210 monotherapy. Similarly, in spheroid assay, MT displayed strong inhibitory effects on PDAC spheroids across various concentration combinations.

Moreover, MT significantly suppressed tumor growth in mice with orthotopically implanted AsPC-1 cells compared to monotherapy.

Lastly, it is confirmed that GPx4 and MEK dual inhibition induces ferroptosis. Both Fer-1 and DFO inhibited tumor suppression in trametinib-treated *GPx4*-knockdown AsPC-1 cells. Additionally, Fer-1 and DFO rescued spheroid volume in AsPC-1 cells treated with either ML210 alone or MT. Consistently, MT elevated intracellular ROS and iron levels, effects that were mitigated by Fer-1 or DFO. In mouse xenograft tumors, IF staining of lipid peroxidation marker 4-hydroxynonenal (4-HNE) supported that cancer cells underwent ferroptosis.

[Discussion]

This study identified the pro-tumorigenic role of NAD synthesis pathway in PDAC by genetic screening in *4-hit* flies. The activation of NAD synthesis presents a therapeutic vulnerability, consistent with previous studies linking *NAMPT* overexpression to poor PDAC prognosis.

Moreover, genetic and chemical screening in *Ser>4-hit* flies reinforced the importance of GPx4 as a therapeutic target. GPx4 prevents ferroptosis, an iron-dependent form of cell death driven by lipid peroxidation. Inducing ferroptosis presents a promising strategy for treating PDAC, particularly in drug-resistant cancer cells. However, ferroptosis in PDAC might also harm immune cells, weakening the anti-tumor response. Dual inhibition of GPx4 and MEK could be useful to solve this issue, as MEK inhibition increases iron levels, sensitizing PDAC cells to ferroptosis. Since previous studies have outlined strategies counteracting immunosuppression triggered by ferroptosis, we speculate that the combination of dual GPx4 and MEK inhibition with immunosuppressive countermeasures is a promising strategy to treat PDAC.

[Conclusion]

This research establishes GPx4 as a therapeutic target and demonstrate that dual inhibition of GPx4 and MEK induces ferroptosis, offering a promising treatment strategy for PDAC. The findings demonstrate the versatility and utility of our *Drosophila* screening platform substantiated by mammalian models in developing novel therapeutic approaches for cancer treatment.

List of Abbreviations

4-HNE	4-hydroxynonenal
5-FU	5-fluorouracil
AFMID	*Arylformamidase*
AHR	*Aryl hydrocarbon Receptor*
BDSC	Bloomington *Drosophila* Stock Center
CC3	cleaved caspase 3
Cys-fs	cysteine to frameshift
DAPI	4',6-diamidino-2-phenylindole
DCFH-DA	dichlorodihydrofluorescein diacetate
dCycE	*Drosophila Cyclin E*
DFO	Deferoxamine mesylate
DMSO	dimethyl sulfoxide
dRas	*Drosophila Rat sarcoma viral oncogene*
EGFR	Epidermal growth factor receptor
FAD	flavin adenine dinucleotide
Fer-1	Ferrostatin-1
FFPE	formalin-fixed paraffin-embedded
FMN	flavin mononucleotide
FOLFIRINOX	the combination of 5-FU, leucovorin, irinotecan and oxaliplatin
FP	flavoprotein
G12D	G to D missense mutation in *KRAS* or *dRas*
GEMM	genetically engineered mouse model
GEO	Gene Expression Omnibus
GPx4	Glutathione peroxidase 4
GSH	glutathione
GSK3	Glycogen synthase kinase 3
GSSG	glutathione disulfide
GTEx	Genotype-Tissue Expression
H&E	Hematoxylin and eosin
IF	immunofluorescence

IHC	immunohistochemistry
KMO	Kynurenine 3-monooxygenase
LOF	loss of function
MCP	Macrophage-capping protein
Med	*Medea*
MEK	Mitogen-activated extracellular signal-regulated kinase
MSI-H	microsatellite instability-high
MSR	Methionine synthase reductase
MT	the combination of ML210 and trametinib
MTD	maximum tolerated dose
MTHFR	N-5,10-methylene-tetrahydrofolate reductase
MTRR	Methionine synthase reductase
NA	nicotinic acid
nab-paclitaxel	nanoparticle albumin-bound paclitaxel
NAC	N-acetyl cysteine
NAD	nicotinamide adenine dinucleotide
NADK	*NAD Kinase*
NADSYN1	*NAD synthetase 1*
NAMPT	Nicotinamide phosphoribosyltransferase
Naprt	*Nicotinate phosphoribosyltransferase*
NM	nicotinamide
Nmnat	*Nicotinamide mononucleotide adenylyltransferase*
PanIN	pancreatic intraepithelial neoplasia
Parp	*Poly-(ADP-ribose) polymerase*
PBS	phosphate-buffered saline
PCA	principal component analysis
PDAC	Pancreatic ductal adenocarcinoma
PFA	paraformaldehyde
PMP oxidase	Pyridoxal 5’-phosphate oxidase
PNP oxidase	Pyridoxine 5’-phosphate oxidase
ptc	*patched*
RF	riboflavin
RFK	riboflavin kinase

ROS	reactive oxygen species
RTK	receptor tyrosine kinase
RT-qPCR	Reverse transcription-quantitative polymerase chain reaction
scRNA-seq	single-cell RNA sequencing
Ser	*Serrate*
Ser-Stop	serine to stop codon
shRNA	short hairpin ribonucleic acid
siRNA	small interfering ribonucleic acid
Sirt1	*Sirtuin 1*
SOX2	*SRY-Box Transcription Factor 2*
SoxN	*SoxNeuro*
Tb	*Tubby*
TCGA	The Cancer Genome Atlas
TDO	*Tryptophan 2,3-dioxygenase*
Thr-fs	threonine to frameshift
tub	*tubulin*
UAS	*Upstream activation sequence*
v	*vermilion*
VB3	vitamin B3
VDRC	Vienna *Drosophila* Resource Center
VM	vitamin metabolism
w^-	*white*$^-$
Wt	wild-type
β-NADP	β-nicotinamide adenine dinucleotide phosphate

Introduction

Pancreatic ductal adenocarcinoma (PDAC) is an aggressive and deadly malignancy with a 5-year survival rate of only 12% (Siegel *et al.*, 2023). Globally, PDAC ranks 14th in incidence but is the 7th leading cause of cancer-related deaths (Sung *et al.*, 2021). Moreover, it is projected to overtake colorectal cancer and become the second leading cause of cancer-derived death before 2040 in the United States (Rahib *et al.*, 2021). As treatment strategies for PDAC, surgery and chemotherapy are the primary options (Halbrook *et al.*, 2023). However, though surgical resection offers the best chance for improved prognosis, 80% of patients are ineligible for surgery due to late-stage diagnosis resulting from non-specific early symptoms (Kleeff *et al.*, 2016). On the other hand, the first-line therapy for systemic chemotherapy includes the combination of 5-fluorouracil (5-FU), leucovorin, irinotecan, and oxaliplatin (FOLFIRINOX), and the combination of gemcitabine and an albumin nanoparticle conjugate of paclitaxel (nab-paclitaxel). While these regiments have better anti-pancreatic cancer efficacy than conventional gemcitabine monotherapy, they are also associated with the higher incidence of adverse events, limiting the benefit to patients (Conroy *et al.*, 2011) (Von Hoff *et al.*, 2013). In recent years, PDAC research has increasingly focused on targeted therapies and immunotherapies. However, neither approach has yet yielded significant advancements in PDAC treatment. For instance, the addition of the Epidermal growth factor receptor (EGFR) inhibitor erlotinib to gemcitabine showed only marginal improvement in patient survival compared to gemcitabine alone (Moore et al., 2007). Furthermore, immune checkpoint inhibitors have had limited success due to the low percentage of PDAC patients with microsatellite instability-high (MSI-H), a critical biomarker for immunotherapy response, which occurs in only 1-2% of cases (Luchini et al., 2021). Given these limitations, drug discovery for PDAC remains a considerable challenge, underscoring the urgent need for innovative therapeutic strategies to address this unmet clinical need.

Pre-clinical research aimed at developing anti-cancer drugs always utilizes

mammalian cancer models, such as cultured cancer cells and mice. Historically, evaluating gene functions and drug candidates mainly relied on cytotoxicity assays using established cancer cell lines. This approach has significantly advanced our understanding of tumor biology and has driven research into anticancer drug discovery and development (Sams-Dodd, 2005). Meanwhile, mouse models, particularly genetically engineered mouse models (GEMMs), have been instrumental in elucidating the systemic mechanisms of PDAC. For instance, it has been demonstrated in GEMMs that oncogenic *KRAS* drives the formation of pancreatic intraepithelial neoplasia (PanIN) (Hingorani et al., 2003), and when combined with *TP53* mutations, leads to invasive and metastatic cancer (Hingorani et al., 2005). However, both cultured cells and mouse models have notable limitations. Namely, cultured cells often fail to replicate the dynamic tumor microenvironment, and the complex organ-organ interactions present in the human body, which may partially account for the high rate of clinical trial failures, despite promising preclinical results (Sams-Dodd, 2005). Mouse models, on the other hand, are costly, time-consuming, and require substantial research resources. These limitations hinder the progress in understanding PDAC pathogenesis and in developing effective treatments. Thus, establishing more predictive cancer models with better efficiency to evaluate current and future chemotherapeutics is of high priority.

To address the limitations, our lab has developed a new research platform using *Drosophila melanogaster* (the fruit fly) for drug screening. This platform complements conventional experimental systems by offering several distinct advantages. First, flies offer a whole-body, quick, cheap and efficient assay platform (Yamamura et al., 2021; Pandey and Nichols, 2011; Bier, 2005). Second, they share a high genetic conservation with mammals, including 75% of human disease-related genes (Jiang et al., 2022). Moreover, previous studies have confirmed significant similarities in drug responses between mammals and flies (Sonoshita et al., 2018; Ung et al., 2019; Lam Wong and Verheyen, 2021; Sekiya et al., 2023; Fukuda et al., 2024). These advantages have led to the development of novel fly models that replicate the genetic alterations of various

cancers, including lung, colorectal, and oral cancers, facilitating the identification of therapeutic targets and potential drug candidates (Levine and Cagan, 2016; Bangi et al., 2019, 2021). Notably, our lab has integrated assays from both mammalian and *Drosophila* models to explore cancer mechanisms and to develop novel drug candidates, including the rational modification of approved kinase inhibitor drugs (Sonoshita et al., 2018; Ung et al., 2019).

Based on this background, we established a novel whole-animal platform for PDAC research integrating *Drosophila* with mammalian models (Sekiya et al., 2023). It has been postulated that PDAC develops through the acquisition of somatic alterations in four key genes, including activation of the oncogene *KRAS* (with a frequency of 92%) and inactivation of the tumor suppressor genes *TP53* (65%), *CDKN2A* (67%), and *SMAD4* (49%) (Morris et al., 2010). Patients harboring mutations in all four gene alterations (hereafter referred to as *4-hit)* experience the poorest survival outcomes among PDAC patients (Qian et al., 2018). However, no whole-body animal model currently exists that fully recapitulates these four genetic alterations in the context of endogenous carcinogenesis.

To address this gap, our lab developed the "*4-hit* fly" the world's first animal model that mimics these four gene mutations in a whole-body system (Sekiya et al., 2023). In this model, *KRAS*^{G12D}, an activating mutation of *KRAS* was simulated by exogenously expressing the fly ortholog *Drosophila Ras* (*dRAS*^{G12D}), which carries a similar single base substitution. Additionally, *p53* (fly ortholog of *TP53*) and *Med* (fly ortholog of *SMAD4*) genes were knocked down using gene specific shRNA. As for *CDKN2A*, which lacks a fly ortholog, its function was mimicked by overexpressing *Drosophila Cyclin E* (*dCycE)* (Richardson et al., 1995) (Figure 1).

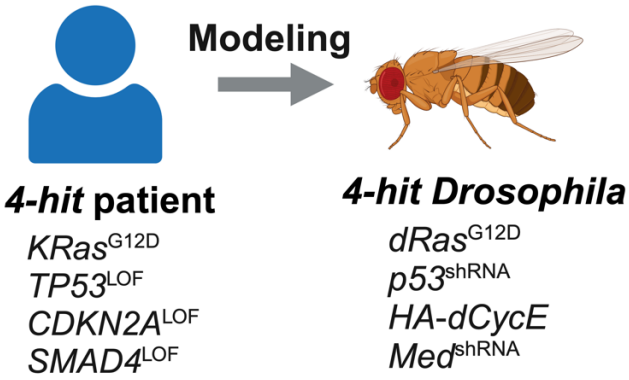

Figure 1. Modeling the four key gene mutations linked to poor prognosis in PDAC using *Drosophila*. We simulated *KRAS* activation by expressing *dRas*^{G12D}, knocked down *TP53* and *SMAD4* using gene-specific shRNA to create loss-of-function (LOF) mutations, and mimicked *CDKN2A* mutation by overexpressing *dCycE*. HA, hemagglutinin tag.

The *GAL4-Upstream Activating Sequence* (*UAS*) system, commonly used in *Drosophila* research (Duffy, 2002), was employed in this study to induce specific transgene expression. This system allows for controlled gene expression by crossing two fly strains: one carrying a *GAL4* driver gene and the other carrying a *UAS* element and gene under *UAS* control. The resulting offspring express the target gene of interest (Figure 2). The driver strain contains a gene encoding *GAL4*, a yeast-derived transcription factor whose activity is dependent on culture temperature. Moreover, *GAL4* can be induced in specific types of pf cells or tissues depending on the activity of an enhancer that drives its expression. On the other hand, the *UAS* strain carries a gene of interest downstream of the *UAS* sequence, where *GAL4* binds and induces the expression of the transgene (Yamamura et al., 2021). This system provides precise spatial and temporal control of gene expression, offering a valuable tool in *Drosophila* studies.

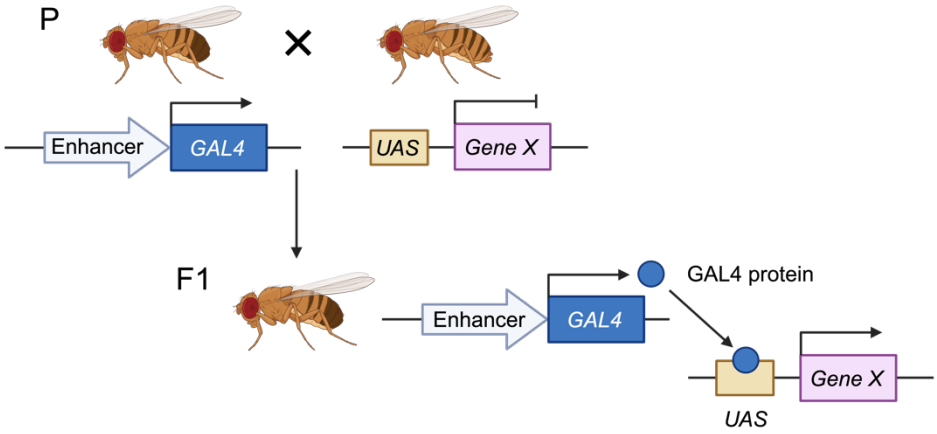

Figure 2. The crossing scheme of the *GAL4-UAS* system in *Drosophila*. This system enables targeted gene expression in specific cells or tissues, regulated by the activity of upstream activating sequences (UAS). It operates through the interaction between the yeast-derived transcription factor GAL4 and its target sequence and its corresponding UAS sites. The diagram illustrates the parental generation (P) and their offspring (F1), where specific gene expression occurs only in the F1 generation. The Figure was adapted from Yamamura et al., 2021.

Wing imaginal discs in *Drosophila* serve as a valuable tool to evaluate epithelial cell transformation driven by activation of the receptor tyrosine kinase (RTK)-Ras pathway (Vidal et al., 2005; Sonoshita et al., 2018; Ung et al., 2019). Based on this, our lab utilizes *patched* (*ptc*)-*GAL4* as a driver to specifically induce transgenes within a region of approximately ten cells wide at the center of the larval wing discs (hereafter referred to as the *ptc* domain) to analyze the proliferation and migration of transformed cells (Figure 3).

In control flies (*ptc>GFP*), which do not express transgenes, the *ptc* domain formed a distinct band appearance. However, in *ptc>1-hit* flies, where only the *dRas* gene was activated (*ptc-gal4*;*UAS-dRas*^{G12D}), I observed increased cell proliferation, accompanied by a significant widening of the *ptc* domain. Furthermore, in flies with the *4-hit* genotype (*ptc-gal4*;*UAS-dRas*^{G12D},*p53*^{shRNA},*HA-dCycE*, *Med*^{shRNA}), referred to as *ptc>4-hit* flies, proliferation of transformed cells was even more pronounced. Furthermore, some transformed cells migrated out of the *ptc* domain, indicating enhanced cellular migration (Figure 3) (Sekiya et al., 2023). In terms of survival, nearly all control flies can survive, while the survival rate of *ptc>1-hit* flies is reduced by half. Strikingly, the survival rate of *ptc>4-hit* flies was 0% (Figure 3) (Sekiya et al., 2023). These findings align with clinical observations that an accumulation of genetic mutations is associated with worsening patient prognosis (Qian et al., 2018). Based on these results, we propose that *4-hit* flies represent a novel animal model that mimics the genotype of human PDAC.

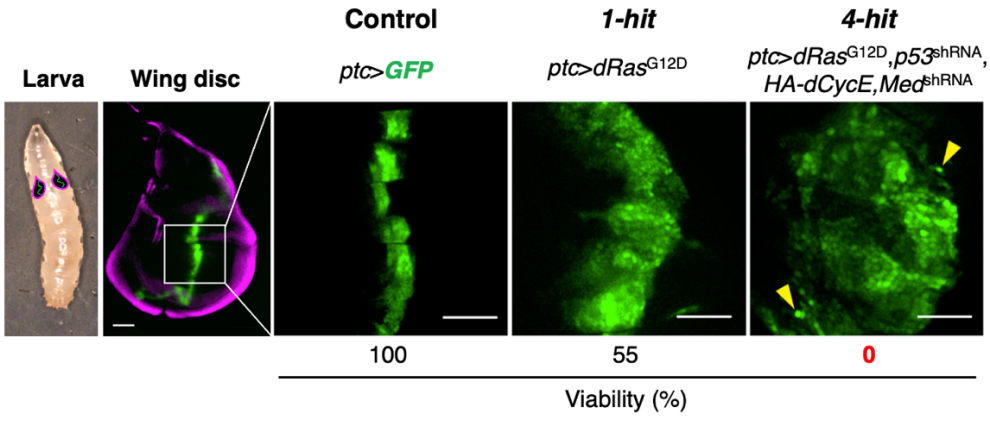

Figure 3. Genetic mutations promote phenotypic transformation in *Drosophila* wing discs. In larval wing discs (magenta outline), the *patched* (*ptc*) promoter was used to induce transgenes in a stripe of epithelial cells approximately ten cells wide (green: genetically modified cells labelled with GFP). The black regions represent wild-type cells. Activation of *dRas* alone (*1-hit*) caused increased cell proliferation, leading to a wider stripe. In contrast, wing discs from *4-hit* flies displayed a more disorganized pattern compared to $dRas^{G12D}$ flies, with enhanced cell migration (indicated by arrowheads). Fly survival was 100 % in control *ptc>GFP* flies, but 0% in *ptc>4-hit* flies. Scale bars, 50 μm. Figure was adapted from Sekiya et al., 2023.

Utilizing this model, we conducted a comprehensive genetic screening of the entire kinome, determining Mitogen-activated protein kinase kinase (MEK), Aurora kinase (AURKB), and Glycogen synthase kinase 3 (GSK3) as vulnerabilities in PDAC (Sekiya et al., 2023; Fukuda et al., 2024). Curiously, the screening also revealed riboflavin kinase (RFK), a kinase responsible for phosphorylating vitamin B2, as a potential therapeutic target alongside these protein kinases. In fact, inhibition of riboflavin metabolism by roseoflavin, a natural analog of riboflavin, in combination with the MEK inhibitor drug trametinib, suppressed the growth of human PDAC xenografts in mice (Ooshio et al., 2024). Riboflavin, a water-soluble vitamin, plays a crucial role as the precursor to flavin mononucleotide (FMN) and flavin adenine dinucleotide (FAD). These metabolites bind to flavoproteins (FPs), serving as coenzymes in electron transfer processes during catalytic cycles, and are essential for energy production and protection against oxidative stress (Barile et al., 2016). Of note, deficiency in riboflavin impairs oxidant defense mechanisms by disrupting the maintenance of reduced glutathione (GSH), the primary antioxidant in cells (Pinto and Zempleni, 2016).

FPs encompass many key proteins in vitamin metabolism pathways (Lienhart et al., 2013) (Figure 4). For example, Methylenetetrahydrofolate reductase (MTHFR) and Methionine synthase reductase (MSR) are key FPs in metabolism of folate (vitamin B9). MTHFR binds with FAD to produce N-5-methly-THF, while MSR binds with FMN to transfer a methyl group from N-5-methly-THF to homocysteine (Lienhart et al., 2013).

These FP functions highlight the potential roles of riboflavin metabolism in homeostasis and disease development, including cancers.

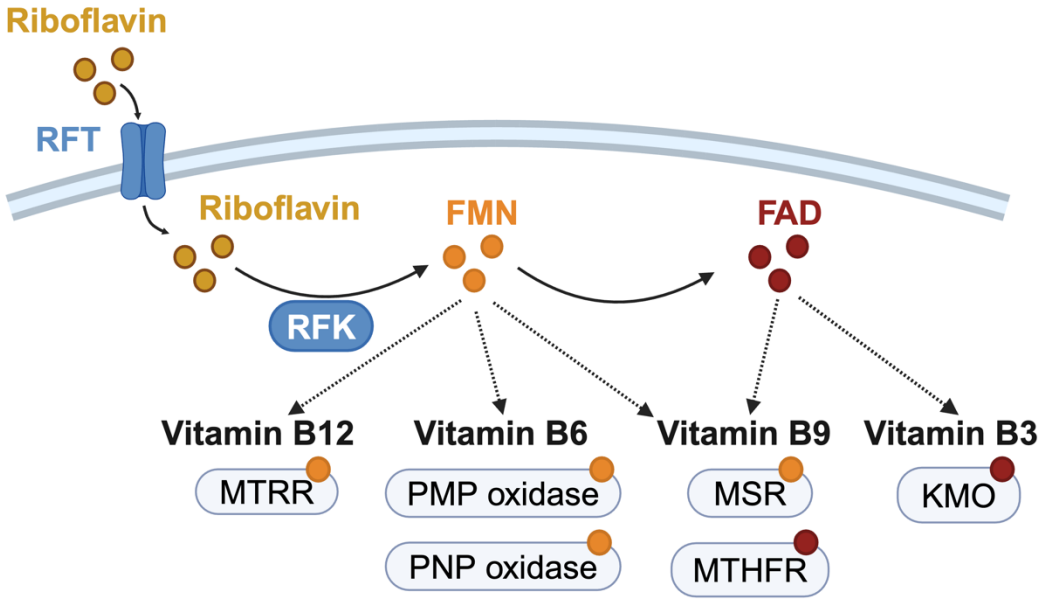

Figure 4. Schematic diagram of riboflavin metabolism leading to flavoproteins that regulate the metabolism of vitamins B3, B6, B9, and B12. Riboflavin is transported across the membrane via riboflavin transporter (RFT) and converted into its active forms, FMN and FAD, by riboflavin kinase (RFK). FMN and FAD serve as essential cofactors for enzymes involved in the metabolism of vitamins B3, B6, B9, and B12. MTRR, Methionine synthase reductase. PMP oxidase, Pyridoxal 5'-phosphate oxidase. PNP oxidase, Pyridoxine 5'-phosphate oxidase. MSR, Methionine synthase reductase. MTHFR, N-5,10-methylene-tetrahydrofolate reductase. KMO, Kynurenine 3-monooxygenase.

The involvement of vitamins in cancer has become a significant focus of recent research. For instance, nicotinic acid (NA) and nicotinamide (NM), collectively known as vitamin B3 (VB3), are integral to the biosynthesis and maintenance of nicotinamide adenine dinucleotide (NAD) levels in cells. Nicotinamide phosphoribosyltransferase (NAMPT)-mediated synthesis of NAD has been identified as a critical therapeutic target in various cancers, including colorectal and breast cancer. In fact, NAMPT inhibitors, such as FK866 and GMX1778, have demonstrated significant anti-cancer

potential by reducing NAD levels and inhibiting energy metabolism and cancer cell proliferation (Yaku et al., 2018).

Moreover, vitamin B9, also known as folate, has been identified as a vital cofactor for biochemical processes, including nucleotide, amino acid, and methyl group synthesis. Methotrexate, a common anti-folate chemotherapy, leads to widespread folate degradation and inhibits cell division (Zheng et al., 2018). Similarly, vitamin B6, in its active form pyridoxal 5'-phosphate (PLP), is essential for enzymatic reactions related to amino acid, glucose, and lipid metabolism (Galluzzi et al., 2013). Furthermore, pyridoxal kinase, which converts vitamin B6 into PLP, has been highlighted as a selective dependency in acute myeloid leukemia (Chen et al., 2020).

Despite the established roles of these vitamins in various cancers, the significance of vitamin metabolism in PDAC has not been fully explored. Hence, I aimed to bridge this gap by exploring the critical connections between riboflavin-related pathways and the pathogenesis of PDAC progression. My study underscored the importance of NAD synthesis pathway, leading to the identification of Glutathione peroxidase 4 (GPx4) as a distinct therapeutic target in PDAC.

Materials and Methods

Drosophila genetic screening

All fly studies were conducted using protocols approved by the Hokkaido University Safety Committee on Genetic Recombination Experiments (approval numbers: 2019-007 and 2022-029). Fly strains carrying gene mutations for whole-body gene disruption or small interfering RNA (siRNA) were obtained from Bloomington *Drosophila* Stock Center (BDSC; Bloomington, IL), KYOTO Stock Center (Kyoto, Japan), the National Institute of Genetics (Mishima, Japan), and Vienna *Drosophila* Resource Center (VDRC; Vienna, Austria) (Table 1).

Table 1. List of fly strains for functional screening of VM-related genes

CG No.	Fly gene	Human gene	RRID
CG6871	*Cat*	*CAT*	VDRC_103591
CG6871	*Cat*	*CAT*	BDSC_31894
CG6871	*Cat*	*CAT*	BDSC_4014
CG6871	*Cat*	*CAT*	BDSC_17939
CG14882	*CG14882*	*MTRR*	BDSC_56006
CG15116	*CG15116*	*GPx4*	BDSC_56992
CG15116	*CG15116*	*GPx4*	VDRC_106717
CG33156	*CG33156*	*NADK*	BDSC_62858
CG33156	*CG33156*	*NADK*	NIG_6152R-4
CG33156	*CG33156*	*NAKD*	VDRC_103902
CG33156	*CG33156*	*NADK*	BDSC_25470
CG3556	*CG3556*	*TCN1/2*	BDSC_65899
CG3556	*CG3556*	*TCN1/2*	NIG_3556R-1
CG3556	*CG3556*	*TCN1/2*	BDSC_19200
CG5946	*CG5946*	*CYB5R2*	BDSC_65007
CG5946	*CG5946*	*CYB5R2*	BDSC_35801
CG5946	*CG5946*	*CYB5R2*	VDRC_110688
CG6145	*CG6145*	*NADK*	NIG_6145R-1

CG6145	*CG6145*	*NAKD*	VDRC_104271
CG6145	*CG6145*	*NADK*	BDSC_42409
CG6739	*CG6739*	*CD320*	NIG_6739R-2
CG6739	*CG6739*	*CD320*	VDRC_108197
CG6993	*CG6993*	*AHR*	VDRC_108732
CG6993	*CG6993*	*AHR*	BDSC_19112
CG7560	*CG7560*	*MTHFR*	BDSC_64993
CG7560	*CG7560*	*MTHFR*	BDSC_57161
CG7560	*CG7560*	*MTHFR*	NIG_7560R-3
CG1555	*cn*	*KMO*	BDSC_268
CG43286	*cnc*	*Nrf2*	BDSC_40854
CG43286	*cnc*	*Nrf2*	BDSC_25984
CG2107	*CPT2*	*CPT2*	BDSC_51900
CG3131	*Doux1*	*DUOX1*	BDSC_38916
CG12529	*Gdh*	*GLUD1*	BDSC_51473
CG4233	*Got2*	*GOT2*	BDSC_78778
CG4233	*Got2*	*GOT2*	VDRC_106120
CG4233	*Got2*	*GOT2*	BDSC_33073
CG7176	*Idh*	*IDH*	BDSC_41708
CG7176	*Idh*	*IDH*	BDSC_4019
CG3962	*Keap1*	*Keap1*	BDSC_40932
CG3962	*Keap1*	*Keap1*	BDSC_57801
CG9542	*Kfase*	*AFMID*	NIG_9542R-2
CG9542	*Kfase*	*AFMID*	VDRC_109675
CG8609	*MED4*	*MMACHC*	BDSC_34697
CG10120	*Men*	*ME* (*123*)	BDSC_4025
CG9940	*Nadsyn*	*NADSYN1*	BDSC_62265
CG9940	*Nadsyn*	*NADSYN1*	NIG_9940R-1
CG9940	*Nadsyn*	*NADSYN1*	BDSC_43803
CG3714	*Naprt*	*NAMPT*	BDSC_61875
CG3714	*Naprt*	*NAMPT*	BDSC_62264
CG3714	*Naprt*	*NAMPT*	NIG_3714R-3
CG13645	*Nmnat*	*NMNAT*	BDSC_29402

CG13645	*Nmnat*	*NAPRT*	BDSC_53235
CG13645	*Nmnat*	*NMNAT*	BDSC_50493
CG34399	*Nox*	*NOX5*	BDSC_32433
CG40412	*Parp*	*PARP1*	BDSC_57265
CG40411	*Parp*	*PARP1*	NIG_GL00229
CG40411	*Parp*	*PARP1*	BDSC_34888
CG12013	*PHGPx*	*GPx4*	BDSC_33939
CG12013	*PHGPx*	*GPx4*	VDRC_100790
CG12013	*PHGPx*	*GPx4*	BDSC_41879
CG12013	*PHGPx*	*GPx4*	BDSC_25968
CG12013	*PHGPx*	*GPx4*	BDSC_28479
CG12306	*polo*	*PL kinase*	NIG_12306R-3
CG12306	*polo*	*PL kinase*	NIG_GL00014
CG12306	*polo*	*PL kinase*	VDRC_330025
CG31472	*sgll*	*PMPO*	BDSC_65207
CG31472	*sgll*	*PNP oxidase*	NIG_31472R-4
CG31472	*sgll*	*PNP oxidase*	VDRC_105941
CG5216	*Sirt1*	*SIRT1*	BDSC_31636
CG5216	*Sirt1*	*SIRT1*	NIG_5216R-1
CG5216	*Sirt1*	*SIRT1*	NIG_HMS00484
CG5216	*Sirt1*	*SIRT1*	BDSC_8838
CG11793	*Sod1*	*SOD*	BDSC_29389
CG11793	*Sod1*	*SOD1*	BDSC_24490
CG18024	*SoxN*	*SOX2*	NIG_18024R-1
CG18024	*SoxN*	*SOX2*	BDSC_25996
CG2151	*Trxr-1*	*GR*	BDSC_53883
CG2151	*Trxr-1*	*GSR*	BDSC_36805
CG2151	*Trxr-1*	*GR*	VDRC_110648
CG6186	*Tsf1*	*TFR1*	BDSC_62968
CG10620	*Tsf2*	*TFR2*	BDSC_65903
CG3666	*Tsf3*	*TFR3*	BDSC_56015
CG2155	*v*	*TDO*	NIG_2155R-1
CG2155	*v*	*TDO*	NIG_2155R-2

CG2155	*v*	*TDO*	NIG_HMC03041
CG2155	*v*	*TDO*	VDRC_107798
CG12529	*Zw*	*G6PD*	BDSC_50667

Fly strains lacking *Tubby* (*Tb*)-marked balancers were rebalanced using *FM7c-Tb-RFP*, *Cyo-Tb-RFP*, or *TM6B* balancers, all of which carry *Tb* as a visible marker (Sekiya et al., 2023) (Fukuda et al. *Cancer Sci* 2024). Subsequently, I crossed *Ser-gal4*,*UAS-4-hit* (*Ser>4-hit*) flies with these flies (Figure 5). The resulting progeny were cultured at 27°C until adulthood for 11 days, and percent viability was assessed by dividing the number of hatched pupae by the total number of pupae.

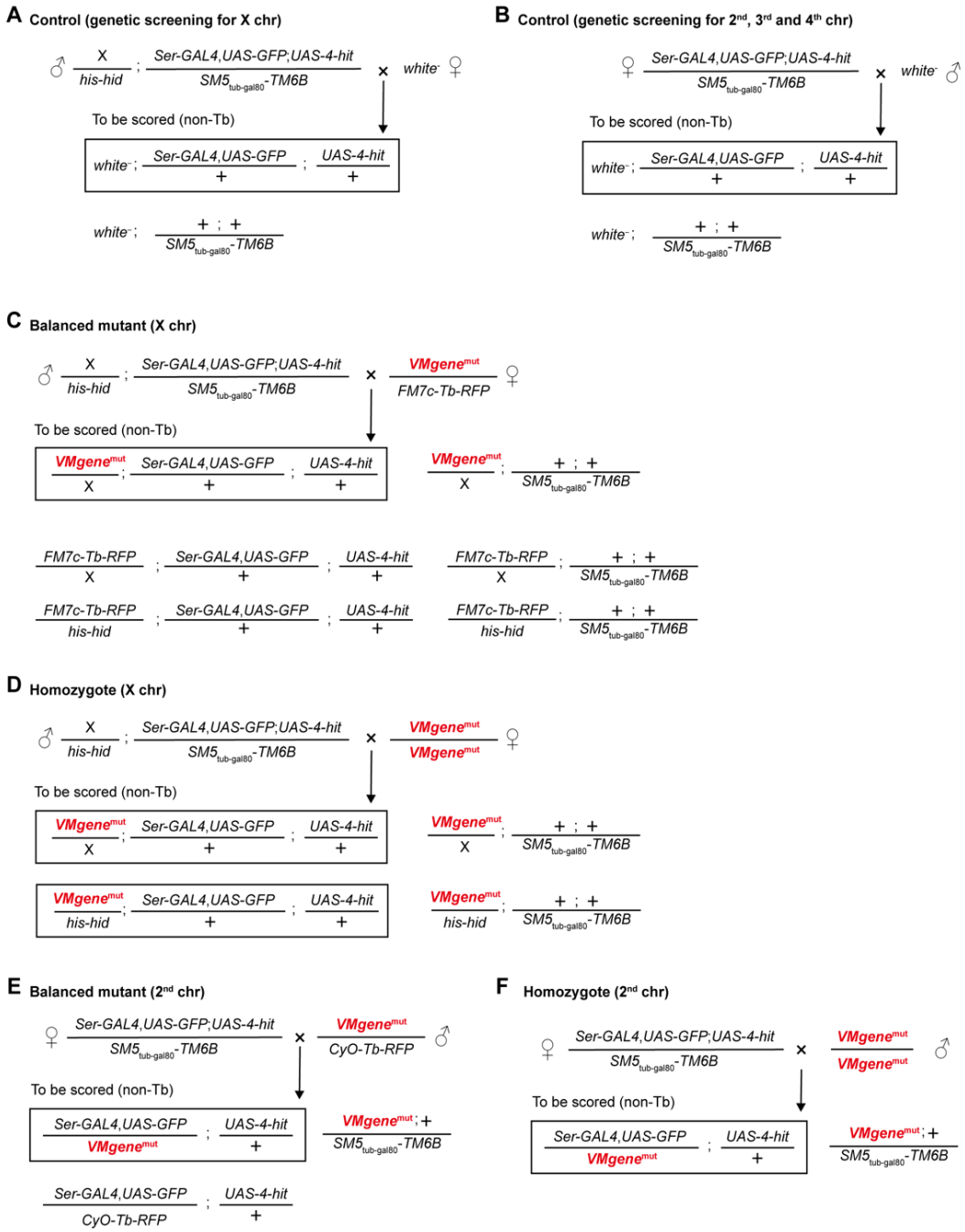

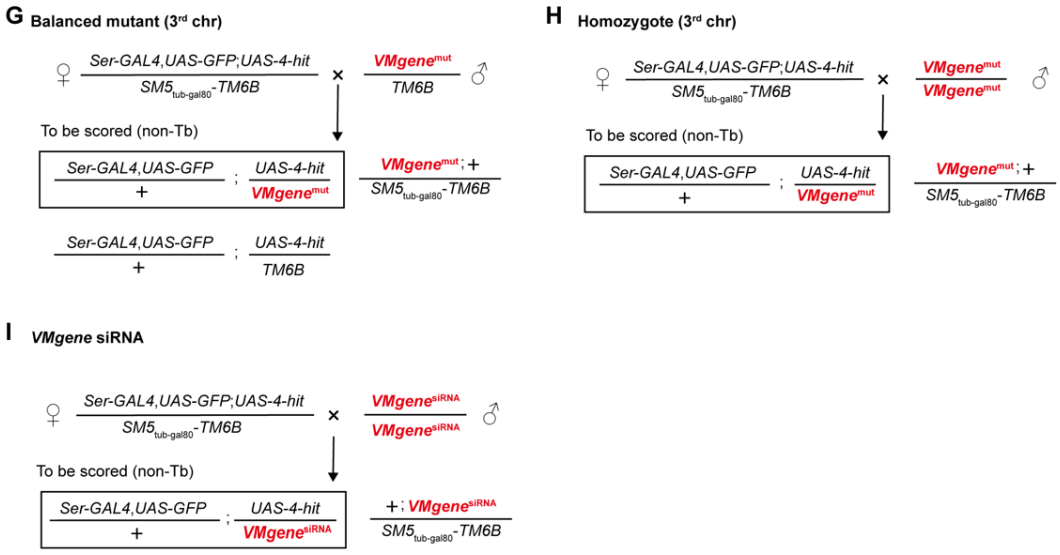

Figure 5. Schemes of fly crossing. (A-I) Generation of experimental flies for genetic screening. The *Ser>4-hit* flies were crossed with non-transgenic control flies **(A, B)** or with flies carrying mutations in a VM gene located on either the X **(C, D)**, 2nd **(E, F)**, 3rd **(G, H)** chromosome at 27°C. In parent flies, mutant alleles were either balanced with the *Tubby* (*Tb*) allele **(C, E, G)** or were homozygous **(D, F, H)**. *SM5tub-GAL80-TM6B*, attached balancer chromosome carrying GAL80 suppressor under the control of the *tubulin* (*tub*) enhancer. *hs-hid*, *hid* pro-apoptotic gene under the control of the heat-shock enhancer. mut, mutant **(I)** Generation of experimental flies with VM-gene knockdown. The viability of *Ser>4-hit* flies with reduced levels of a VM gene was compared to that of control flies.

Drosophila chemical testing

Chemicals were dissolved in dimethyl sulfoxide (DMSO, Sigma Aldrich, St. Louis, MO) or double-distilled water to prepare stock solutions based on their solubilities (Table 2).

Table 2. List of small molecular inhibitors in chemical testing.

Chemicals	SOURCE	IDENTIFIER
FK866 (NAMPT inhibitor)	MedChemExpress	Cat# HY-50876
OT-82 (NAMPT inhibitor)	MedChemExpress	Cat# HY-136241

2-HNA (NAPRT inhibitor)	TCI, Wako	Cat# H0795
STK459768 (NADSYN1 inhibitor)	Vitas M Lab	Cat# STK459768
Polydatin (G6PD inhibitor)	MedChemExpress	Cat# HY-N0120A
ML210 (GPx4 inhibitor)	MedChemExpress	Cat# HY-100003
RSL3 (GPx4 inhibitor)	MedChemExpress	Cat# HY-100218A
LCS1 (SOD1 inhibitor)	Sigma Aldrich	Cat# SML0466
2-ME2 (SOD1 inhibitor)	MedChemExpress	Cat# HY-12033
Tannic acid (NMNAT inhibitor)	Nacalai Tesque	Cat# 32616-02

Before screening, the maximum tolerated dose (MTD) of each chemical at a final DMSO concentration of 0.1% was determined by assessing viability of non-transgenic control w^- flies fed with the chemical (Sekiya et al., 2023; Fukuda et al., 2024). Virgin *UAS-4-hit* females were crossed with *Ser*-gal4 males to produce *Ser>4-hit* offspring, and their viability was assessed at 22°C (Figure 6).

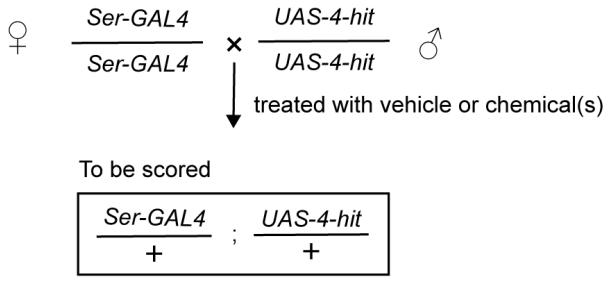

Figure 6. Schemes of fly crossing for chemical testing and wing malformation analysis. Crossing scheme for chemical testing. The progeny of *UAS-4-hit* flies and *Ser-GAL4* flies were raised on fly food containing vehicle or chemical(s) at 22℃

Adult wing malformation analyses

After preparing adult flies for analysis (Figure 7), adult wings were dissected, and wing sizes were quantified using the ImageJ software (National Institutes of Health, Bethesda, MD) (Fukuda et al., 2024).

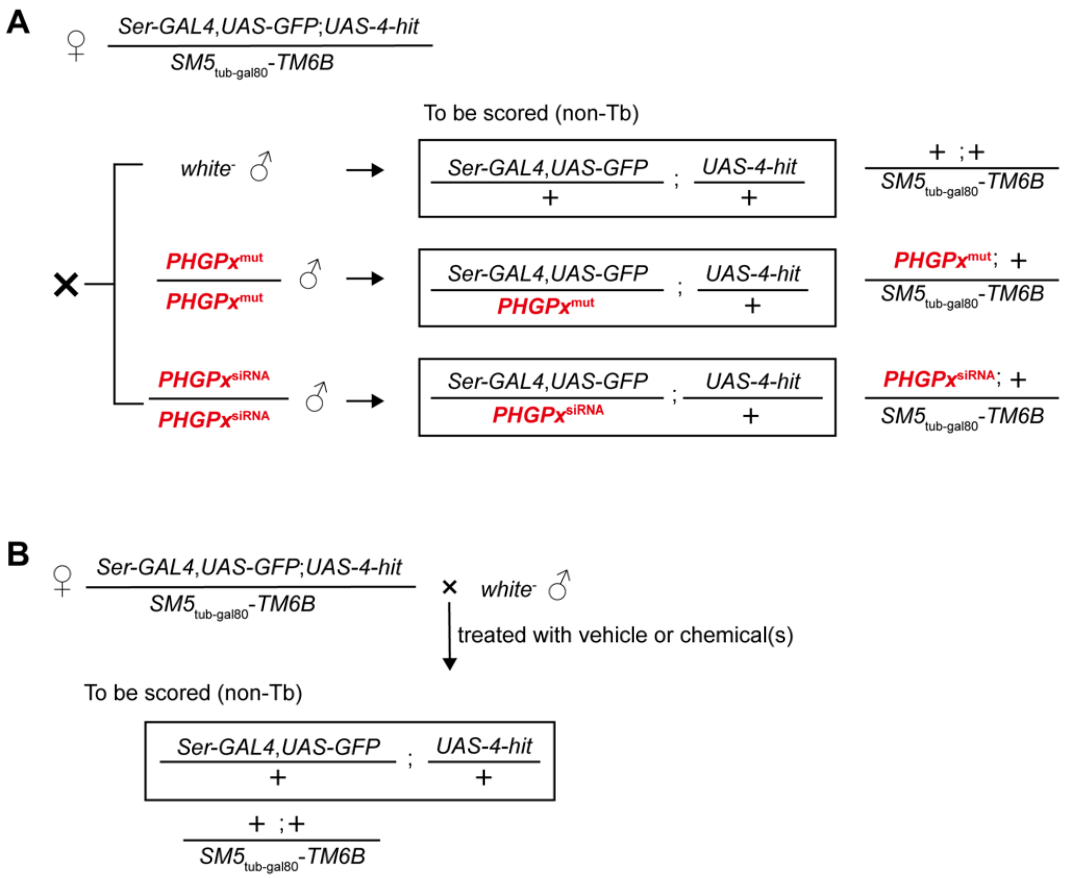

Figure 7. Schemes of fly crossing for chemical testing and wing malformation analysis. (A) Crossing scheme for wing malformation analysis of function deficiency of *PHGPx*. *Ser>4-hit* flies were crossed with either control (*white-*) or *PHGPx*-mutant flies, or flies carrying *PHGP*x siRNA at 27°C. **(B)** Crossing scheme for wing malformation analysis of chemical treatment. *Ser>4-hit* flies were crossed with control (*white-*) flies, and the progeny were raised on fly food containing either vehicle or chemical(s) at 27°C.

The development of VB3-deficient AsPC-1 cells

AsPC-1 cells were initially seeded in RPMI 1640 medium with 10% FBS (NICHIREI, Tokyo, Japan) and 1% Penicillin-Streptomycin Mixed Solution (Nacalai Tesque, Kyoto, Japan). After 24 hours, the medium was replaced with RPMI lacking NM. The cells were incubated in NM-deficient RPMI for 2 days. Following this incubation, the cells were passaged and further incubated for an additional 3 days in NM-deficient medium.

Subsequently, NM-deficient AsPC-1 cells were harvested for further analysis.

Maximum tolerated dose (MTD) assay in mice

MTD of ML210 and its combination with trametinib (MT) was determined using 13-week-old female BALB/c-*nu*/*nu* mice (RRID: IMSR_CRL:490, Sankyo Labo Service, Tokyo, Japan). Toxicity was assessed based on mortality and a 20% reduction in body weight compared to baseline. Five animals were assigned to each dose group. For the MTD assay of ML210, two dosing regimens were administered intraperitoneally. In the first group, mice received an initial dose of 0.1 mg/kg/day, which was gradually increased to a final dose of 2 mg/kg/day. In the second group, the initial dose was 5 mg/kg/day, increasing to a final dose of 80 mg/kg/day. For MTD assessment of MT combination, two groups received trametinib at a fixed oral dose of 0.5 or 1.0 mg/kg/day, alongside escalating doses of ML210, starting at 5 mg/kg/day and increasing to 40 mg/kg/day via intraperitoneal injection. Mice were treated once daily, five times a week, and monitored throughout the treatment period for signs of clinical distress, including weight loss, discharge, and morbidity (Sekiya et al., 2023; Fukuda et al., 2024).

Mouse pharmacokinetic assay

Pharmacokinetic assays for ML210 were conducted by Medicilon Preclinical Research (Shanghai, China). Six-week-old male ICR mice were administered a 10 mg/kg dose of ML210, and its plasma concentrations were measured at 0.083, 0.25, 0.5, 1, 2, 4, 8, and 24-hours post-dosing.

Mouse xenograft assay

All mouse studies were conducted under protocols approved by the Hokkaido University Safety Committee on Genetic Recombination Experiments (approval

number: 2022-029) and the Hokkaido University Animal Research Committee (approval numbers: 19-0121, 2022-0117, and 2022-0118). BALB/c-*nu/nu* mice (RRID:IMSR_CRL:490, Sankyo Labo Service) were housed under specific pathogen-free conditions on a 12:12 hours light:dark cycle. All surgical procedures were performed in mice anesthetized subcutaneously. Mice were anesthetized by subcutaneous administration of 15 mg/kg medetomidine (Kyoritsuseiyaku, Tokyo, Japan), 200 mg/kg midazolam (Astellas Pharma, Tokyo, Japan), and 250 mg/kg butorphanol tartrate (Meiji Seika Pharma, Tokyo, Japan). Anesthesia was reversed with 150 mg/kg of atipamezole (Kyoritsu Seiyaku) after the procedure. To develop an orthotopic PDAC mouse model, AsPC-1 cells transduced with *luciferase* cDNA (AsPC-1-Luc) (Fukuda et al., 2024) were harvested and injected into the exposed pancreas of 11-week-old female BALB/c-*nu*/*nu* mice (1×10^6 cells per mouse, suspended in 15 μl of Hanks' Balanced Salt Solution, Thermo Fisher Scientific, Waltham, MA). The mice were randomized into four groups (six mice per group) based on average tumor size, which was determined by bioluminescence imaging using IVIS Spectrum Imaging System (Caliper Life Science, Mountain View, MA) (Sekiya et al., 2023; Fukuda et al., 2024). The following treatment regimens were administered to the mice once daily, five times a week for four week: vehicle [5% DMSO in saline p.o. plus 10% Cremophor EL (Nacalai Tesque) and 5% DMSO in saline i.p.], ML210 (10 or 40 mg/kg/day i.p.), trametinib (0.5 mg/kg/day p.o.), and MT combination (ML210 10 or 40 mg/kg/day i.p. + trametinib 0.5 mg/kg/day p.o.). Bioluminescence signals were analyzed weekly using IVIS system and quantified with Living Image Ver.4.2 software (Caliper Life Science). Throughout the treatment period, mice were closely monitored for signs of acute toxicity, including weight loss, discharge, and morbidity. On or before day 21 after starting treatment, mice were euthanized for analyses following the endpoints approved by the Institutional Animal Care and Use Committee (IACUC): (i) animals showing signs of significant discomfort, (ii) ascites or overt signs of tumor metastasis or gastrointestinal bleeding (blood in stool), (iii) animals losing > 15% of their body weight, or (iv) animals with tumors > 2 cm in diameter.

Spheroid formation assay

AsPC-1 cells were suspended in 100 μL of culture medium and seeded into a U-shaped, cell-repellent 96-well plate (Cellstar 650970, Greiner, Kremsmünster, Austria). The cells were incubated for 72 hours to form spheroids. Following spheroid formation, 100 μL of RPMI 1640 medium containing either vehicle or chemical dissolved in DMSO was added to each well, ensuring a final DMSO concentration of 0.2%. After an additional 72-hour incubation, 100 μL of the medium containing the spheroids was carefully aspirated and transferred to opaque-walled 96-well plates (Thermo Fisher Scientific). Spheroid volume was assessed using CellTiter-Glo 3D Reagent (Promega, Madison, WI), and luminescence was measured using a microplate reader (Synergy LX Biotek, Winooski, VT). Relative spheroid volume was calculated by comparing the average luminescence value to that of vehicle control group. Each experiment was conducted in quintuplicate. ZIP synergy scores for the combination assay were calculated using SynergyFinder (version 3.4.5) in R.

Detection of intracellular ROS levels

Intracellular ROS levels were measured using dichlorodihydrofluorescein diacetate (DCFH-DA) (ROS Assay Kit-Highly Sensitive DCFH-DA, Dojindo Lab, Kumamoto, Japan) and CellROX™ Deep Red Reagent (Thermo Fisher Scientific). Firstly, AsPC-1 cells were seeded in 24-well plates at a density of 1×10^5 cells per well 24 hours prior to chemical treatment. After the indicated treatments, the cells were washed with phosphate-buffered saline (PBS) and incubated with DCFH-DA (1:1500 dilution) or CellROX™ Deep Red (1:500 dilution) in the dark at 37°C for 30 minutes. Following incubation, the cells were washed with PBS and harvested in RPMI 1640 medium. Fluorescence intensity was then measured using BD FACS Canto II flow cytometer (BD Biosciences, Franklin Lakes, NJ).

Detection of intracellular Fe^{2+} levels

Intracellular iron levels were measured using FerroOrange (Dojindo Lab). AsPC-1 cells were seeded in 24-well plates at a density of 1×10^5 cells per well 24 hours prior to chemical treatment. Following the specified treatments, cells were stained with 1 μM FerroOrange in serum-free RPMI 1640 medium and incubated in the dark at 37°C for 30 minutes. Fluorescence intensity was subsequently measured using BD FACS Canto II flow cytometer (BD Biosciences).

Wing disc analyses

After preparing third instar larvae for analysis (Figure 8), wing discs were dissected from body and fixed in 4% paraformaldehyde (PFA, Nacalai Tesque) at room temperature for 10 minutes. After fixation, wing discs were washed three times with PBS, each for 10 minutes, and then mounted on microscope slides in Vectashield Vibrance Antifade Mounting Medium containing 0.9 μg/mL 4',6-diamidino-2-phenylindole (DAPI, Vector Biolabs, Malvern, PA). The discs were subsequently imaged using Leica DMi8 microscope (Leica, Wetzlar, Germany), and the whole disc area and transformed area were quantified using ImageJ software.

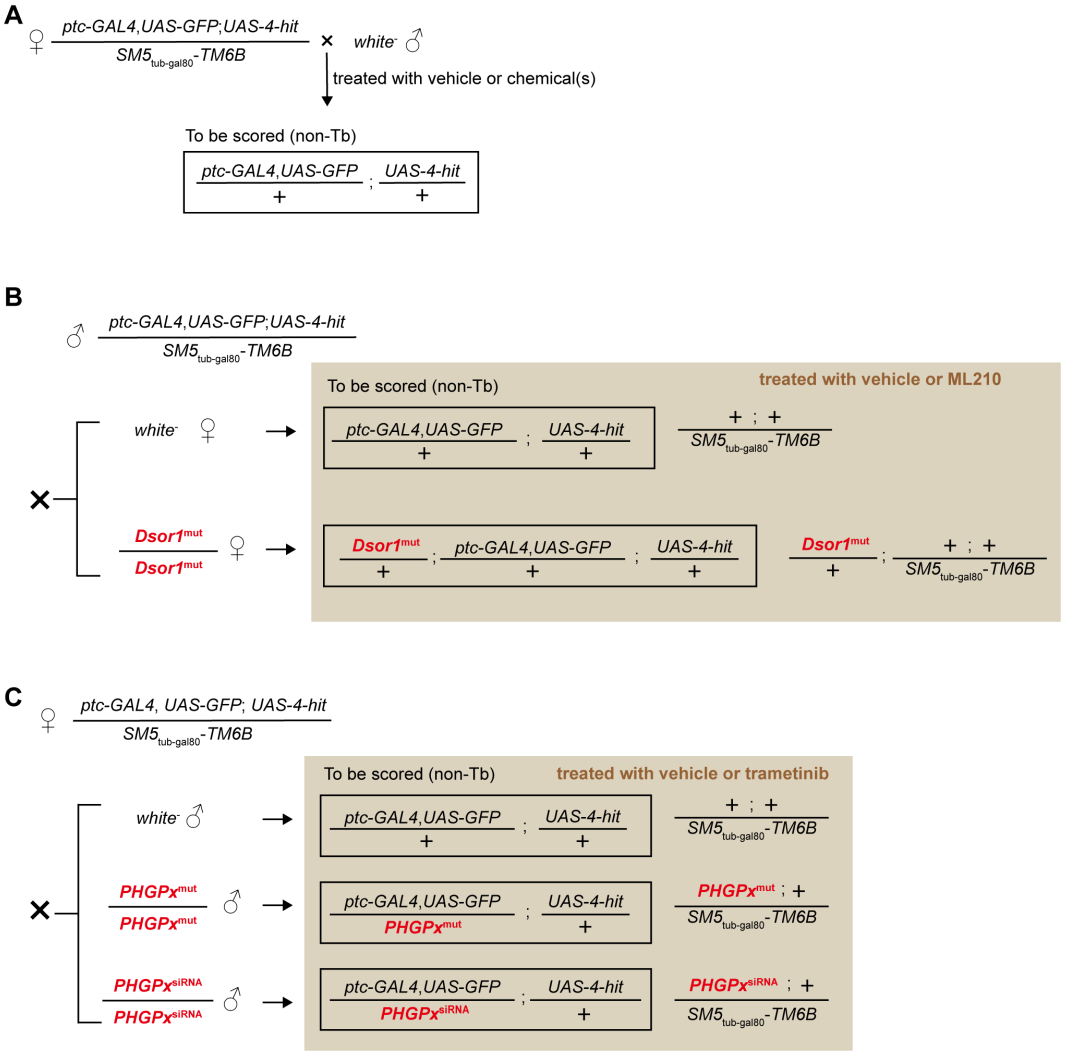

Figure 8. Schemes of fly crossing for wing disc analysis. (A) Wing disc analysis of *ptc>4-hit* under chemical treatment. The progeny of *ptc>4-hit* flies and *white*$^{-}$ were raised on fly food with vehicle or chemical(s) at 27°C. **(B)** Wing disc analysis of *ptc>4-hit* flies with *Dsor1* heterozygous mutation and treated with ML210. The progeny of *ptc>4-hit* flies with either control (*white*$^{-}$) or *Dsor1*-mutant flies were raised on fly food containing vehicle or ML210 at 16°C. **(C)** Wing disc analysis of *ptc>4-hit* flies with functional deficiency of *PHGPx* and treated with trametinib. The progeny of *ptc>4-hit* flies crossed with either control (*white*$^{-}$) or *PHGPx*-mutant flies, or flies carrying *PHGPx* siRNA were raised on fly food with vehicle or trametinib at 25°C.

Soft agar colony formation assays

First, 400 μL of RPMI 1640 medium containing 0.5% agar was spread in each well of a 12-well plate as the bottom layer. Subsequently, AsPC-1 cells (2×10^4 cells/well) were suspended in 400 μL of RPMI 1640 medium containing 0.3% agar and layered on top of the solidified bottom layer. The cells were incubated for 72 hours to allow colony formation. Afterward, 200 μL of RPMI 1640 medium containing the specified chemicals dissolved in DMSO (final DMSO concentration 0.2%) was added to the top of each well. Following a 7-day incubation, colonies were imaged using the Olympus CKX53 inverted microscope (Olympus, Tokyo, Japan), and colony size was quantified using ImageJ software.

RNA interference

GPx4 expression was knocked down using target-specific small interfering RNAs (siRNAs). Two *GPx4* siRNAs were purchased: validated siRNA s6111 (si*GPx4* #1) and s6112 (si*GPx4* #2) from Thermo Fisher Scientific, along with a non-silencing control siRNA (Silencer™ Negative Control #2 siRNA, Thermo Fisher Scientific). AsPC-1 cells were transfected with si*GPx4* (5 nM) or control siRNA (5 nM) using Lipofectamine RNAiMAX (Thermo Fisher Scientific). The siRNA and Lipofectamine RNAiMAX mixtures were added to AsPC-1 cells in 6-well plates and incubated for 24 hours, after which the medium was replaced with standard RPMI 1640 medium. RNA interference efficiency was assessed 48 hours post-transfection by RT-qPCR and western blotting. Follow-up experiments were conducted 48 hours after transfection.

Western blot

Cells were washed with PBS and lysed in Cell Lysis Buffer (Cell Signaling Technology, Danvers, MA) containing phenylmethylsulfonyl fluoride (Fujifilm Wako, Tokyo, Japan). Proteins were then separated on a 10-12% SDS-PAGE gel and transferred onto polyvinylidene difluoride (PVDF) membranes (Millipore, Billerica, MA). After a 20-minute block with Blocking One (Nacalai Tesque), membranes were incubated overnight at 4°C with primary antibody (Table 3). The following day, membranes were incubated with the secondary antibody (Table 3). Immunoreactivity was analyzed with ChemiDoc XRS+ and Image Lab software (Bio-Rad Laboratories, Hercules, CA). Relative signal intensity was determined using the α-tubulin signal as control.

Table 3. Antibody list for Western blot

Antibody	Source	Identifier	Applications
Anti-Glutathione Peroxidase 4 antibody [EPNCIR144]	Abcam	Cat# ab125066 RRID: AB_10973901	Primary antibody 1:1000
α-Tubulin (11H10) Rabbit mAb	Cell signaling Technology	Cat# 2125 RRID: AB_2619646	Primary antibody 1:1000
Goat Anti-rabbit IgG, HRP-linked Antibody	Cell signaling Technology	Cat# 7074 RRID: AB_2099233	Secondary antibody 1:2000

RT-qPCR

Isogen II (Nippon Gene, Tokyo, Japan) was added to cells, and the cell lysate was collected. RNA was then extracted using a spin column method, and 1 μg of this was reverse transcribed to create cDNA using ReverTra Ace® qPCR RT Master Mix (Toyobo, Oosaka, Japan). The reverse transcription reaction was carried out by continuous incubation at 37°C for 15 minutes, 50°C for 5 minutes, and 98°C for 5 minutes. Reverse Transcription-quantitative Polymerase Chain Reaction (RT-qPCR) was carried out using THUNDERBIRD SYBR qPCR Mix (Toyobo, Oosaka, Japan) and the StepOnePlus real-time PCR system (Thermo Fisher Scientific), and after

incubation at 95°C for 1 minute, the cycle was repeated 40 times at 95°C for 15 seconds and 60°C for 45 seconds. Comparative quantification was performed using the ΔΔCt method with GAPDH as the endogenous control (Table 4).

Table 4. Primer list for RT-qPCR

Gene	Forward	Reverse
GPx4	CTGGACAAGTACCGGGGC	TTCCCGAACTGGTTACACGG
GAPDH	GAAGGTGAAGGTCGGAGTC	GAAGATGGTGATGGGATTTC

Hematoxylin-eosin (HE) staining

To prepare formalin-fixed paraffin-embedded (FFPE) blocks, xenografts were collected post-sacrifice and fixed in 4% PFA (Fujifilm Wako) for 24 hours. Following fixation, the samples were embedded in paraffin using HistoCore PEARL (Leica Biosystems, Nussloch, Germany). The FFPE blocks were then sectioned into 5 μm thick slices. Prior to staining, the sections were deparaffinized in xylene and rehydrated through a graded ethanol series. Subsequently, the sections were stained with Mayer's Hematoxylin Solution (Fujifilm Wako) and 0.5% EosinY, Ethanol Solution (Fujifilm Wako) to visualize tissue architecture. Finally, the stained sections were imaged using Keyence BZ-X800 Analyzer (Keyence, Osaka, Japan).

Immunohistochemistry staining

Antigen retrieval was performed by heating the sections to 98°C for 20 minutes in Target Retrieval Solution (Agilent, Santa Clara, CA). Endogenous peroxidase activity was then quenched by treating the sections with 3% hydrogen peroxide (Fujifilm Wako) for 5 minutes. To prevent nonspecific binding, the sections were blocked with SuperBlocking Blocking Buffer (Thermo Fisher Scientific) for 30 minutes at room temperature. Afterward, the sections were incubated overnight at 4°C with primary antibodies against cleaved Caspase 3 (#9661, 1:200, Cell signaling Technology,). The

following day, the sections were treated with the EnVision+ System-HRP labeled polymer (Agilent) for 30 minutes at room temperature. Immune complexes were visualized using ImmPACT DAB peroxidase substrate (Vector Biolabs, Malvern, PA). Finally, the sections were counterstained with hematoxylin, dehydrated in ethanol, and cleared in xylene. The immunohistochemical images were then observed and captured using BZ-X800. The percentage of area containing CC3-positive cells was quantified using ImageJ software (Varghese et al., 2014).

Immunofluorescence staining

After antigen retrieval by heating the sections at 98°C for 20 minutes in Target Retrieval Solution (Agilent), the sections were permeabilized with 0.4% Triton X-100 (Fujifilm Wako) in PBS. They were then blocked with SuperBlocking Blocking Buffer (Thermo Fisher Scientific) for 30 minutes at room temperature. Subsequently, the sections were incubated overnight at 4°C with primary antibodies against 4-HNE (ab48506, 1:25, Abcam, Cambridge, UK). The following day, the sections were incubated with Alexa 488-conjugated anti-mouse IgG secondary antibodies (1:200, Invitrogen, Carlsbad, CA) for 1 hour at room temperature, followed by staining with DAPI (Dojindo Lab) for 5 minutes. Finally, the sections were mounted using Aqua-Poly/Mount (Polysciences, Warrington, PA), and fluorescent images were captured using Keyence BZ-X800 Analyzer.

The scRNAseq data processing

The scRNA-seq gene-barcode matrices were obtained from Gene Expression Omnibus (GEO) database under accession number GSE205013. For this study, I included fourteen sequenced tumor tissue samples from the pancreas of PDAC patients. FASTQ data were aligned to the hg38/GRCh38 reference genome using 10x Genomics Cell Ranger software (version 7.0.1). Batch effects were corrected using the Harmony package (version 0.1.1) in R with default parameters. Cells were filtered according to

established criteria (Werba G, 2023), including those with > 500 detectable genes, > 1500 unique molecular identifiers, > 1% of transcripts corresponding to erythroid genes, < 15% of transcripts derived from mitochondrial genes, and the exclusion of doublets/multiplets identified by scDblFinder (version 1.6.0). Subsequent analyses were conducted using the Seurat package (version 4.3.0.1). Data processing steps included normalization using the NormalizeData function (log-transformed with a scaling factor of 10,000), feature selection with FindVariableFeatures (method: "vst", nfeatures: 2000), and scaling using ScaleData for all detected genes. Dimensionality reduction was conducted through principal component analysis (PCA) using RunPCA (dims: 20), with the top 20 principal components employed for further data reduction using RunUMAP. Nearest neighbors were identified using FindNeighbors, and cell clusters were identified using FindClusters with a resolution range of 0.1 to 2. Data visualization was carried out using Plot1cell (Wu et al., 2022).

Cell identification and clustering

Single-cell clusters were identified based on canonical marker genes, including T/NK cells (*CD3E, NKG7*), epithelial cells (*KRT19*), endothelial cells (*VWF*, *PECAM1*), myeloid cells (*CD68*), mast cells (*KIT*), mesenchymal cells (*DCN*), and B/Plasma cells (*CD79A*).

GSH/ferroptosis module scores

A total of 18 genes associated with GSH metabolism were selected (Yang, F et al., 2023). Additionally, 46 key genes related to ferroptosis were identified from the following sources: KEGG (https://www.genome.jp/kegg/pathway.html) (map04216), AmiGo2 (http://amigo.geneontology.org/amigo) (GO:0006879), and Reactome (https://reactome.org/) (R-HSA-917937) (Table 5). The AddModuleScore function in Seurat was employed to evaluate the relative expression of ferroptosis-related genes across the epithelial cell population (Xu et al., 2023).

Table 5. Gene list for GSH module score and ferroptosis module score

GSH
GCLC
GCLM
GPX4
GPX7
GPX3
GPX8
GSTM3
GSTM4
GSTM5
GSTO1
GSTO2
GSTP1
GSTZ1
HAGH
HAGHL
MGST1
MGST2
MGST3

Ferroptosis	
GPX2	*TFRC*
GPX4	*HMOX1*
FGSTP1	*CP*
MGST1	*SLC11A2*
GSR	*HMOX2*
TMEM199	*SLC40A1*
NUBP1	*STEAP3*
NDFIP1	*ATG5*
TTC7A	*VDAC2*
BOLA2	*ATP6V0B*
SOD1	*ATP6V0C*
SLC11A1	*ATP6V0E1*
HAMP	*STEAP2*
CCDC115	*TF*
HIF1A	*NEDD8*
SRI	*FLVCR1*
ATP13A2	*SKP1*
ABCB6	*GLRX3*
PELO	*LCN2*
CSDE1	*NCOA4*
CNOT6	*FTH1*
SLC7A11	*FTL*
GSS	*LPCAT3*

Statistical analyses

Statistical analyses and graphing were performed using GraphPad Prism (version 9.4.1) (GraphPad Software, Inc., San Diego, CA) and R (version 4.2.2). All statistical tests were two-tailed, with significance defined as a *P*-value of < 0.05.

Result

1. Targeting NAD synthesis pathway alleviates lethality of *4-hit Drosophila* modeling PDAC genotype

In genetic screening, I employed the *Drosophila* model *Ser>4-hit* mimicking the *4-hit* signature in PDAC patients (Sekiya et al., 2023; Fukuda et al., 2024). *Ser* induces transgenes in fly wing discs, reducing the survival rate of fly adult at 27°C to approximately 20%. In previous studies, this survival rate was found to be a practical criterion for identifying both "suppressor genes" that suppress the transforming phenotype by introducing heterozygous mutations and "enhancer genes" that promote it, and this criterion was also applied to the screening in this study (Sonoshita et al., 2018). Hence, I conducted dominant modifier screening utilizing this model to investigate the roles of VM pathways; namely, I introduced either a heterozygous mutation or siRNA of each VM-related gene into *Ser>4-hit* flies to evaluate the impact of reduced gene function in a whole-body context (Figure 9A and Figure 10A). In this screening, I tested the functions of 37 VM genes involved in metabolism of these vitamins (Figure 4).

As a result, functional deficiencies of 23 genes significantly ($P < 0.05$) rescued lethality of *Ser>4-hit* flies, suggesting that they are potential therapeutic targets for PDAC (Table 6 and 7).

Table 6. Fly viability of VM-related gene screening evaluating the effects of heterozygous mutation of genes.

Stock	Fly gene	RRID	*4-hit* fly viabilit	Standard error	*P* value (Dunnett's test)
Control	w^-	N/A	18.0%	0.033	N/A
Heterozygous mutant	*Cat*	BDSC_4014	34.6%	0.032	0.142
Heterozygous mutant	*Cat*	BDSC_17939	34.4%	0.044	0.279
Heterozygous mutant	*CG33156*	BDSC_25470	4.8%	0.023	0.550
Heterozygous mutant	*CG3556*	BDSC_19200	48.3%	0.034	0.000

Heterozygous mutant	*CG6145*	BDSC_42409	16.6%	0.081	1.000
Heterozygous mutant	*CG6993*	BDSC_19112	16.2%	0.015	1.000
Heterozygous mutant	*cn*	BDSC_268	48.3%	0.131	< 0.0001
Heterozygous mutant	*Got2*	BDSC_33073	8.5%	0.043	0.712
Heterozygous mutant	*Idh*	BDSC_4019	44.5%	0.128	0.011
Heterozygous mutant	*Men*	BDSC_4025	26.0%	0.064	0.969
Heterozygous mutant	*Nadsyn*	BDSC_43803	51.5%	0.162	0.000
Heterozygous mutant	*Nmnat*	BDSC_53235	17.1%	0.065	1.000
Heterozygous mutant	*Nmnat*	BDSC_50493	42.5%	0.022	0.007
Heterozygous mutant	*PHGPx*	BDSC_28479	42.9%	0.041	0.001
Heterozygous mutant	*Sirt1*	BDSC_8838	37.0%	0.060	0.004
Heterozygous mutant	*Sod1*	BDSC_24490	70.6%	0.021	< 0.0001

N/A: Not applicable.

Table 7. Fly viability of VM-related gene screening evaluating the effects of gene knockdown induced by siRNA.

Stock	Fly gene	RRID	*4-hit* fly viability	Standard error	*P* value (Dunnett's test)
Control	w^-	N/A	27.5%	0.013	N/A
siRNA	*Cat*	VDRC_103591	60.2%	0.031	0.000
siRNA	*Cat*	BDSC_31894	97.4%	0.013	< 0.0001
siRNA	*CG14882*	BDSC_56006	15.3%	0.011	0.933
siRNA	*CG15116*	BDSC_56992	34.2%	0.032	0.998
siRNA	*CG15116*	VDRC_106717	89.3%	0.106	< 0.0001
siRNA	*CG33156*	BDSC_62858	22.5%	0.075	0.999
siRNA	*CG33156*	NIG_6152R-4	86.5%	0.054	< 0.0001
siRNA	*CG33156*	VDRC_103902	67.4%	0.138	< 0.0001
siRNA	*CG3556*	BDSC_65899	26.8%	0.101	> 0.9999
siRNA	*CG3556*	NIG_3556R-1	72.6%	0.055	< 0.0001
siRNA	*CG5946*	BDSC_65007	29.4%	0.116	1.000
siRNA	*CG5946*	BDSC_35801	43.7%	0.055	0.255
siRNA	*CG5946*	VDRC_110688	34.0%	N/A	0.999
siRNA	*CG6145*	NIG_6145R-1	87.9%	0.047	< 0.0001

siRNA	*CG6145*	VDRC_104271	76.5%	0.097	< 0.0001
siRNA	*CG6739*	NIG_6739R-2	92.1%	0.007	< 0.0001
siRNA	*CG6739*	VDRC_108197	79.0%	0.108	< 0.0001
siRNA	*CG6993*	VDRC_108732	76.5%	0.097	< 0.0001
siRNA	*CG7560*	BDSC_64993	28.3%	0.054	1.000
siRNA	*CG7560*	BDSC_57161	16.9%	0.080	0.860
siRNA	*CG7560*	NIG_7560R-3	67.1%	N/A	0.001
siRNA	*cnc*	BDSC_40854	11.3%	0.031	0.260
siRNA	*cnc*	BDSC_25984	43.4%	0.120	0.285
siRNA	*CPT2*	BDSC_51900	31.7%	0.043	0.575
siRNA	*Doux1*	BDSC_38916	31.1%	0.089	0.999
siRNA	*Gdh*	BDSC_51473	14.7%	0.059	0.891
siRNA	*Got2*	BDSC_78778	10.9%	0.021	0.123
siRNA	*Got2*	VDRC_106120	61.2%	0.089	< 0.0001
siRNA	*Idh*	BDSC_41708	4.2%	0.010	0.042
siRNA	*Keap1*	BDSC_40932	9.7%	0.046	0.140
siRNA	*Keap1*	BDSC_57801	15.0%	0.057	0.737
siRNA	*Kfase*	NIG_9542R-2	70.4%	0.016	< 0.0001
siRNA	*Kfase*	VDRC_109675	64.1%	0.081	< 0.0001
siRNA	*MED4*	BDSC_34697	51.4%	0.071	0.000
siRNA	*Nadsyn*	BDSC_62265	29.9%	0.024	1.000
siRNA	*Nadsyn*	NIG_9940R-1	92.7%	0.037	< 0.0001
siRNA	*Naprt*	BDSC_61875	22.7%	0.033	0.999
siRNA	*Naprt*	BDSC_62264	28.7%	0.044	1.000
siRNA	*Naprt*	NIG_3714R-3	64.9%	0.032	< 0.0001
siRNA	*Nmnat*	BDSC_29402	80.3%	0.084	< 0.0001
siRNA	*Nox*	BDSC_32433	17.6%	0.083	0.977
siRNA	*Parp*	BDSC_57265	12.7%	0.066	0.420
siRNA	*Parp*	NIG_GL00229	12.9%	N/A	0.979
siRNA	*Parp*	BDSC_34888	55.1%	0.131	0.001
siRNA	*PHGPx*	BDSC_33939	16.9%	0.065	0.942
siRNA	*PHGPx*	VDRC_100790	59.7%	0.175	< 0.0001
siRNA	*PHGPx*	BDSC_41879	36.3%	N/A	0.999

siRNA	*PHGPx*	BDSC_25968	71.9%	0.038	< 0.0001
siRNA	*polo*	NIG_12306R-3	80.1%	0.033	< 0.0001
siRNA	*polo*	NIG_GL00014	19.2%	N/A	0.999
siRNA	*polo*	VDRC_330025	6.3%	0.022	0.027
siRNA	*sgll*	BDSC_65207	34.9%	0.065	0.998
siRNA	*sgll*	NIG_31472R-4	33.2%	0.106	0.999
siRNA	*sgll*	VDRC_105941	79.4%	0.045	<0.0001
siRNA	*Sirt1*	BDSC_31636	42.5%	0.135	0.240
siRNA	*Sirt1*	NIG_5216R-1	21.5%	0.051	0.999
siRNA	*Sirt1*	NIG_HMS00484	15.6%	0.048	0.819
siRNA	*Sod1*	BDSC_29389	92.8%	0.065	< 0.0001
siRNA	*SoxN*	NIG_18024R-1	88.7%	0.088	< 0.0001
siRNA	*SoxN*	BDSC_25996	82.9%	0.087	< 0.0001
siRNA	*Trxr-1*	BDSC_53883	22.3%	0.125	0.999
siRNA	*Trxr-1*	BDSC_36805	29.8%	0.074	1.000
siRNA	*Trxr-1*	VDRC_110648	57.5%	0.134	0.001
siRNA	*Tsf1*	BDSC_62968	11.2%	0.042	0.246
siRNA	*Tsf2*	BDSC_65903	16.9%	0.048	0.938
siRNA	*Tsf3*	BDSC_56015	41.1%	0.055	0.575
siRNA	*v*	NIG_2155R-1	85.8%	0.019	< 0.0001
siRNA	*v*	NIG_2155R-2	90.3%	N/A	< 0.0001
siRNA	*v*	NIG_HMC03041	69.1%	0.084	< 0.0001
siRNA	*v*	VDRC_107798	90.8%	0.035	< 0.0001
siRNA	*Zw*	BDSC_50667	44.0%	0.226	0.228

N/A: Not applicable.

Notably, twelve of the 23 genes are part of NAD synthesis pathway, including *cinnabar* [*cn*; a fly ortholog of human *Kynurenine 3-monooxygenase* (*KMO*)], *Kynurenine formamidase* [*Kfase*; *Arylformamidase* (*AFMID*)], *NAD kinase 1a* [*CG6145*, *NAD Kinase* (*NADK*)], *NAD kinase 1b* [*CG3315*, *NAD Kinase* (*NADK*)], *NAD synthetase* [*Nadsyn*; *NAD synthetase 1* (*NADSYN1*)], *Nicotinamide mononucleotide adenylyltransferase* (*Nmnat*; *NAMPT*), *Nicotinate phosphoribosyltransferase* (*Naprt*; *NAMPT*), *Poly-(ADP-ribose) polymerase* [*Parp*; *Poly(ADP-Ribose) Polymerase 1* (*PARP1*)], *Sirtuin 1* [*Sirt1*; *Sirtuin 1* (*SIRT1*)], *SoxNeuro* (*SoxN*; *SRY-Box Transcription Factor 2* (*SOX2*)], *CG6993* [(*spineless*; *Aryl Hydrocarbon Receptor* (*AHR*)], and *vermilion* [*v*; *Tryptophan 2,3-dioxygenase* (TDO)] (Figure 9B and Figure 10B). This finding highlights the critical role of the VB3 metabolism pathway in regulating the viability of *Ser>4-hit* flies.

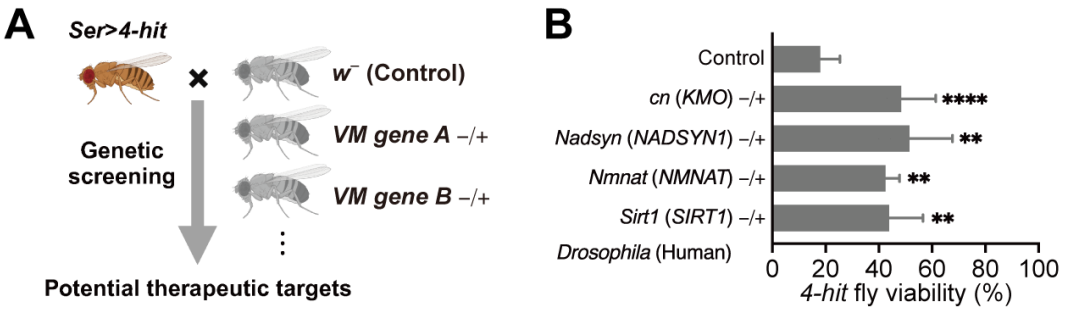

Figure 9. Genetic screening in *Ser>4-hit* flies to evaluate the effects of heterozygous mutations in vitamin metabolism (VM) genes. (A) Heterozygous mutations in individual VM genes were introduced to *Ser>4-hit* flies by crossing. **(B)** Heterozygous mutation of four genes, including *cn*, *Nadsyn*, *Nmnat* and *Sirt1*, all related to VB3 pathway, rescued the lethality of *Ser>4-hit* flies. The viability of the offspring was compared to progeny from a cross between *4-hit* flies and w^- control flies. Statistical significance was determined using one-way ANOVA with post-hoc Dunnett's multiple comparisons test. $^{**}P < 0.01$, $^{****}P < 0.0001$.

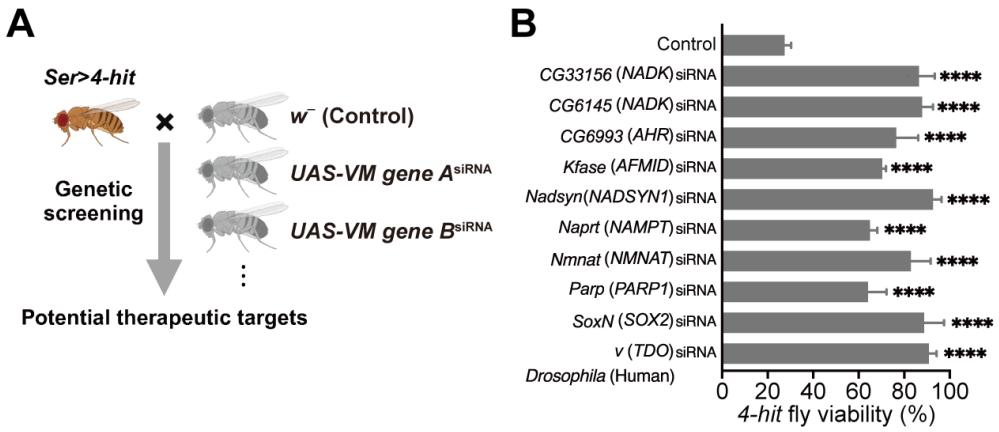

Figure 10. Genetic screening in *Ser>4-hit* flies to evaluate the effects of VM gene knockdown by siRNA. (A) VM genes were knocked down by crossing *Ser>4-hit* flies with flies expressing siRNA targeting specific genes under the control of the *Ser* enhancer. **(B)** Knockdown of ten genes, including *CG33156*, *CG6145*, *CG6993*, *Kfase*, *Nadsyn*, *Naprt*, *Nmnat*, *Parp*, *SoxN* and *v* in the VB3-related pathway rescued the lethality of *Ser>4-hit* flies. The viability of the offspring was compared to progeny from a cross between *4-hit* flies and w^- control flies. Statistical significance was determined using one-way ANOVA with post-hoc Dunnett's multiple comparisons test. ****$P < 0.0001$.

Furthermore, human PDAC tissues exhibit elevated expression levels of *NAPRT*, *NAMPT*, and *TDO* compared to normal pancreatic tissue (Figure 11), collectively suggesting that the activation of NAD synthesis could present a therapeutic vulnerability in PDAC.

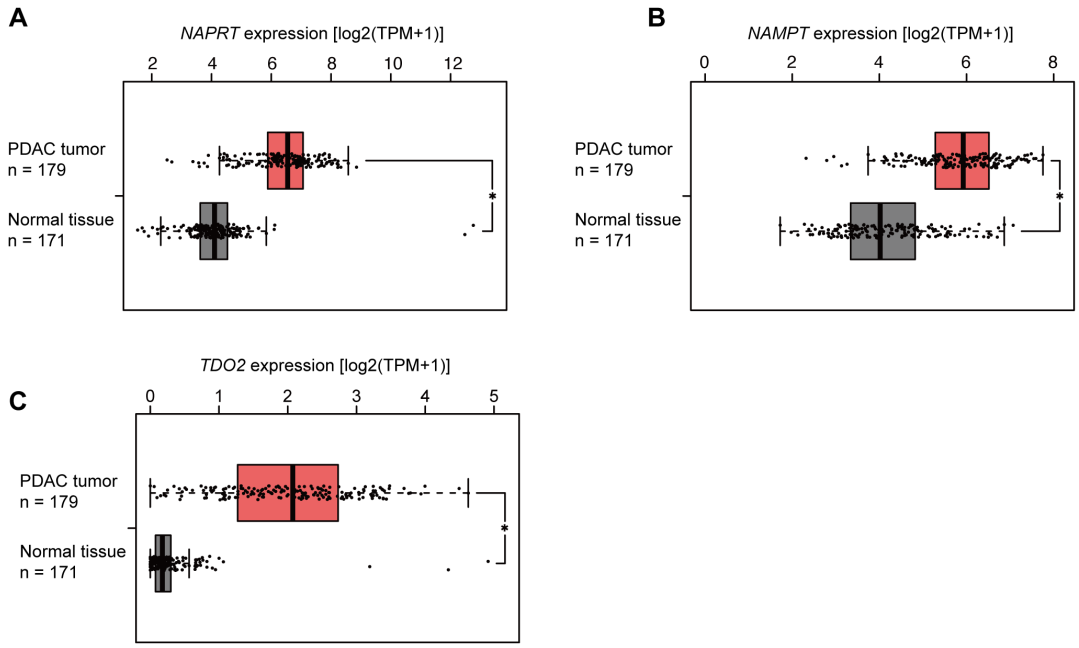

Figure 11. Increased mRNA expression of *NAPRT*, *NAMPT* and *TDO2* in pancreatic cancer tissue compared to normal pancreatic tissue. mRNA expression levels of *NAPRT* **(A)**, *NAMPT* **(B)** and *TDO2* **(C)** were significantly elevated in pancreatic cancer tissue relative to normal pancreatic tissue. RNA sequencing data were sourced from The Cancer Genome Atlas (TCGA) and Genotype-Tissue Expression (GTEx) databases, with graphs generated using GEPIA (http://gepia.cancer-pku.cn). Statistical significance was calculated using one-way ANOVA. *$P < 0.001$.

It has been well established that cells synthesize NAD through both exogenous VB3 derived from dietary and endogenous tryptophan (Kincaid and Berger, 2020) (Figure 12). Using nicotinic acid as a starting material, the Preiss-Handler pathway converts NA into NAD through reactions involving NAPRT, NMNAT, and NADSYN1. Additionally, the salvage pathway converts NM into NAD, facilitated by enzymes including NAMPT and NMNAT. In contrast to these pathways that utilize dietary VB3, the de novo pathway begins with endogenous tryptophan, which is converted into NAD through enzymatic reactions involving TDO, AFMID, and KMO (Yaku et al., 2018). Each of these pathways is crucial for maintaining adequate NAD levels necessary for cellular metabolism and energy production.

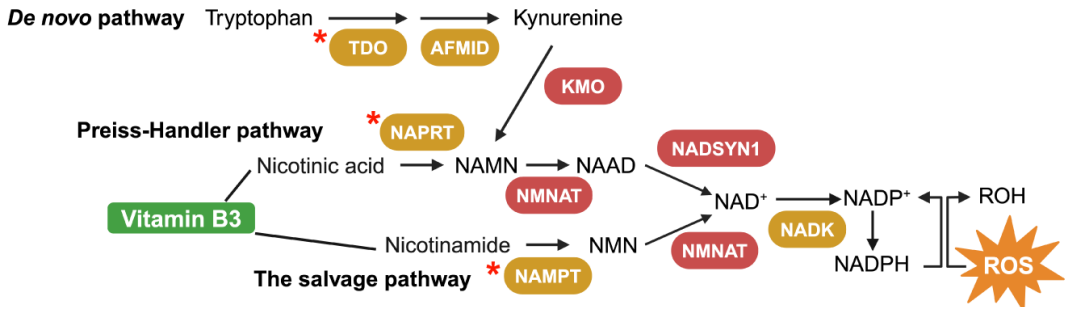

Figure 12. Schematic diagram of NAD synthesis pathway in VB3 metabolism. Yellow highlights proteins whose knockdown rescued lethality of *Ser>4-hit* flies. Red indicates proteins where both heterozygous mutation and knockdown rescued the lethality of *Ser>4-hit* flies. Red asterisks mark genes that exhibit mRNA overexpression in human PDAC tissue compared to normal tissue.

Hence, it is hypothesized that elevated intracellular NAD levels could promote the progression of transformed cells, leading to a further decrease in the survival rate of Ser>4-hit flies. To test this, I supplemented the fly food with VB3, including NM and NA, as well as the active form of VB3, β-nicotinamide adenine dinucleotide phosphate (β-NADP), and the antioxidant N-acetylcysteine (NAC). First, I determined maximum tolerated dose (MTD) for each compound employing w− flies to ensure safe administration (Figure 13A). Subsequently, I administered varying concentrations of NM, NA, β-NADP, and NAC to Ser>4-hit flies, anticipating a notable reduction in their survival rate following VB3 supplementation. However, I did not observe the survival of the flies after chemical treatment (Figure 13B). A potential explanation is that VB3, due to its water-soluble nature, is readily excreted through bodily fluids such as urine (Fukuwatari and Shibata, 2007), thereby constraining its impact on fly viability.

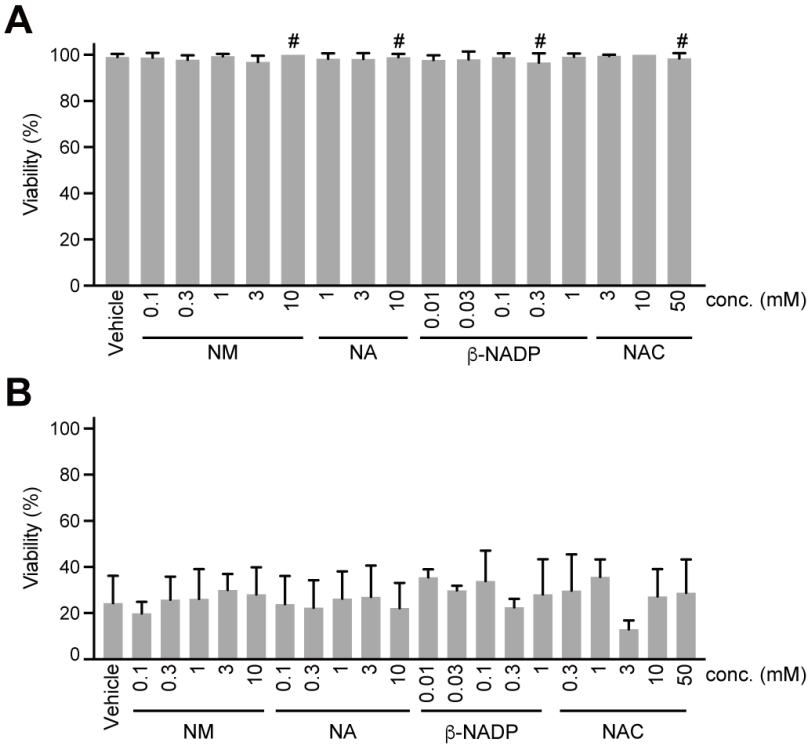

Figure 13. Supplementation of vitamin B3 in fly food does not affect the survival rate of *4-hit* flies. (A) MTD determination for NM, NA, β-NADP, and NAC. The concentration of each compound was determined based on its solubility, and the viability of *w*− flies orally administered the vitamin-supplemented food was

measured. The highest concentration (#) that did not affect fly survival was defined as the MTD and used as the maximum concentration for further testing. **(B)** The survival rate of *Ser>4-hit* flies with the indicated concentrations of NM, NA, β-NADP, and NAC. Statistical significance was calculated using one-way ANOVA with post-hoc Dunnett's multiple comparisons test. No significant difference was observed.

To further investigate the role of VB3, I cultured a human PDAC cell line AsPC-1 harboring the *4-hit* signature (Sekiya et al., 2023) in the presence or absence of NM. As a result, I observed significantly decreased spheroid volume (Figure 14A and 14B), underscoring the essential role of VB3 in maintaining viability of PDAC cells. It is intriguing that the depletion of VB3, and consequently NAD, appears to disrupt crucial metabolic processes, suggesting that NAD synthesis could be a promising therapeutic target in PDAC treatment strategies.

As the active form of VB3, NAD and its derivatives, namely NADH and NADPH, are crucial for maintaining the redox balance within cells. NADPH plays a crucial antioxidant role in glutathione redox cycle, which involves the reduction of glutathione disulfide (GSSG) to glutathione by Glutathione reductase, a process dependent on NADPH. GSH is a major antioxidant that neutralizes reactive oxygen species (ROS), thereby protecting cells against oxidative damage (Yang and Sauve, 2016). Hence, it is hypothesized that oxidative stress might inhibit the proliferation of PDAC cells observed under VB3 deficiency. To test this hypothesis, I used a DCFH-DA probe, which detects intracellular ROS, and revealed a significant increase in intracellular ROS levels in VB3-deficient AsPC-1 cells by flow cytometry (Figure 14C), suggesting that VB3 deficiency led to the accumulation of ROS. This increase in ROS levels under VB3 deficiency implies that reducing oxidative stress is crucial in PDAC tumorigenesis. Therefore, decreasing antioxidant capacity may enhance the accumulation of intracellular ROS, thereby inhibiting PDAC cell proliferation, which highlights a promising therapeutic avenue.

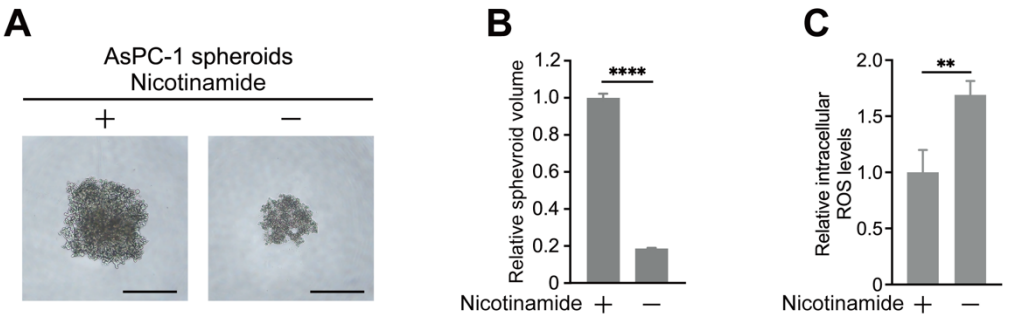

Figure 14. Nicotinamide depletion suppresses spheroid growth in human PDAC cells. (A) Morphology and **(B)** relative volume of AsPC-1 spheroids in the presence (+) or absence (-) of nicotinamide. AsPC-1 cells were cultured for five days before observation. Scale bars, 500 μm. **(C)** Nicotinamide depletion led to an increased relative level of intracellular ROS in AsPC-1 cells, detected using DCFH-DA fluorescence. Statistical analysis was performed using Student's *t*-test for (B) and (C). $^{**}P < 0.01$, $^{****}P < 0.0001$.

2. Genetic screening and chemical testing in *Ser>4-hit* flies identify GPx4 as a therapeutic target of PDAC

NAD and its phosphorylated form, NADP, play essential role in glutathione redox cycle, which helps maintain cellular redox balance and protects cells from oxidative stress (Yang and Sauve, 2016). Key enzymes in this cycle include NADK and Malic enzyme 1 (ME1) which convert NAD to NADP, Glutathione reductase (GR), which regenerates GSH from GSSG. Other important proteins, such as GPx4, and Superoxide dismutase 1 (SOD1) and catalase (CAT), contribute to reducing ROS levels (Figure 15).

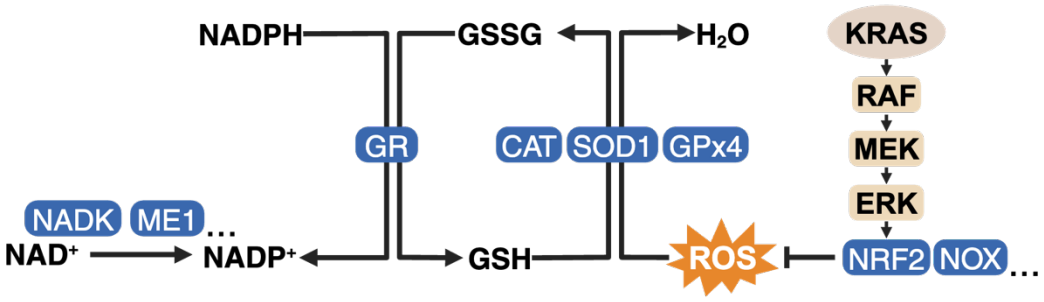

Figure 15. Schematic diagram showing glutathione redox pathway downstream of NAD synthesis pathway, including genes regulating ROS.

In my genetic screening of ROS-related genes, I observed a significant improvement in the viability of *Ser>4-hit* flies when *Sod1* or *PHGPx* were made heterozygous (Figure 16A). Additionally, knockdowns of *Trxr-1* (a fly ortholog of human *GR*), *PHGPx* (*GPx4*), *CG15116* (*GPx4*), *Sod1* (*SOD1*), and *Cat* (*CAT*) also improved survival (Figure 16B). These results highlight the importance of controlling oxidative stress in mitigating the lethality of *Ser>4-hit* flies, suggesting that these genes are potential therapeutic targets for PDAC.

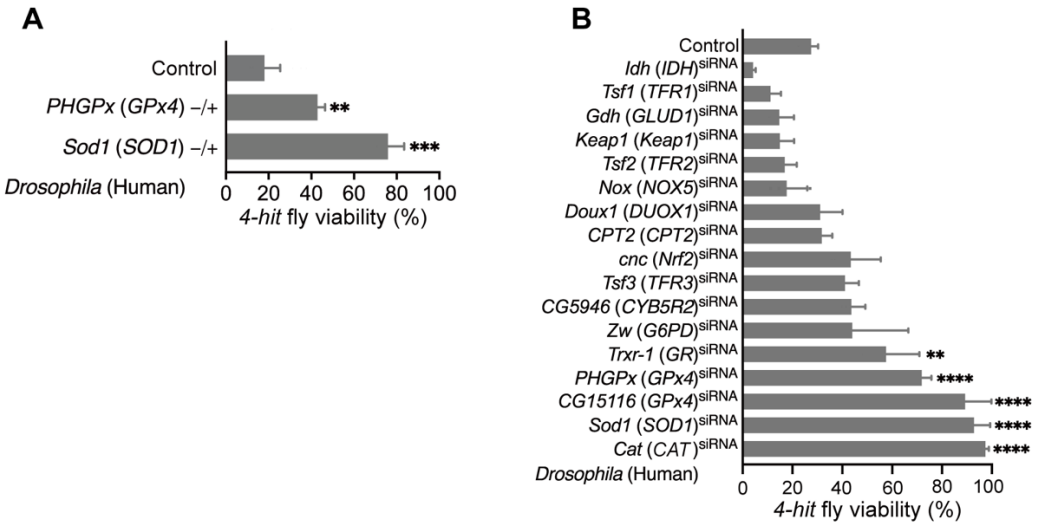

Figure 16. Genetic screening in *Ser>4-hit* flies to assess the impact of heterozygous mutations and gene knockdown in the glutathione redox pathway. **(A)** Heterozygosity of *PHGPx* or *Sod1* rescued the lethality of *Ser>4-hit* flies. **(B)** Knockdown of *Trxr-1*, *PHGPx*, *CG15116*, *Sod1*, or *Cat* in transformed cells rescued the lethality of *Ser>4-hit* flies. The viability of the resulting offspring was compared with that of progeny obtained from a cross between *4-hit* flies and w^- control flies using one-way ANOVA with post-hoc Dunnett's multiple comparisons test. ***P*, < 0.01, ****P* < 0.001, *****P* < 0.0001.

Following these genetic findings, I focused on developing novel therapeutic strategies for PDAC and explored small-molecule inhibitors targeting these genes. Firstly, I determined the MTD for each compound in w^- flies to ensure safe dosing (Figure 17).

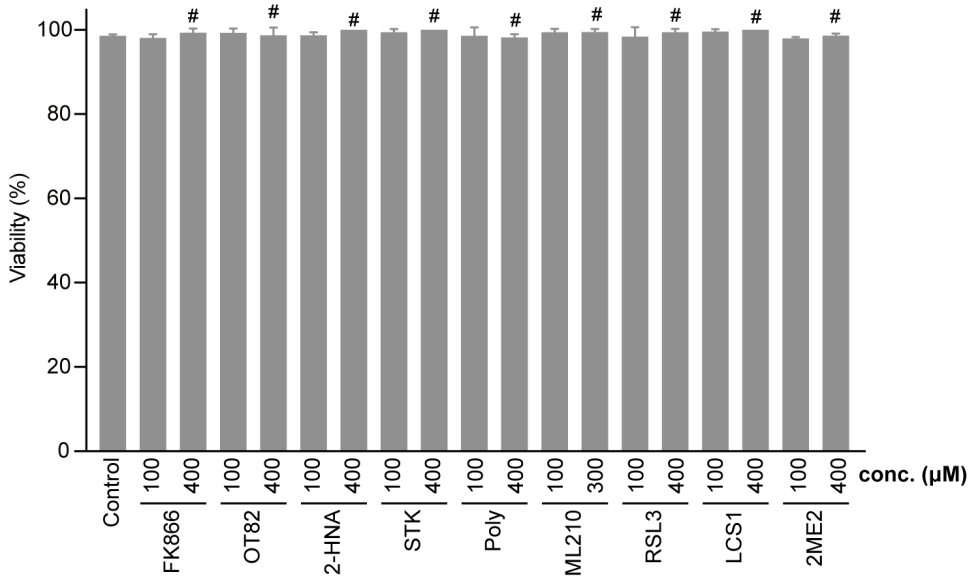

Figure 17. MTD determination for small molecule inhibitors targeting candidate genes. The concentration of each compound was determined based on its solubility, and the viability of w^- flies orally administered the indicated concentration of chemicals was measured. The highest concentration (#) that did not affect fly survival was defined as the MTD and used as the maximum concentration for further testing. Statistical significance was calculated using one-way ANOVA with post-hoc Dunnett's multiple comparisons test. No significant difference was observed.

Based on the MTD of each compound, I then conducted chemical testing using *Ser>4-hit* flies to assess their therapeutic potential. Although most inhibitors showed limited effectiveness as monotherapies, ML210, a covalent GPx4 inhibitor (Eaton et al., 2020), significantly extended the survival of *Ser>4-hit* flies when combined with the MEK inhibitor trametinib (Figure 18). This combination highlights GPx4 as a promising therapeutic target for PDAC. Also, the synergy between ML210 and trametinib underscores the potential of targeting GPx4 in tandem with MEK inhibition to suppress PDAC progression.

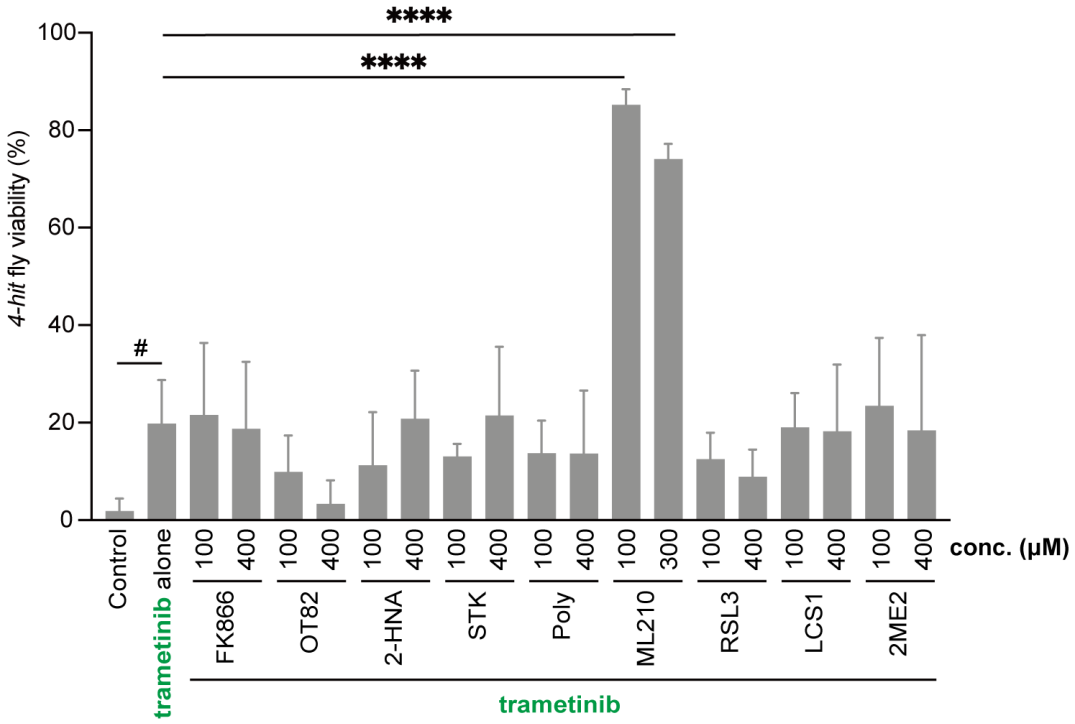

Figure 18. The combination of ML210 and trametinib enhanced viability of *Ser>4-hit* flies, indicating anti-PDAC potential. Small molecule inhibitors targeting candidate genes were tested in *Ser>4-hit* flies to evaluate their potential therapeutic effects on PDAC. *Ser>4-hit* flies were treated with various concentrations of the indicated inhibitors with 0.5 μM trametinib. MicroM, final concentration in fly food. While most inhibitors showed limited efficacy, ML210 significantly improved fly viability when combined with trametinib. This combination demonstrated a synergistic effect, resulting in a significant increase in fly survival compared to other

treatments. Data are presented as mean + SD. ****$P < 0.0001$ in one-way ANOVA with post-hoc Dunnett's tests compared with trametinib alone; $^{\#}P < 0.05$ in Student's *t* test.

GPx4 is known to protect cancer cells against oxidative damage and can have an oncogenic effect in multiple cancers (Zhang et al., 2020). Previous studies have shown that in KRAS-activated cancers, such as PDAC, oncogenic signaling through RAF-MEK-ERK enhances NRF2 activation, leading to increased antioxidant defenses (DeNicola et al., 2011). This suggests that targeting GPx4 alone may not be sufficient in these cancers, as they possess strong antioxidant defenses. However, trametinib has been reported to enhance the therapeutic effect of dabrafenib, the BRAF inhibitor drug, in melanoma and squamous cell carcinoma, primarily by increasing ROS production and inducing caspase-activated apoptosis (Tham et al., 2018). The synergistic effects of trametinib and dabrafenib suggest the possibility of eliminating intracellular antioxidant defenses through the action of MEK inhibitors to exert anti-tumor effects by inducing cytotoxic ROS.

To verify such synergistic anti-tumor effects, I further examined the phenotypic rescue effect rescue following dual inhibition of GPx4 and MEK in *Ser>4-hit* flies. Adult wing malformation, characterized by abnormal wing venation, is a well-established marker of RAS signaling activation (Sekiya et al., 2023; Fukuda et al., 2024; Karim and Rubin, 1998). Confirming our previous results, *Ser>4-hit* adults exhibited irregular structure featuring a sac-like form as reported (Figure 19A) (Sekiya et al., 2023; Fukuda et al., 2024). In comparison to this, both knockdown and heterozygosity of GPx4 significantly suppressed wing abnormalities (Figure 19B).

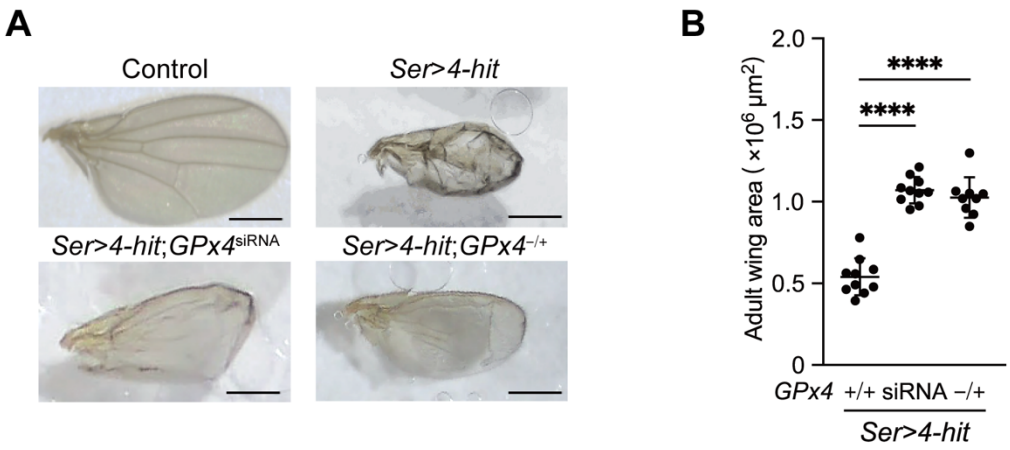

Figure 19. *GPx4* knockdown or heterozygosity suppresses wing malformation in *Ser>4-hit* flies. (A) *GPx4* knockdown or heterozygosity restored the wing morphology of *Ser>4-hit* flies similar to that of wild-type flies. Scale bars, 500 μm. **(B)** Quantification of wing area comparing *Ser>4-hit* flies with wildtype *GPx4* and *Ser>4-hit* flies with *GPx4* knockdown or heterozygosity. Statistical significance was assessed using one-way ANOVA followed by Dunnett's post-hoc test. ****$P <$ 0.0001. Each dot represents one wing.

Similarly, monotherapy with either ML210 or trametinib reduced wing malformation in *Ser>4-hit* flies, while the combination of ML210 and trametinib showed the most pronounced effect (Figure 20). This provides strong evidence that dual inhibition of GPx4 and MEK can counteract RAS-driven phenotypes.

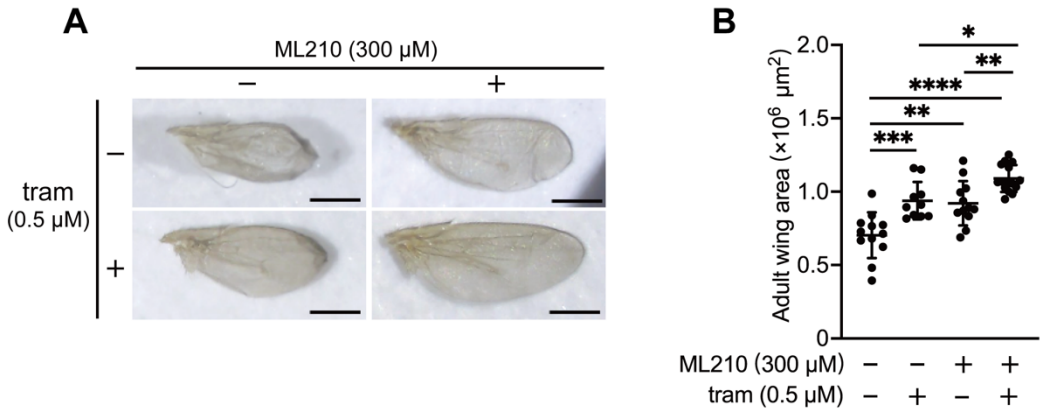

Figure 20. Rescue of wing malformation in *Ser>4-hit* flies by combined administration of ML210 and trametinib. (A) ML210 combined with trametinib effectively suppressed wing defects in *Ser>4-hit* flies. Scale bars, 500 μm. **(B)** Quantification of wing area in *Ser>4-hit* flies treated by chemicals. ML210 alone and trametinib alone suppressed wing malformation; however, their combination demonstrated the most pronounced effect. Statistical significance was calculated by one-way ANOVA followed by post-hoc Tukey HSD test. **P* < 0.05, ***P*, < 0.01, ****P* < 0.001, *****P* < 0.0001. Each dot represents one wing.

To further evaluate the potential of targeting GPx4 and MEK as a novel therapeutic strategy for PDAC, I employed multiple approaches to simultaneously inhibit their activities in flies and monitored the effects on transformed cells. In *Ser>4-hit* flies, I use the *Ser* enhancer to assess fly survival and wing malformation because it induces transgenes in a significant portion of epithelial cells in wing discs. However, this approach limits its utility for observing the proliferation and migration of transformed cells. Therefore, in this study, I employed the *ptc* enhancer, which induces transgenes in a limited number of cells, allowing for the examination of transformed cell phenotypes in wing discs of third-instar larvae (Sonoshita et al., 2018; Ung et al., 2019; Sekiya et al., 2023; Fukuda et al., 2024; Dar et al., 2012).

First, I dosed ML210 and trametinib to *ptc-gal4*,*UAS-GFP*,*UAS-4-hit* flies (hereafter referred to as *ptc>4-hit* flies), and found that their combination decreased the area containing GFP-expressing transformed cells in wing discs (Figure 21), which marks the location of transformed cells displaying aggressive proliferation and migration (Sekiya et al., 2023; Fukuda et al., 2024). ML210 or trametinib alone did not significantly influence the GFP area, although a decreasing trend was observed. However, the combination of trametinib and ML210 significantly reduced the GFP area, consistent with my expectation that this combination would be most effective in inhibiting the progression of transformed cells.

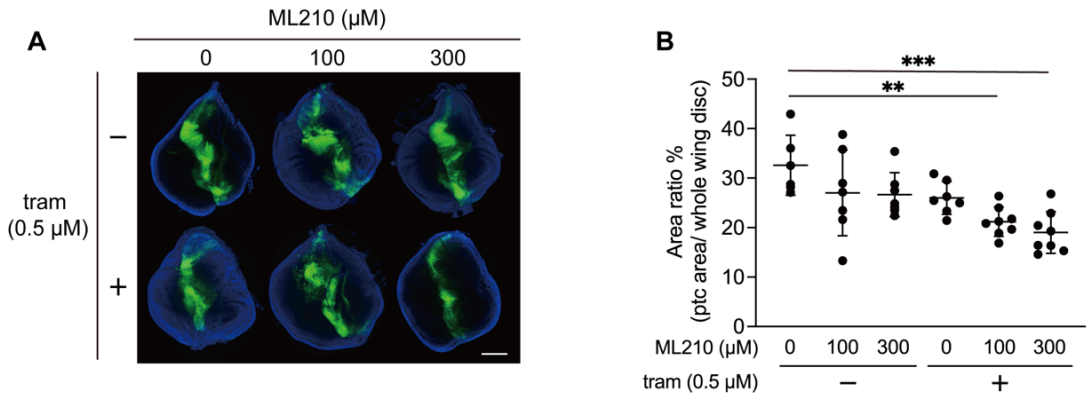

Figure 21. The combination of ML210 and trametinib suppressed transformation in the developing wing disc of *ptc>4-hit* larvae. (A) Wing discs of

ptc>4-hit larvae in treated with both ML210 and trametinib exhibited a smaller GFP-labeled area, indicating reduced transformation. Transformed cells are labeled with GFP. Blue, DAPI outlining the disc margin. Scale bar, 100 μm. **(B)** Quantification of the relative *ptc* area in *4-hit* wing discs treated by chemicals. Statistical significance was calculated by one-way ANOVA with post-hoc Dunnett's multiple comparisons test. ***P*, < 0.01, ****P* < 0.001. Each dot represents one disc.

Additionally, I administered ML210 to *ptc>4-hit* flies introduced with *Dsor1* (*MEK*) heterozygosity and observed GFP-expressing transformed cells in wing discs. ML210 alone significantly decreased the GFP area ratio relative to the entire wing disc, indicating reduced proliferation of transformed cells. In *ptc>4-hit* flies with *MEK* heterozygosity treated with ML210, wing discs almost fully recovered, showing minimal GFP areas (Figure 22). This indicates that Dsor1 inhibition is highly effective in suppressing the proliferation of transformed cells, and ML210 works synergistically with Dsor1 inhibition.

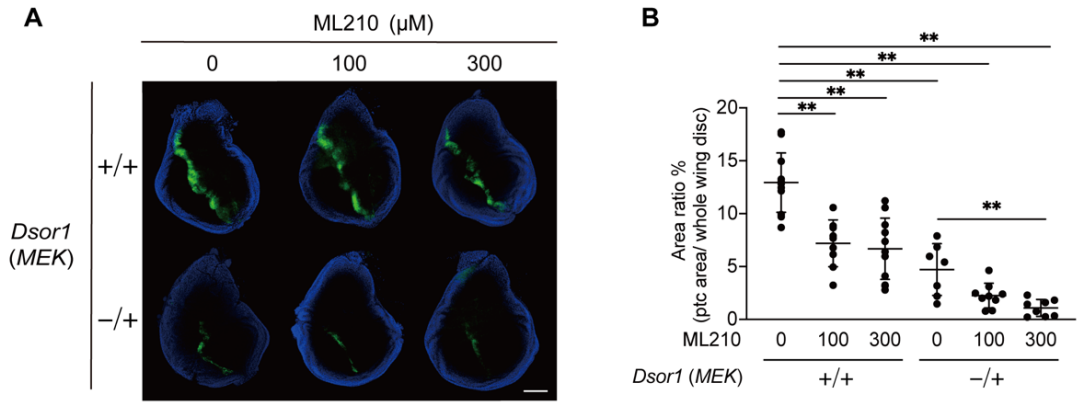

Figure 22. ML210 suppressed transformation in the wing disc of *ptc>4-hit* larvae with or without *Dsor1* (a fly ortholog of human *MEK*) heterozygosity. (A)Wing discs of *ptc>4-hit* larvae with *Dsor1* heterozygosity treated with ML210 exhibited a significantly smaller GFP-labeled area compared to *ptc>4-hit* larvae, both with or without *Dsor1* heterozygosity. **(B)** Relative *ptc* area to the whole wing disc in *ptc>4-hit* larvae treated with trametinib and ML210, with either *PHGPx* (a fly ortholog of human *GPx4*) heterozygosity or *GPx4* knockdown. Statistical significance was calculated by one-way ANOVA with post-hoc Dunnett's multiple comparisons test. ***P*, < 0.01. Each dot represents one disc.

Furthermore, trametinib administration on *ptc>4-hit* flies with *PHGPx* siRNA or heterozygosity also reduced the GFP area and fluorescent intensity in transformed cells throughout wing discs (Figure 23). In *ptc>4-hit* flies with *PHGPx* siRNA, trametinib decreased the GFP area in a dose-dependent manner. These findings indicate that dual inhibition of GPx4 and MEK effectively suppresses viability of transformed cells in *ptc>4-hit* flies.

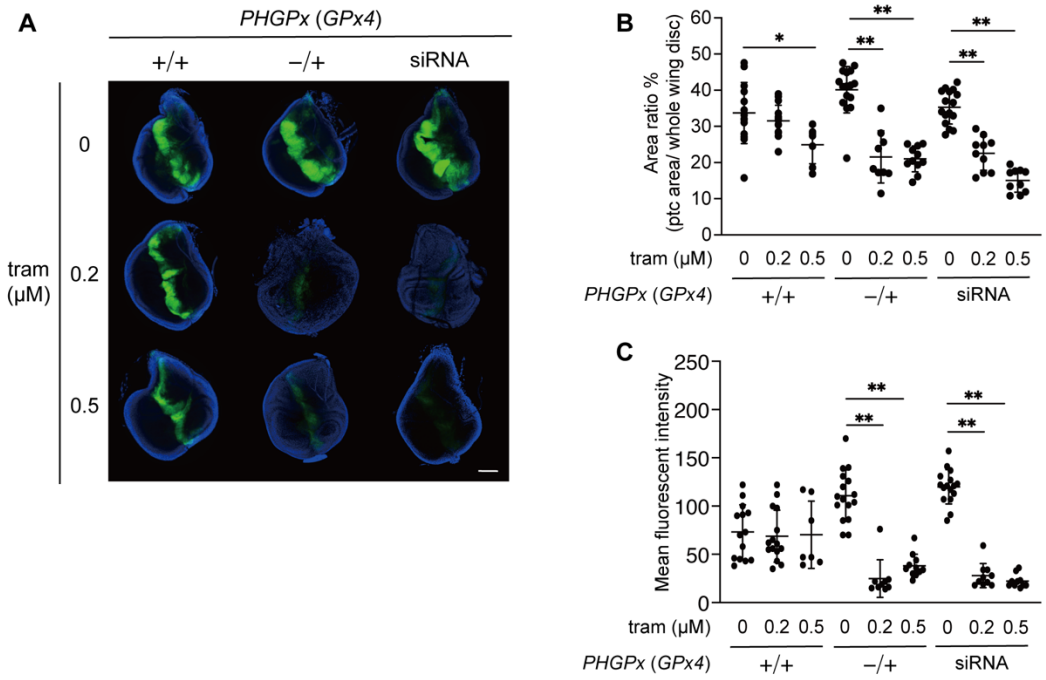

Figure 23. Trametinib suppressed transformation in the wing disc of *ptc>4-hit* larvae or *ptc>4-hit* larvae with *GPx4* heterozygosity or knockdown of *GPx4*. (A) Wing discs of *ptc>4-hit* larvae with *GPx4* heterozygosity or *GPx4* knockdown, treated with trametinib (tram), exhibited a significantly smaller GFP-labeled area compared to *ptc>4-hit* larvae without *GPx4* heterozygosity or *GPx4* knockdown. **(B)** Relative *ptc* area in wing discs of trametinib-treated *ptc>4-hit* flies with additional *GPx4* heterozygosity or *GPx4* knockdown. **(C)** Mean fluorescent intensity (IntDen/Area) of GFP in wing discs, indicated that alteration occurs when blocking GPx4 and MEK simultaneously. Statistical significance was calculated by one-way ANOVA followed by post-hoc Tukey HSD test. **P* < 0.001, ***P* < 0.0001.

Apart from fly platform, to elucidate the role of GPx4 in PDAC cells, I employed RNA interference in human AsPC-1 cells. Knockdown of *GPx4* in AsPC-1 cells significantly reduced their mRNA expression and protein levels (Figure 24A and 24B). When cultured in 3D, *GPx4*-knockdown cells exhibited decreased spheroid volume, and this inhibitory effect was more pronounced in the presence of trametinib (Figure 23C). These results underscore the potential of targeting GPx4 as an effective therapeutic strategy for PDAC. The enhanced inhibitory effect observed with trametinib further indicates a potential synergistic interaction, where the suppression of GPx4 combined with trametinib treatment exacerbates the reduction in spheroid volume.

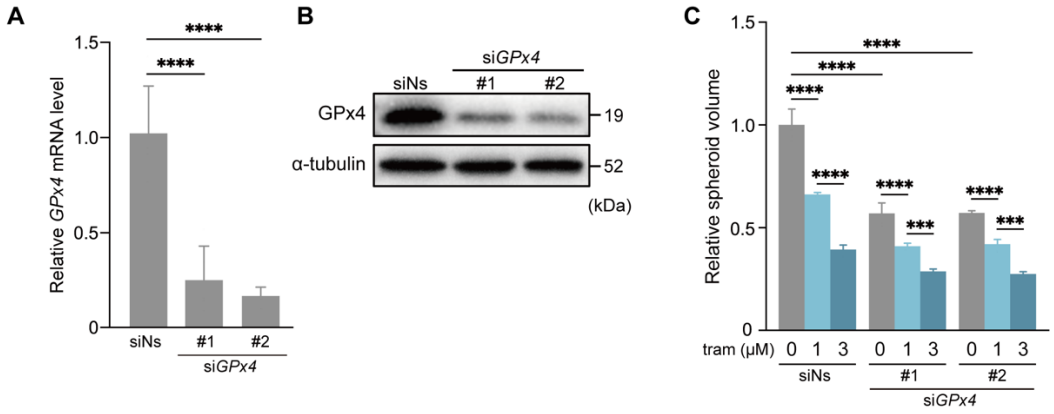

Figure 24. Inhibition of GPx4 and MEK suppresses the proliferation of human PDAC. (A) Quantitative PCR analysis showing relative *GPx4* mRNA levels in AsPC-1 cells 48 hours post-transfection with non-silencing siRNA (siNs) or two different *GPx4*-specific siRNAs (#1 and #2). ****$P < 0.0001$, compared with control in one-way ANOVA with post-hoc Dunnett's multiple comparisons test. **(B)** Western blot analysis showing GPx4 protein levels in AsPC-1 cells 48 hours post-transfection with siNs or *GPx4*-specific siRNAs. Alpha-tubulin was detected as a loading control. **(C)** Spheroid volumes were significantly reduced in the presence of trametinib and si*GPx4*. AsPC-1 cells were first transfected with *GPx4*-specific siRNAs for 48 hours, then seeded at 1,000 cells per well in cell-repellent 96-well plates to establish spheroids over 72 hours. The relative spheroid volumes were subsequently analyzed following treatment. Statistical significance was calculated by one-way ANOVA followed by post-hoc Tukey HSD test. **$P < 0.01$, ***$P < 0.001$, ****$P < 0.0001$.

In summary, I identified GPx4 as a critical therapeutic target in PDAC. The dual inhibition of GPx4 and MEK showed significant promise as a strategy to suppress tumor progression by inducing oxidative stress and reducing cell viability.

3. Human PDAC exhibits a gene expression signature suggesting sensitivity to GPx4 inhibition and ferroptosis induction

Following the identification of GPx4 as a therapeutic target in the *4-hit* fly models and human PDAC cells, I sought to evaluate its clinical relevance in human PDAC. Notably, human PDAC tissues exhibit elevated expression levels of *GPx4* compared to normal pancreatic tissue (Figure 25). This overexpression, combined with its role in our models, collectively suggests that *GPx4* might present a therapeutic vulnerability in PDAC.

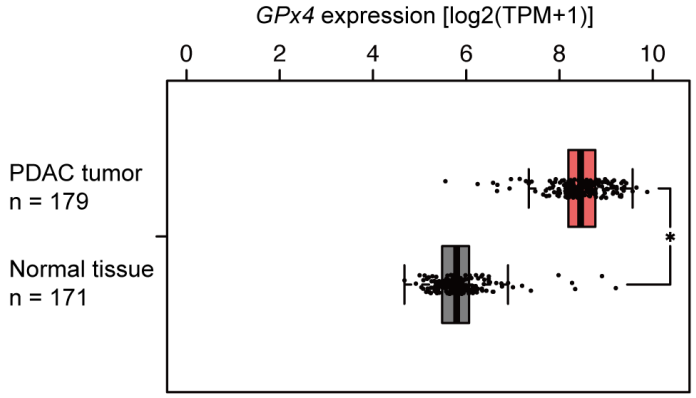

Figure 25. Increased mRNA expression of *GPx4* in pancreatic cancer tissue compared to normal pancreatic tissue. mRNA expression levels of *GPx4* were significantly elevated in pancreatic cancer tissue relative to normal pancreatic tissue. RNA sequencing data were sourced from TCGA and GTEx, with graphs generated using GEPIA (http://gepia.cancer-pku.cn). Statistical significance was calculated using one-way ANOVA. *$P < 0.001$.

Then, I analyzed single-cell RNA sequencing (scRNAseq) data from a previous study of PDAC specimens (Werba et al., 2023) to identify cell types that express GPx4. Unsupervised, graph-based clustering and visualization using uniform manifold approximation and projection (UMAP) for a total of 94,929 cells revealed seven distinct cell clusters, which were annotated based on canonical markers (Figure 26A). These clusters represented cancer epithelial, endothelial, mesenchymal, myeloid, T/NK (T and NK cells), B/plasma cells, and mast cells (Figure 26B).

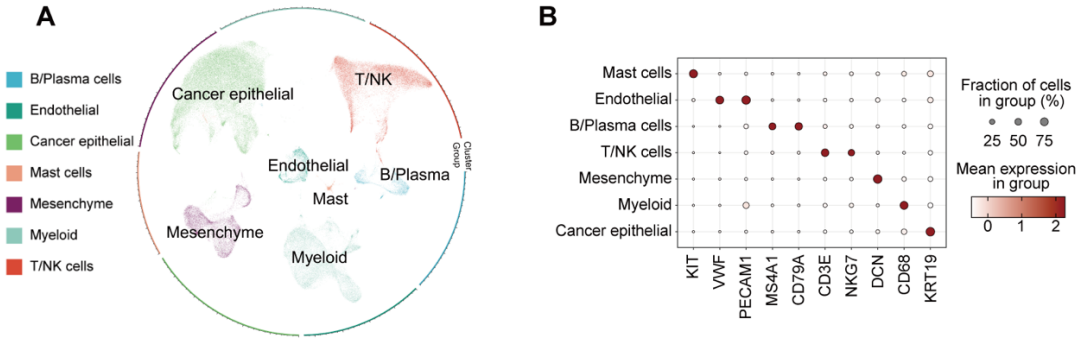

Figure 26. Single-cell analysis revealed the transcriptomic landscape in PDAC. **(A)** UMAP visualization of 94,929 cells from human PDAC samples. Cells were clustered into seven types based on transcriptomic profiles. NK, natural killer. **(B)** A dotplot displaying canonical marker genes used to identify the clusters. The size of each dot corresponds to the fraction of cells within each cluster expressing the respective marker gene, while the color intensity indicates the mean expression level within the cluster.

This analysis revealed that cancer epithelial cells possessed a large population of cells expressing high levels of *GPx4* (Figure 27A), suggesting that these cells might be particularly susceptible to GPx4 inhibition. However, recognizing that *GPx4* expression alone may not fully capture GSH metabolism, for which *GPx4* is essential, I extended the investigation to the GSH metabolism-related genes. It is found that cancer epithelial cells exhibited elevated expression levels of GSH metabolism genes, distinguishing them from other cell types in their susceptibility to oxidative stress (Figure 27B).

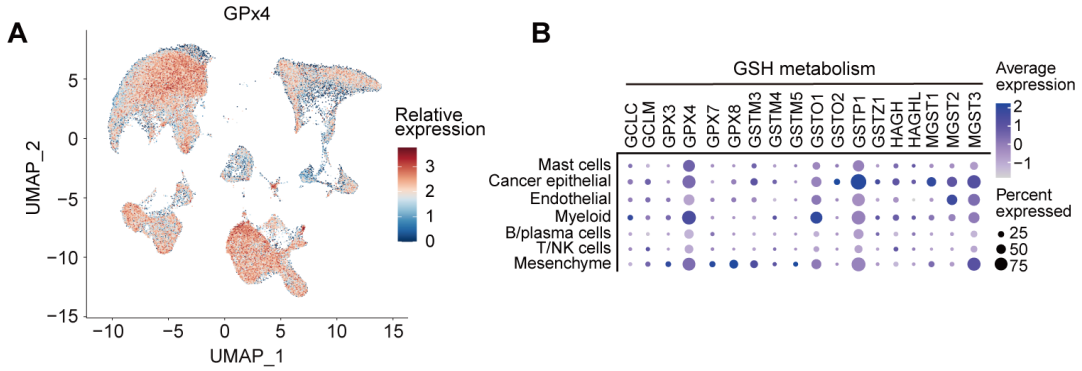

Figure 27. Cancer epithelial cells exhibited elevated expression levels of *GPx4* and other GSH metabolism-related genes. (A) A feature plot depicting the relative expression of *GPx4* across all cell clusters. Cancer epithelial cells exhibited elevated GPx4 expression compared to other cell types, suggesting their potential vulnerability to GPx4 inhibition. **(B)** A dotplot showing the expression of genes involved in GSH metabolism across different cell types. Cancer epithelial cells displayed higher expression levels of these GSH metabolism-related genes, further reinforcing their potential susceptibility to ferroptosis.

Given that GPx4 inhibition is one of the classical methods for triggering ferroptosis (Liu et al., 2021a), I calculated module scores for GSH metabolism and ferroptosis across different cell types in PDAC to quantitatively assess the vulnerability of tumor cells to GSH interference and ferroptosis induction. Consequently, cancer epithelial cells exhibited the highest scores in GSH (Figure 28) and the second highest ferroptosis scores (Figure 29). These results suggest that cancer epithelial cells are particularly vulnerable to therapies targeting the GSH cycle and ferroptosis induction. I also noted that myeloid cells had the highest ferroptosis module scores (Figure 29A), likely reflecting the presence of macrophages processing cancer cell debris (Wu et al., 2023).

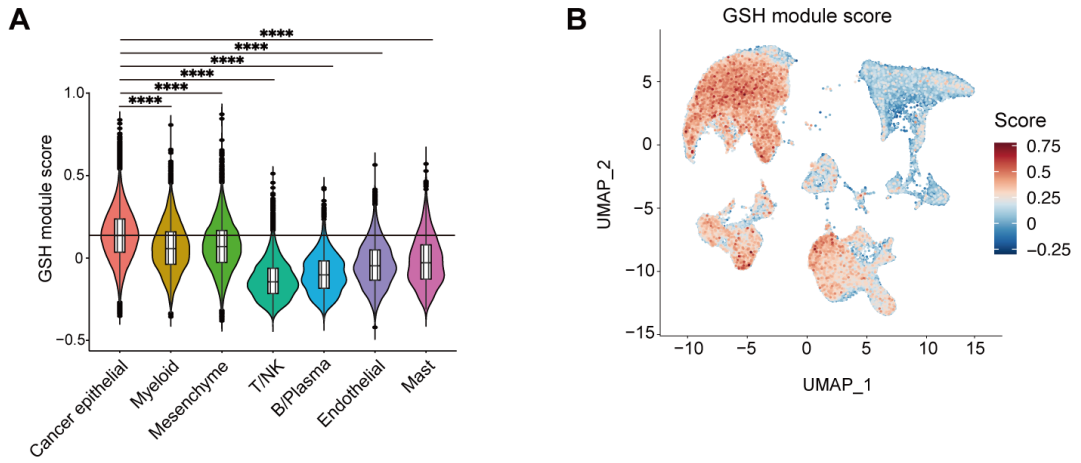

Figure 28. Cancer epithelial cells exhibited the highest scores in GSH modules. **(A)** A violin plot quantifying GSH module scores across the seven cell types. Cancer epithelial cells exhibited significantly higher GSH module scores compared to other cell types, indicating their reliance on GSH metabolism for survival. Statistical significance was calculated by Wilcoxon rank-sum test. ****$P < 0.0001$. **(B)** A feature plot visualizing GSH module scores across all cell clusters, highlighting variations in GSH metabolism activity within different cell populations.

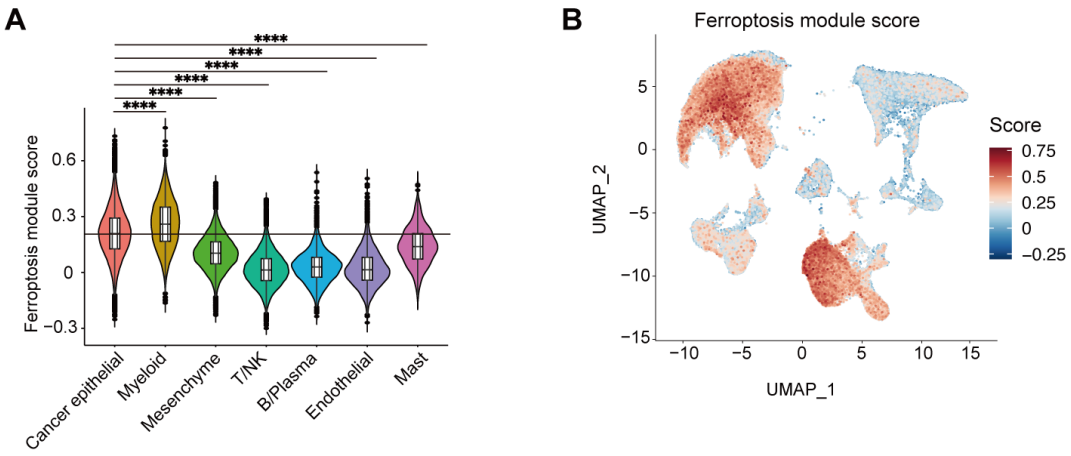

Figure 29. Cancer epithelial cells exhibited the second-highest scores in ferroptosis modules. (A) A violin plot quantifying ferroptosis module scores across the seven cell types. Both cancer epithelial cells and myeloid cells exhibited significantly elevated ferroptosis module scores, suggesting their potential sensitivity to ferroptosis induction. Statistical significance was calculated by Wilcoxon rank-sum test. ****$P < 0.0001$. **(B)** A feature plot visualizing ferroptosis module scores across all cell clusters.

To sum up, the single-cell transcriptomic analysis suggests that human PDAC exhibits a gene expression profile that renders it sensitive to GPx4 inhibition and ferroptosis induction. Cancer epithelial cells show both high GSH metabolism activity and a propensity for ferroptosis, indicating that targeting GPx4 could be an effective therapeutic strategy for PDAC.

4. Dual inhibition of GPx4 and MEK by the combination of ML210 and trametinib as a potential therapeutic strategy for PDAC

While ML210 and trametinib demonstrated their therapeutic potential in fly models, it was essential to assess their efficacy against PDAC in mammalian systems. I began by testing the MT combination in AsPC-1 PDAC cell colonies grown in soft agar. Results showed that their combination (hereafter abbreviated as MT) significantly reduced colony number and size compared to ML210 alone, indicating a strong anti-proliferative effect (Figure 30).

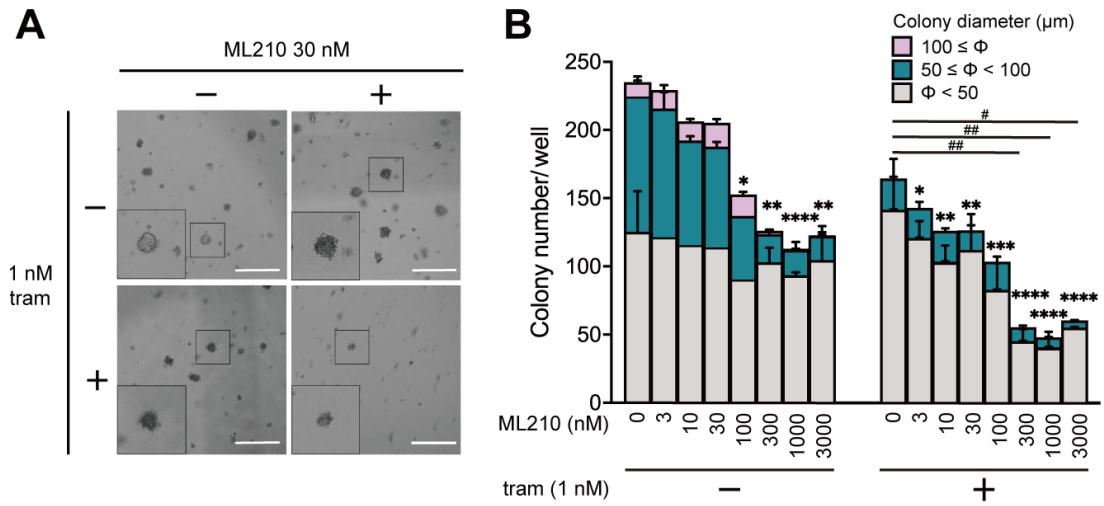

Figure 30. The combination of ML210 and trametinib inhibited colony formation of AsPC-1 cells in soft agar. (A) Representative images of AsPC-1 colony formation in soft agar. AsPC-1 cells were cultured in ML210, trametinib, or the ML210 and trametinib combination (MT) for seven days. Scale bars, 500 μm. **(B)** Quantification of the number and size of AsPC-1 colonies in soft agar after treatment with ML210 and/or trametinib for seven days. Statistical significance was assessed using one-way ANOVA with post-hoc Dunnett's multiple comparisons test. *P < 0.05, **P < 0.01, ***P < 0.001, ****P < 0.0001 compared to vehicle without trametinib, $^{\#}P < 0.05$, $^{\#\#}P < 0.01$ compared to the trametinib group.

To further validate these effects, I treated AsPC-1 spheroids with MT and confirmed its efficacy in inhibiting proliferation (Figure 31A). Then, I evaluated their synergistic effects by analyzing the spheroid data for ZIP synergy score. This analysis revealed that ML210 and trametinib exhibited synergistic suppression of AsPC-1 cell proliferation (Figure 31B).

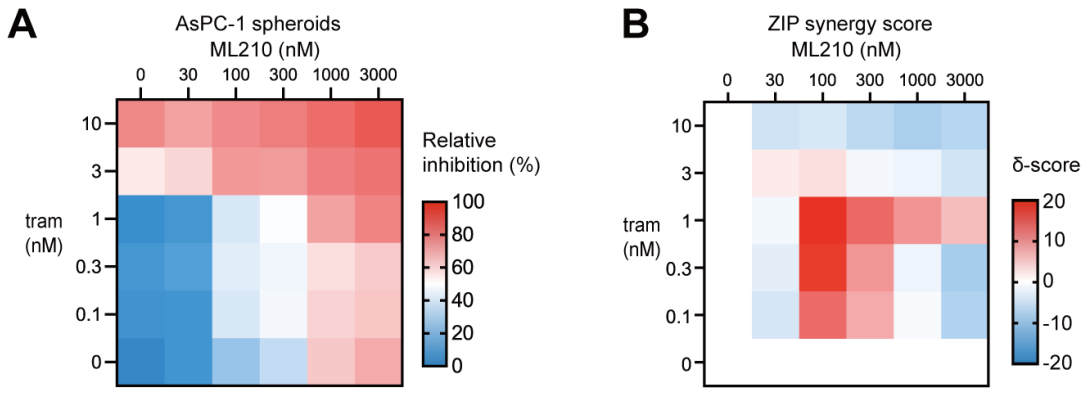

Figure 31. The MT combination inhibits proliferation of AsPC-1 cells in spheroid assays and demonstrates synergistic effects. (A) Heatmap depicting the relative inhibition of spheroid volume of AsPC1 cells in response to varying dose combinations of ML210 and trametinib. **(B)** Synergistic suppression of spheroid volume in AsPC-1 cells by ML210 and trametinib. The ZIP synergy score, calculated based on the relative inhibition of spheroid volume in AsPC1 cells, was used to generate a heatmap for the MT combination.

Given the significant anti-proliferative effects of MT in AsPC-1 cells carrying the *4-hit* genotype (*KRAS*^{G12D}, *TP53*^{LOF}, *CDKN2A*^{LOF}, and *SMAD4*^{LOF}), I subsequently investigated MT's efficacy in additional PDAC cell lines with diverse genotypes to assess genotype specificity. I selected two further lines: Capan-1, which lacks *SMAD4*^{LOF} and represents a *3-hit* genotype, and Panc-1, which carries *KRAS*^{G12V} within its *4-hit* genotype (Table 8) (Sekiya et al., 2023).

Table 8. Somatic mutations in PDAC cell lines. Genomic sequences of *KRAS*, *TP53*, *CDKN2A* and *SMAD4* were analyzed by PCR for PDAC cell line AsPC1, Capan-1 and

Panc-1. Genes for which PCR did not amplify expected fragments were determined as homozygously deleted (HD), which was further confirmed by RT-qPCR. Wt, wild-type; Ser-Stop, serine to stop codon; Cys-fs, cysteine to frameshift; Thr-fs, threonine to frameshift. Table adapted from Sekiya et al, 2023.

Cell line	*KRAS*		*TP53*		*CDKN2A*		*SMAD4*		No. of mutations
	Alteration	Predicted product	Alteration	Predicted product	Alteration	Predicted product	Alteration	Predicted product	
AsPC-1	12 GGT-GAT	Gly to Asp	135 TGC-GC	Cys-fs	27 ACT-A	Thr-fs	100 AGG-ACG	Arg-Thr	4
Capan-1	12 GGT-GTT	Gly to Val	159 GCC-GTC	Ala to Val	HD	absent	343 TCA-TGA	Ser-Stop	4
Panc-1	12 GGT-GAT	Gly to Asp	273 CGT-CAT	Arg to His	HD	absent	none	Wt	3

Intriguingly, MT displayed differential efficacy across these cell lines. While MT strongly inhibited proliferation in AsPC-1 and Panc-1 cells, it was less effective in Capan-1 cells (Figures 31A, 32A, and 32C). Furthermore, MT exhibited a marked synergistic effect on Capan-1 cells but not Panc-1 cells (Figure 32B, 32D). Collectively, these findings suggest that MT's efficacy may depend on the *4-hit* genotype involving $KRAS^{G12D}$, which aligns with the genotype used in our initial fly model experiments.

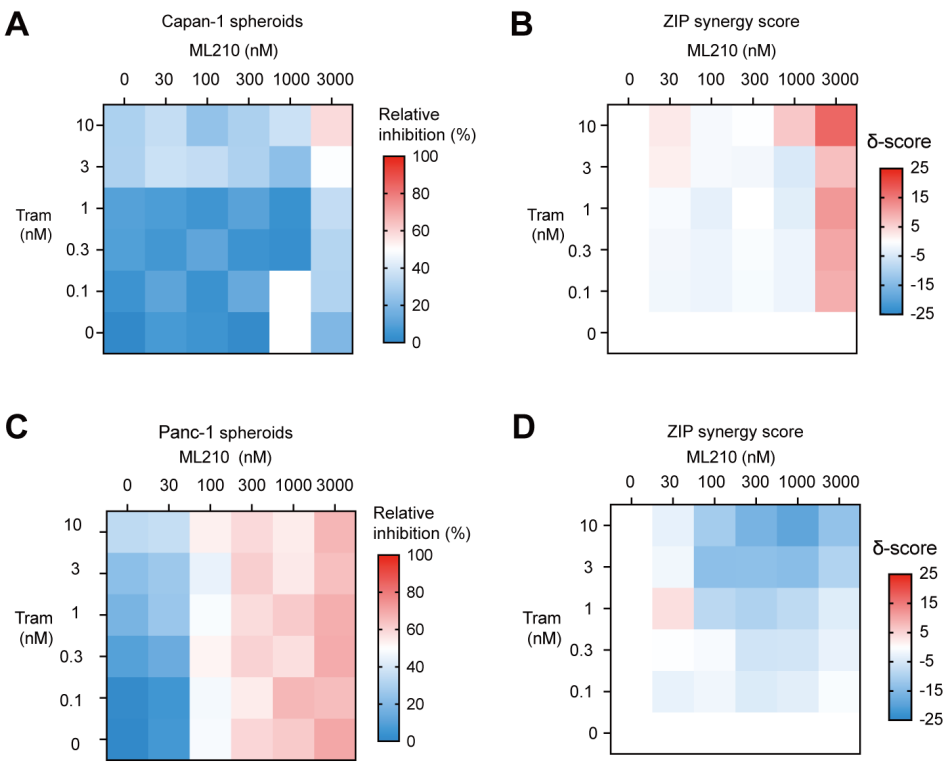

Figure 32. The inhibitory effect of MT on proliferation of Capan-1 and Panc-1 cells in spheroid assays differs from its effect on AsPC-1 cells. (A) Heatmap depicting the relative inhibition of spheroid volume of Capan-1 cells in response to varying dose combinations of ML210 and trametinib. **(B)** Synergistic suppression of spheroid volume in Capan-1 cells by ML210 and trametinib. **(C)** Heatmap depicting the relative inhibition of spheroid volume of Panc-1 cells in response to varying dose combinations of ML210 and trametinib. **(D)** Synergistic suppression of spheroid volume in Panc-1 cells by ML210 and trametinib.

To validate the therapeutic efficacy of MT against PDAC in mammals at a whole-body level, I utilized an orthotopic xenograft mouse model. AsPC-1 cells expressing luciferase (AsPC-1-Luc) were implanted in the pancreas of immunodeficient mice to allow for bioluminescence-based tumor growth monitoring. I first established the maximum tolerated doses (MTD) of ML210 and trametinib and found that ML210 at 40 mg/kg/day, alone or combined with trametinib at 1.0 mg/kg/day, was safe (Figure 33).

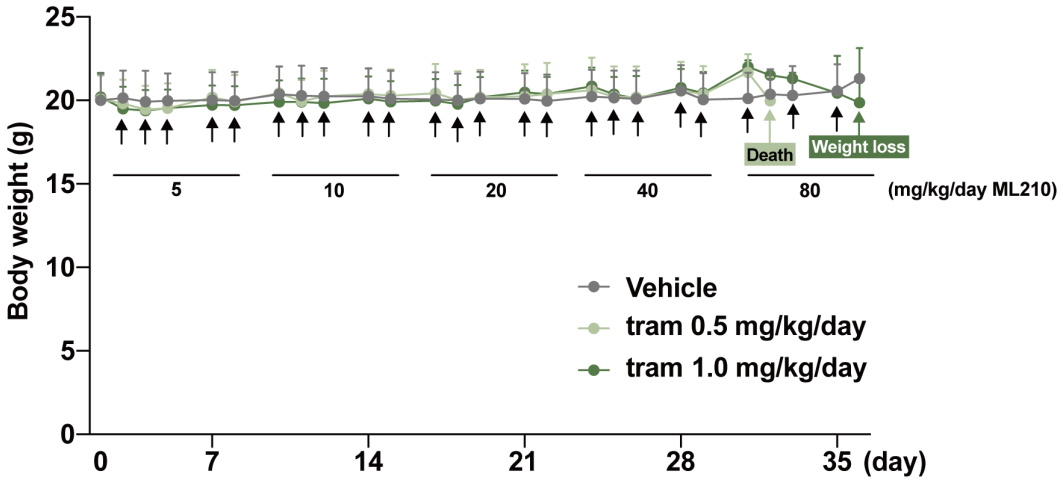

Figure 33. MTD determination for the combination of ML210 and trametinib (tram) in mice. Five female BALB/c-nu/nu mice were administered orally with tram at a fixed dose of 0.5 mg/kg/day or 1.0 mg/kg/day and intraperitoneally with increasing doses of ML210 starting at 5 mg/kg/day (arrows) and observed for the following 7 days. The dose was gradually escalated up to 80 mg/kg/day of ML210 and decrease of body weight and death after chemical happened at 80 mg/kg/day. Arrows, dose of ML210 and tram five times a week. Error bars, SD.

Then a pharmacokinetic assay of ML210 was conducted at single dose of 10 mg/kg. ML210 demonstrates favorable characteristics, including efficient absorption, substantial systemic exposure, and plasma concentrations exceeding the effective dose in 3D culture of AsPC-1 cells (Table 9). These findings strongly support the potential efficacy of ML210 in preclinical models and its further development as a therapeutic candidate.

Table 9. Pharmacokinetic properties of ML210.

Male ICR mice were administered ML210 at a dose of 10 mg/kg via intraperitoneal injection, and plasma concentrations were measured at 0.083, 0.25, 0.5, 1, 2, 4, 8, and 24-hours post-dosing. $T_{1/2}$ the half-life, $T_{max,}$ the time to reach the maximum plasma concentration. $C_{max,}$ the maximum plasma concentration. $AUC_{0\text{-}24}$, the area under the plasma concentration-time curve from 0 to 24 hours. $AUC_{0-\infty}$, the area under the plasma concentration-time curve extrapolated to infinity. $MRT_{0-\infty}$, the mean residence time extrapolated to infinity.

Compound	**Dose**	**$T_{1/2}$**	**T_{max}**	**C_{max}**	**$AUC_{0\text{-}4}$**	**$AUC_{0\text{-}\infty}$**	**$MRT_{0\text{-}\infty}$**
	mg/kg	h	h	nM	nM*h	nM*h	h
ML210	10	6.1	1	923.3	4405.9	4646.4	6.6

Hence, for therapeutic assays, I chose 10 mg/kg and 40 mg/kg as the doses of ML210 to be treated intraperitoneally and 0.5 mg/kg trametinib orally for four weeks. During the assay, I evaluated tumor growth weekly by measuring bioluminescence signal intensities using *in vivo* imaging in the presence of luciferin. Weekly imaging revealed that MT significantly suppressed xenograft tumor growth relative to either agent alone (Figure 34), underscoring the synergy between ML210 and trametinib in reducing PDAC tumor progression.

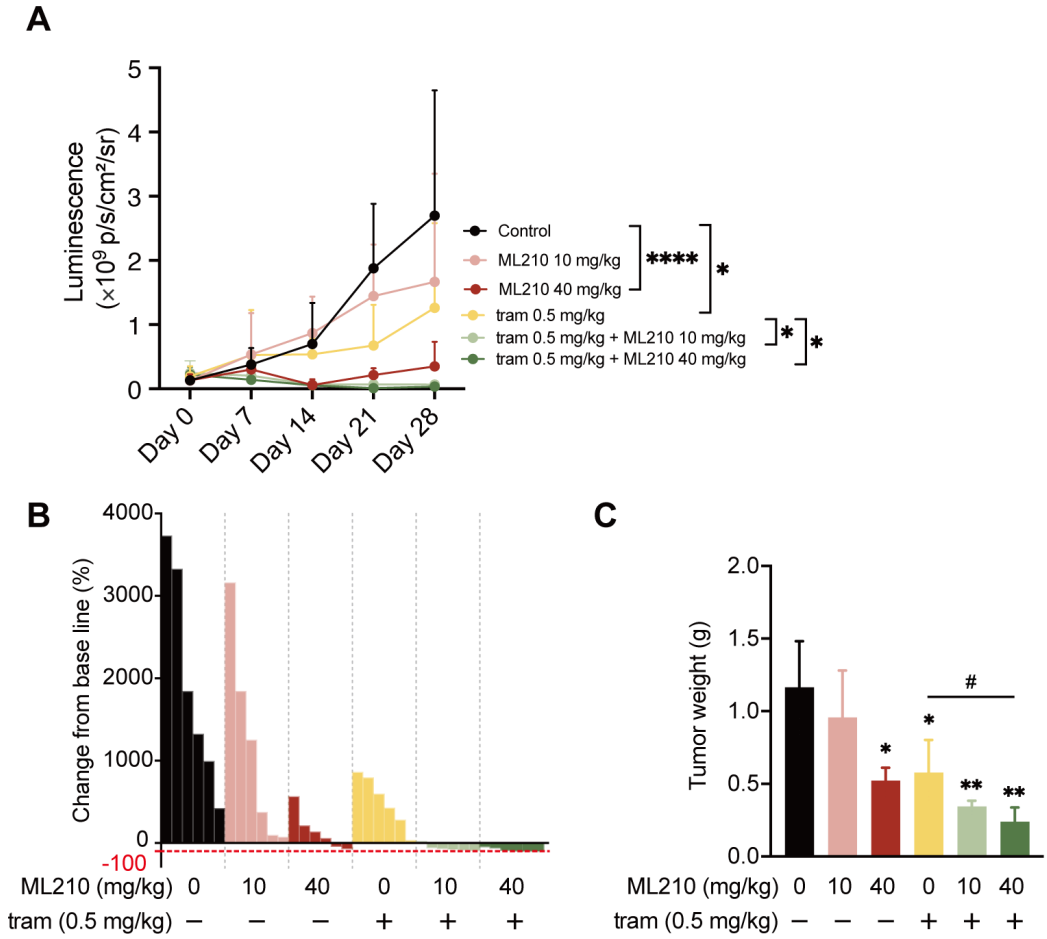

Figure 34. The ML210 and trametinib (MT) combination exerts anti-tumor effects on orthotopic PDAC xenografts in mice. (A) MT significantly suppressed the growth of AsPC-1 orthotopic xenografts over the course of four weeks. Tumor growth was monitored using bioluminescence imaging. Data are presented as mean tumor volume + SD for six mice per group. **P* <0.05, *****P* < 0.0001 compared with control in two-way ANOVA with post-hoc Tukey HSD test. **(B)** MT inhibited xenograft growth effectively. A waterfall plot illustrates the percentage change in

tumor volume on day 28 relative to the pretreatment baseline for each group, with each bar representing an individual mouse. **(C)** MT treatment group showed a significant reduction in tumor weight compared to the control group. Tumor weights were measured after the mice were sacrificed on day 29, one day following the completion of the four-week treatment. Data are presented as mean + SD for six mice per group. *$P < 0.05$, **$P < 0.01$, compared with control, $^{\#}P < 0.05$ compared with tram alone group in one-way ANOVA with post-hoc Tukey HSD test.

Importantly, MT administration caused no significant reduction in mouse body weight, suggesting that the regimen is well-tolerated (Figure 35).

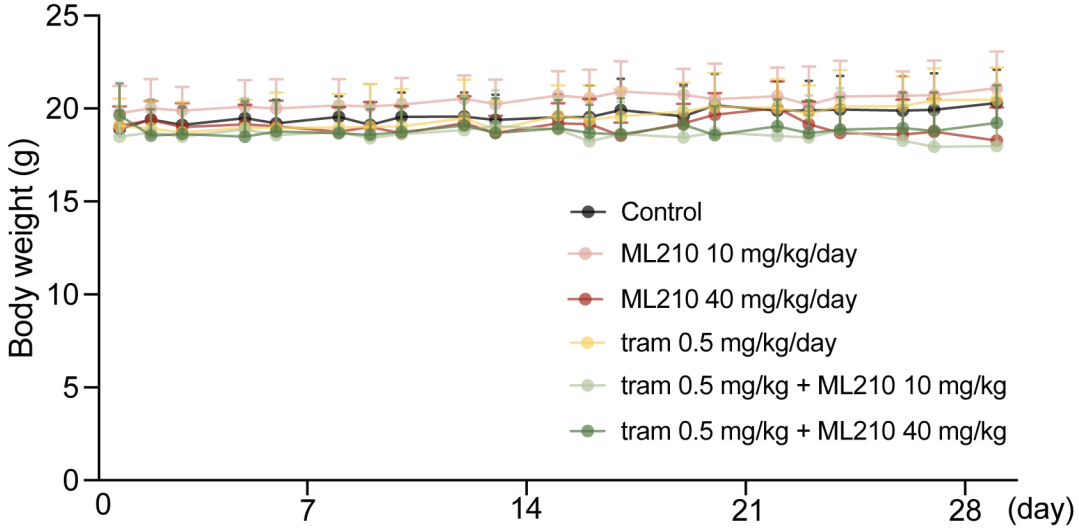

Figure 35. Tolerance of MT in xenograft mice. Over a four-week period, no significant body weight changes were observed in MT-treated mice as compared with vehicle control. Error bars, SD.

In conclusion, these findings validate the potential of dual GPx4 and MEK inhibition as a therapeutic approach for PDAC, particularly in genotypes driven by *KRAS*^{G12D}.

5. The combination of ML210 and trametinib inhibits PDAC cell viability by inducing ferroptosis

To explore the mechanisms of action of *GPx4* inhibition, I investigated whether ferroptosis was induced by targeting GPx4, as GPx4 has been reported to protect cells from ferroptosis by reducing lipid hydroperoxides to non-toxic lipid alcohols (Lei et al., 2024). Since ferroptosis is uniquely dependent on intracellular iron and ROS, I assessed the impact of the ferroptosis inhibitor Ferrostatin-1 (Fer-1) and the iron chelator Deferoxamine mesylate (DFO) on spheroid formation. Fer-1, a ROS scavenger, inhibited spheroid suppression in trametinib-treated *GPx4*-knockdown AsPC-1 cells (Figure 36A). In *GPx4*-knockdown AsPC-1 cells, ROS levels were significantly elevated compared to control cells, indicating that GPx4 suppression increases oxidative stress (Figure 36B). While trametinib treatment alone did not significantly elevate ROS levels in AsPC-1 cells without *GPx4* knockdown, it caused a marked increase in ROS levels in *GPx4*-knockdown AsPC-1 cells, particularly those transfected with si*GPx4* #1. This finding suggests that GPx4 suppression sensitizes cells to trametinib-induced oxidative stress. Furthermore, treatment with the antioxidant Fer-1 effectively reduced ROS levels in trametinib-treated *GPx4*-knockdown AsPC-1 cells, which show no significant difference compared to control cells.

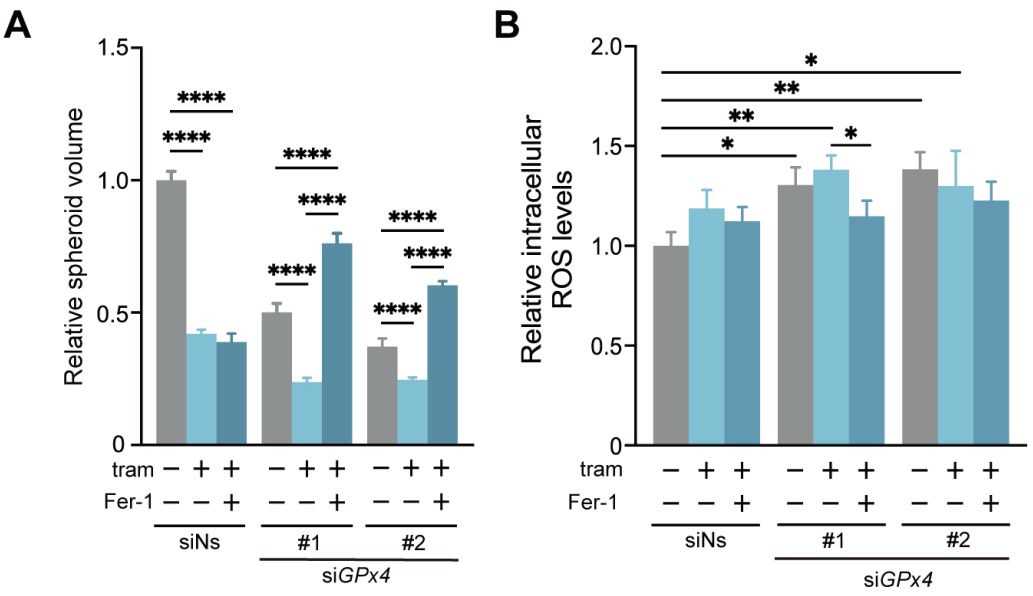

Figure 36. Fer-1 inhibits spheroid suppression in trametinib-treated *GPx4*-knockdown AsPC-1 cells. (A) *GPx4* knockdown significantly reduced spheroid volume, which was partially rescued by Fer-1 (10 μM) in combination with trametinib (3 nM) for 48 hours. AsPC-1 cells were initially transfected with *GPx4*-specific siRNAs for 48 hours, then seeded at 1,000 cells per well in cell-repellent 96-well plates to form spheroids over a 72-hour period. The relative spheroid volume was analyzed following treatment. **(B)** Combined *GPx4* Knockdown and trametinib treatment elevated ROS levels in AsPC-1 cells, with attenuation by antioxidant Fer-1. *GPx4* knockdown AsPC-1 cells were treated with trametinib (3 nM), and Fer-1 (10 μM) for 48 hours, after which intracellular ROS levels were measured by using DCFH-DA fluorescence. Error bars, SD in technical triplicate. *$P < 0.05$, **$P < 0.01$, ****$P < 0.0001$ in one-way ANOVA with post-hoc Tukey HSD test.

Although the efficacy of DFO was less prominent than that of Fer-1, DFO significantly reversed the spheroid suppression effects (Figure 37A), along with corresponding changes in iron accumulation. Trametinib-treated *GPx4*-knockdown AsPc-1 cells also showed elevated iron levels (Figure 37B), indicating that dual inhibition of GPx4 and MEK in PDAC cells promotes ferroptosis via ROS and iron accumulation. These results indicate that *4-hit* PDAC exhibits a particular vulnerability to ferroptosis induced by the dual inhibition of GPx4 and MEK.

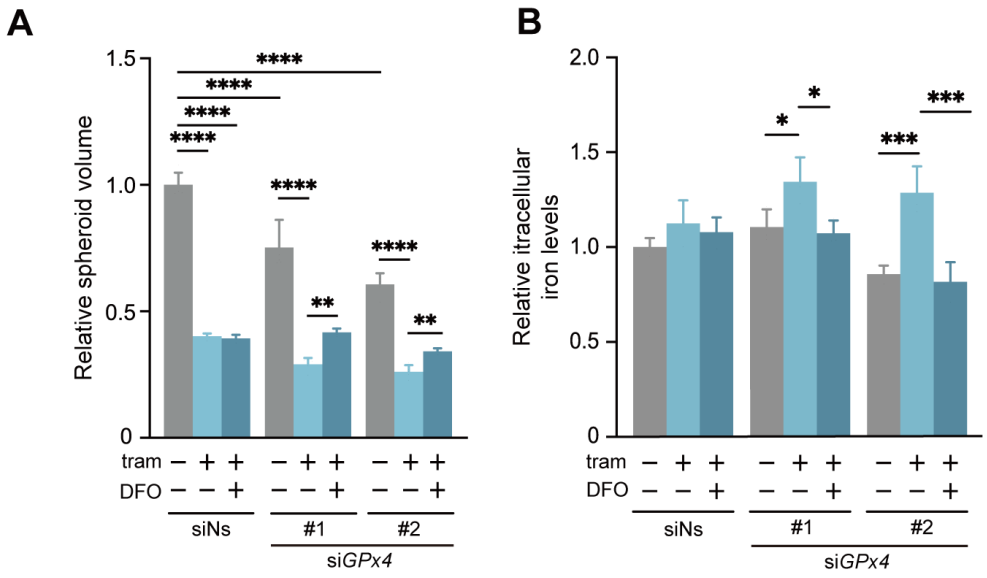

Figure 37. DFO inhibits spheroid suppression in trametinib-treated *GPx4*-knockdown AsPC-1 cells. (A) *GPx4* knockdown significantly reduced spheroid volume, which were partially rescued by DFO (10 μM) in combination with trametinib (3 μM) for 24 hours. AsPC-1 cells were first transfected with *GPx4*-specific siRNAs for 48 hours, then seeded at 100 cells per well in cell-repellent 96-well plates to establish spheroids over 72 hours. The relative spheroid volume was analyzed after treatment. **(B)** *GPx4*-knockdown AsPC-1 cells exhibited increased iron levels in AsPC-1 cells, which were suppressed by DFO treatment. AsPC-1 cells were pre-treated with DFO and trametinib for 24 hours, followed by measurement of intracellular iron levels using FerroOrange fluorescence. Error bars, SD in technical triplicate. *$P < 0.05$, **$P < 0.01$, ***$P < 0.001$, ****$P < 0.0001$ in One-way ANOVA with post-hoc Tukey HSD test.

With evidence of ferroptosis induction in *GPx4* knockdown AsPC-1 cells, I next investigated whether ferroptosis contributes to the anti-proliferative effect of MT treatment. I hypothesized that MT exerts its synergistic effect by inducing ferroptosis in AsPC-1 cells. This hypothesis is based on previous findings reporting ML210 as a ferroptosis inducer (Hangauer et al., 2017). To explore this further, I employed Erastin, which reduces GSH level by directly inhibiting cystine/glutamate antiporter System X_c^- activity (Zhao et al., 2020; Xie et al., 2016) (Figure 38), in combination with trametinib in AsPC-1 cells. Consistent with my hypothesis, erastin exhibited an antiproliferative effect in AsPC-1 cells similar to that of ML210 when combined with trametinib (Figure 39). These findings indicate that AsPC-1 cells are sensitive to ferroptosis induction by erastin, further supporting my hypothesis that ML210 also acts as a ferroptosis inducer in AsPC-1 cells.

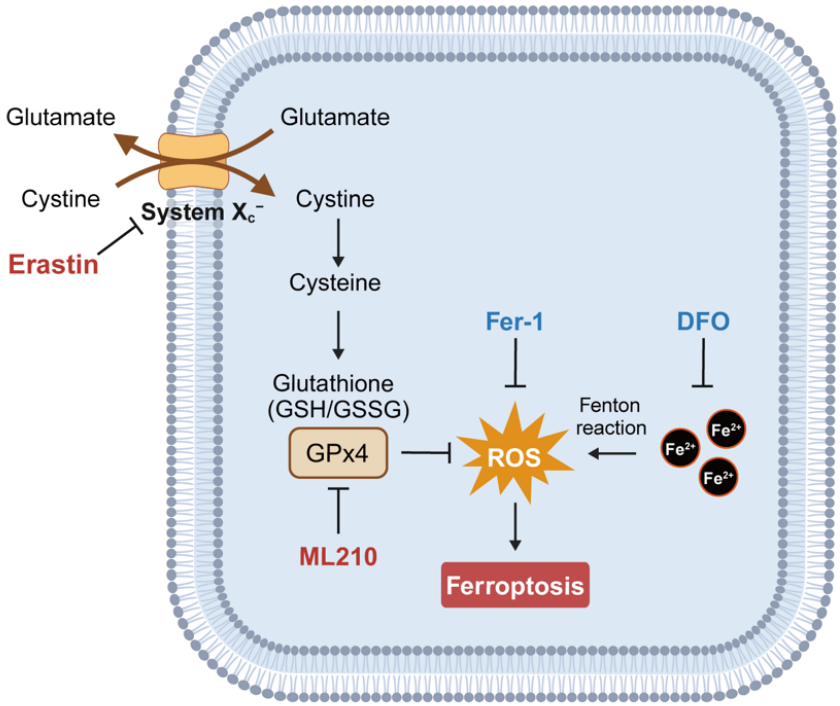

Figure 38. Schematic overview of the molecular mechanism of ferroptosis. Ferroptosis is an iron- and ROS-dependent form of regulated cell death. Erastin inhibits the cystine/glutamate antiporter System X_c^-, blocking cystine uptake and subsequently depleting intracellular cysteine, which is required for GSH synthesis.

GPx4 reduces lipid peroxides depending on GSH. ML210 targets GPx4 leading to ROS accumulation, thereby drives ferroptosis. The ferroptosis inhibitors Fer-1 and DFO counteract this process: Fer-1 reduces intracellular ROS level, while DFO chelates iron, preventing ROS generation through the Fenton reaction. The figure was adapted from Xie et al., 2016.

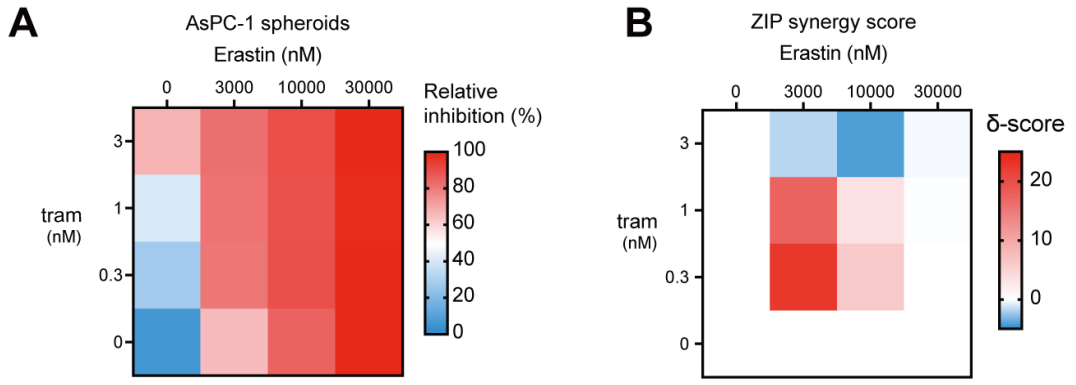

Figure 39. The combination of the ferroptosis inducer erastin and trametinib inhibits proliferation of AsPC-1 cells in spheroid assays and demonstrated synergistic effects. (A) Heatmap depicting the relative inhibition of spheroid volume of AsPC-1 cells in response to varying dose combinations of erastin and trametinib. **(B)** Synergistic suppression of spheroid volume in AsPC-1 cells by erastin and trametinib. The ZIP synergy score, calculated based on the relative inhibition of spheroid volume, was used to generate the heatmap for the combination of erastin and trametinib.

To confirm ferroptosis in MT-treated AsPC-1 cells, I utilized Fer-1 and DFO in spheroid assays. Upon the addition of Fer-1 and DFO, I observed a significant rescue of spheroid volume in AsPC-1 cells treated with either ML210 alone or MT (Figure 40A and 41A), suggesting that ML210 and MT treatments induced ferroptosis to suppress spheroid formation. Consistently, MT elevated intracellular ROS and iron levels, which were abrogated by Fer-1 or DFO (Figure 40B and 41B). Notably, MT caused higher ROS levels than ML210 alone, indicating that MT's ROS-driven oxidative stress may be critical for suppressing PDAC cell growth. Additionally, iron

accumulation was more pronounced in trametinib-treated cells (Figure 41B). Given that iron continuously generates ROS via Fenton reaction during ferroptosis (Illés et al., 2020), it is possible that trametinib triggers intense intracellular oxidative stress by promoting iron accumulation.

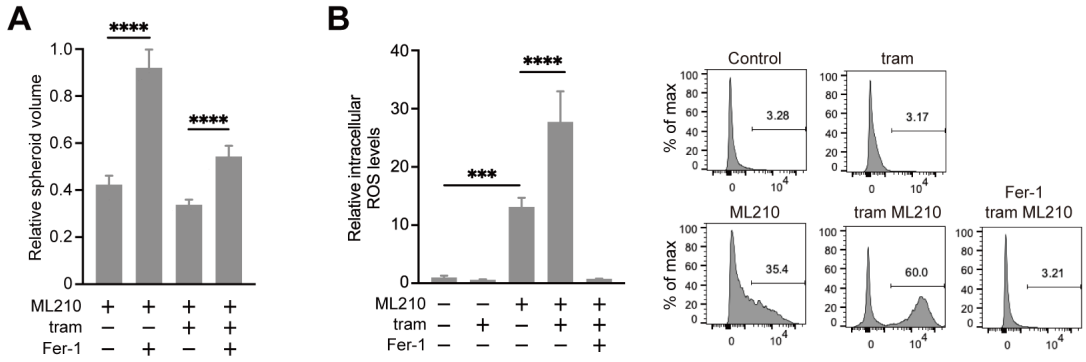

Figure 40. The inhibitory effect of MT in AsPC-1 spheroids is ROS-dependent. **(A)** The MT combination significantly reduced spheroid volume compared to individual treatments, while Fer-1 significantly suppressed the reduction. The relative spheroid volume of AsPC-1 cells treated with ML210, trametinib, and additional Fer-1 was analyzed 48 hours after initiating the treatments. **(B)** MT significantly elevated ROS levels compared to individual treatments, while Fer-1 reduced the ROS levels induced by the MT combination. AsPC-1 cells were treated with ML210, trametinib, and Fer-1 for 48 hours, after which intracellular ROS levels were measured by using DCFH-DA fluorescence. The histograms on the right illustrate the fluorescent intensity of DCFH-DA under different treatment conditions. Error bars, SD in technical triplicate. ***$P < 0.001$, ****$P < 0.0001$ in One-way ANOVA with post-hoc Tukey HSD test.

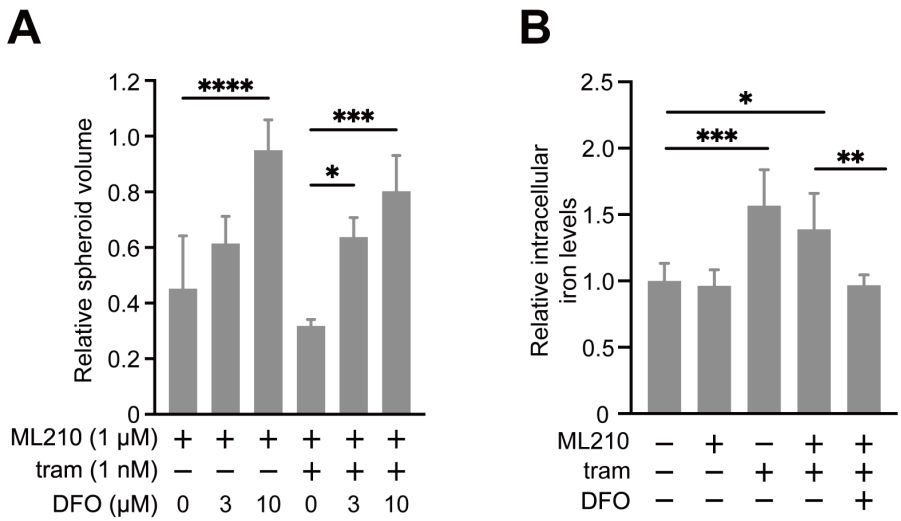

Figure 41. The inhibitory effect of MT in AsPC-1 spheroids is iron-dependent. **(A)** DFO significantly rescued the volume suppression induced by ML210 alone and the MT combination. The relative spheroid volume of AsPC-1 cells treated with ML210, trametinib, and DFO was analyzed 24 hours after initiating the treatments. **(B)** The MT combination increased iron level in AsPC-1 cells, which were suppressed by DFO treatment. AsPC-1 cells were pre-treated with ML210 (1 μM), trametinib (1 nM) and DFO (10 μM) for 24 hours, followed by measurement of intracellular iron levels using FerroOrange fluorescence. *$P < 0.05$, **$P < 0.01$, ***$P < 0.001$, ****$P < 0.0001$ in One-way ANOVA with post-hoc Tukey HSD test.

Collectively, these findings suggest that MT effectively induces ferroptosis to inhibit PDAC cell proliferation. The increased ROS production and iron accumulation underscore the importance of targeting both GPx4 and MEK to maximize anti-tumor efficacy.

Since MT triggered ferroptosis in cultured AsPC-1 cells, I investigated whether ferroptosis was also induced in MT-treated xenografts. Hematoxylin and eosin (H&E) staining demonstrated the accumulation of cytosolic vacuoles, suggesting extensive cell death in MT group (Figure 42).

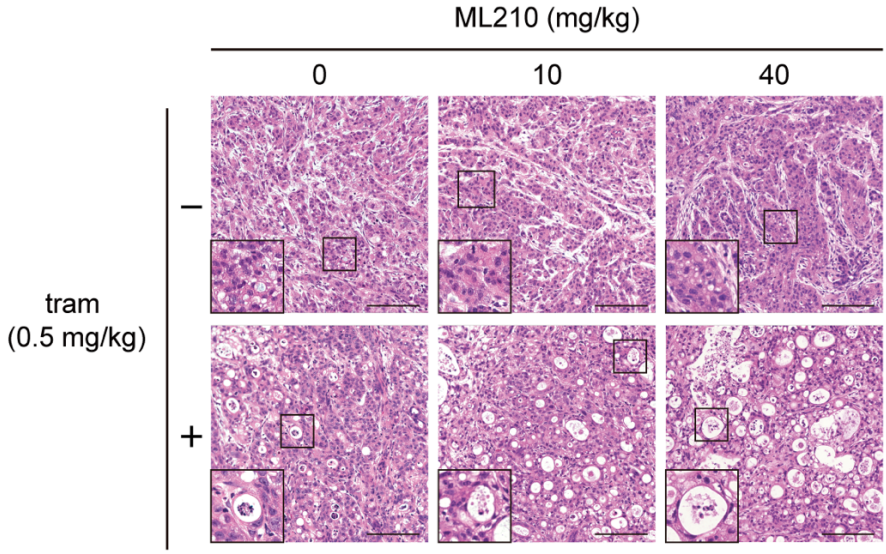

Figure 42. MT-treated AsPC-1 xenografts exhibit extensive cell death. Tumor samples were collected and fixed immediately after sacrifice on day 29, followed by H&E staining. Scale bars: 100 μm.

Ferroptosis is characterized by lipid peroxidation, leading to elevated levels of the lipid peroxidation marker, 4-hydroxynonenal (4-HNE) (Zarkovic, 2003). Therefore, I investigated 4-HNE within the tumors and observed aberrant accumulation of peroxidized lipids in dead cells in MT group (Figure 43).

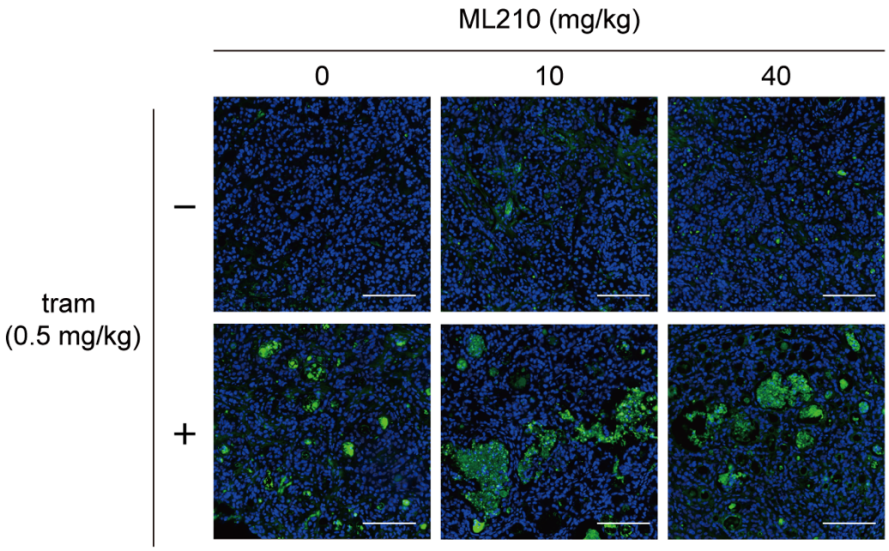

Figure 43. MT-treated AsPC-1 xenografts exhibit elevated lipid peroxidation levels. Immunofluorescence staining for 4-HNE showed elevated lipid peroxidation in the MT treatment group compared to ML210 or trametinib treatments alone. Scale bars: 100 μm.

Additionally, immunohistochemical staining for cleaved Caspase 3 (CC3), the apoptosis marker, revealed significantly less aggregation of CC3-positive cells in MT group than trametinib alone group (Figure 44), indicating that MT-induced cell death occurred without the activation of pro-apoptotic caspases. Intriguingly, tumors treated with trametinib alone exhibited CC3 aggregation in dying cells. This finding is consistent with the widely acknowledged conclusion that trametinib induces apoptosis in cancer cells (Caunt et al., 2015).

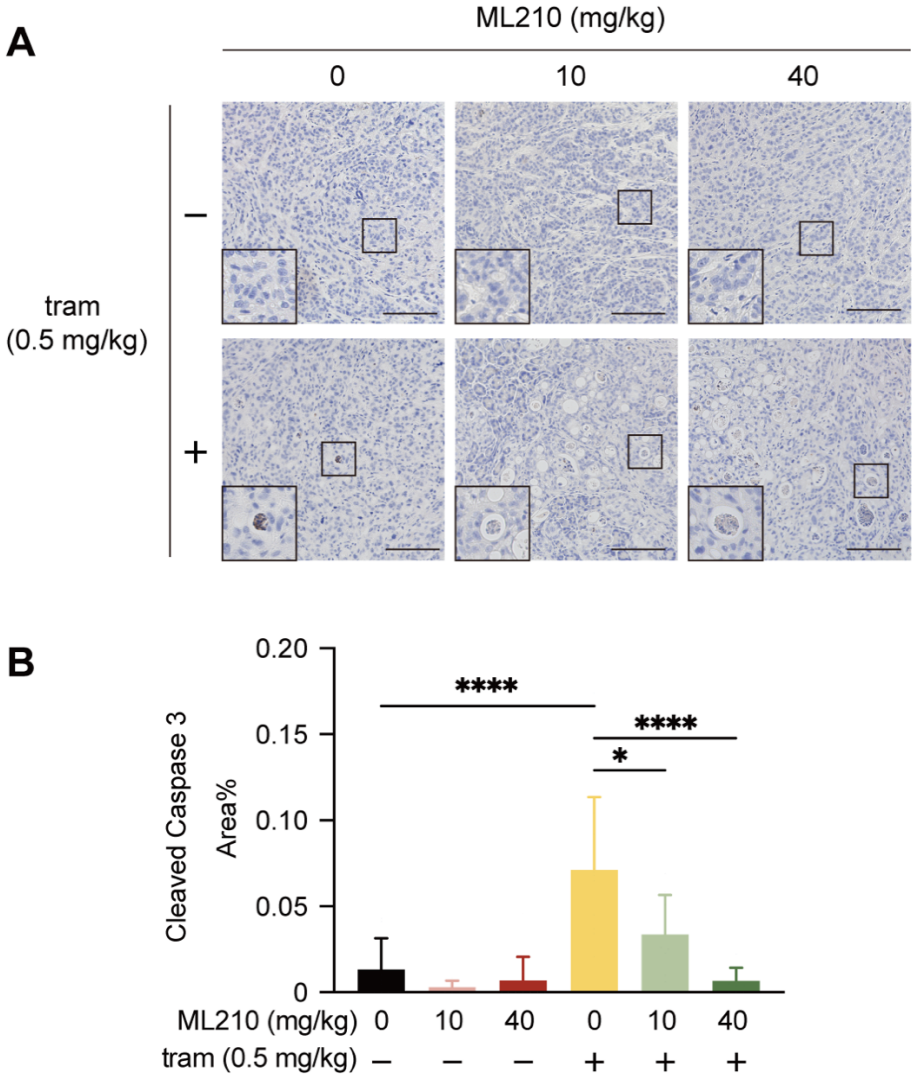

Figure 44. MT-treated AsPC-1 xenografts exhibit non-apoptotic cell death. (A) Minimal accumulation of CC3 was observed following treatment with either ML210 or the MT combination, indicating that apoptosis was not the predominant form of cell death in these treatment groups. Scale bars: 100 μm. **(B)** Quantification of CC3-

positive areas in AsPC-1 xenografts. Data are presented as mean + SD for six mice per group. *$P < 0.05$, ****$P < 0.0001$ compared with control in one-way ANOVA with post-hoc Tukey HSD test.

Collectively, these results suggest that simultaneous inhibition of GPx4 and MEK exerts anti-PDAC effects by inducing ferroptosis. In PDAC cells with activated KRAS, glutathione metabolism pathway is upregulated, with elevated GPx4 playing a crucial role in enhancing antioxidant defenses, thereby protecting them from ROS and supporting their survival (Xue et al., 2023; Eling et al., 2015; Li et al., 2022). In contrast, MEK inhibition induces ferritinophagy, leading to the release of lysosomal iron into the cytoplasm (Ravichandran et al., 2022). Together, dual inhibition of MEK and GPx4 results in an overwhelming accumulation of ROS, surpassing the cell's antioxidant capacity, causing lipid peroxidation, and ultimately triggering ferroptotic death of PDAC cells (Figure 45).

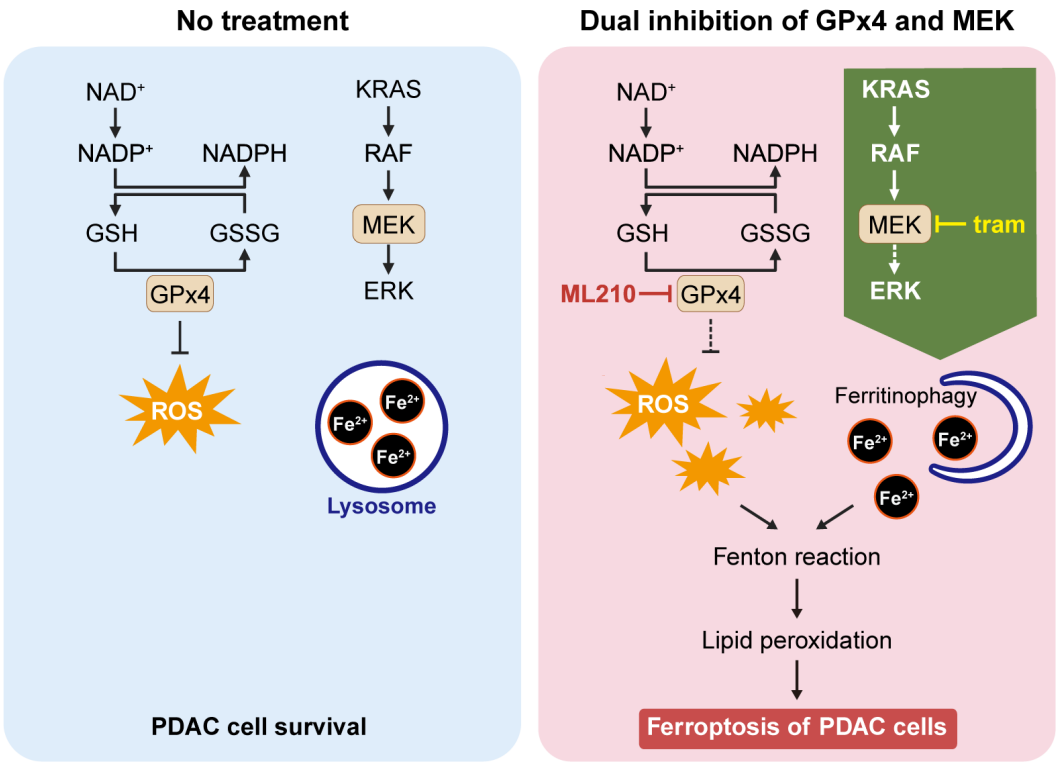

Figure 45. Schematic overview of ferroptosis induction by MT in PDAC cells. PDAC cells harboring oncogenic *KRAS* mutations and elevated GPx4 expression

adapt by enhancing their antioxidant capacity via NAD metabolism, which recycles $NADP^+$ to NADPH. This process maintains redox homeostasis, mitigates the accumulation of toxic ROS, and promotes cell survival. MEK inhibition triggers ferritinophagy (Ravichandran et al., 2022), releasing lysosomal iron, whereas GPx4 inhibition weakens antioxidant defenses. Consequently, dual inhibition of MEK and GPx4 overwhelms the antioxidant response, leading to lipid peroxidation and ferroptotic cell death.

Discussion

In this study, I utilized genetic screening in *Drosophila* to elucidate the pro-tumorigenic role of NAD synthesis pathway, identifying GPx4 as a novel therapeutic target in PDAC. Additionally, combining the GPx4 inhibitor ML210 with the MEK inhibitor drug trametinib exhibited significant anti-tumor effects in mice. Previously, the salvage pathway of NAD synthesis was recognized for its role in PDAC, with overexpression of NAMPT correlating with poor prognosis, suggesting that PDAC cell proliferation is dependent on this pathway (Birnbaum et al., 2017; Ju et al., 2016). NAMPT inhibitors, such as FK866, have been shown to reduce NAD levels and inhibit PDAC cell proliferation (Chini et al., 2014). Additionally, NAD synthesis is crucial for maintaining intracellular redox balance, and inhibiting the production of NADH and NADPH leads to increased oxidative stress (Olivares and Vasseur, 2016), which aligns with my observation of elevated ROS levels and reduced spheroid volume in VB3-deficient AsPC-1 cells. These findings underscore the utility of our strategy, combining *Drosophila* screening with validation in mammals, to identify therapeutic targets in VM, extending beyond protein kinases.

GPx4 is a phospholipid hydroperoxidase that prevents ferroptosis by detoxifying oxidative damage in membrane lipids (Yang et al., 2014). Ferroptosis, an iron-dependent, non-apoptotic form of cell death, is driven by uncontrolled lipid peroxidation and subsequent membrane damage. Inducing ferroptosis can present an attractive therapeutic strategy in PDAC, with particular efficacy against cancer cells that have developed resistance to conventional therapies, such as chemotherapy and radiation. This approach exploits the vulnerability of cancer cells to oxidative damage and disrupts their metabolic processes (Su et al., 2020). Furthermore, the induction of ferroptosis offers a distinct advantage over other forms of cell death by selectively targeting cancer cells while sparing normal cells, making it a compelling avenue for developing novel cancer treatments (Su et al., 2020; Liu et al., 2021a). In previous studies, chemicals such as artesunate (Eling et al., 2015) and zalcitabine (Li et al., 2021)

have been shown to suppress PDAC by inducing ferroptosis. Given GPx4's critical role in inhibiting ferroptosis, it emerges as a promising therapeutic target for PDAC (Li et al., 2023, 2024). Notably, high doses of rapamycin have been shown to induce ferroptosis in pancreatic cancer cells by promoting GPX4 degradation, which in turn inhibits cell proliferation (Liu et al., 2021b). Considering that a phase II trial of FK866 for cutaneous T-cell lymphoma failed due to a lack of remission and severe side effects (Goldinger et al., 2016), targeting GPx4 as a downstream effector of NAD metabolism may represent a more promising therapeutic approach.

On the other hand, cellular injuries like ferroptosis can act as a double-edged sword in PDAC progression. While ferroptosis inducers promote cancer cell deaths (Jiang et al., 2015; Hangauer et al., 2017; Efimova et al., 2020), they may concurrently induce ferroptosis in dendritic cells, T cells, and neutrophils, thereby attenuating anti-tumor immune response (Han et al., 2021; Ma et al., 2021; Kim et al., 2022). Additionally, *GPx4* depletion has been demonstrated to promote *Kras*-driven pancreatic tumorigenesis in immunocompetent mice by enhancing the infiltration of M2-like macrophages within tumor microenvironment (Dai et al., 2020). M2-like macrophages express immunosuppressive signals, emphasizing the necessity to mitigate immune suppression induced by ferroptotic damage in tumor microenvironment. The scRNA-seq analysis in PDAC revealed that myeloid cells may be particularly susceptible to ferroptosis induction. Consequently, N6F11 has emerged as a promising lead compound that selectively induces ferroptosis in cancer cells by promoting GPx4 degradation, while sparing dendritic cells, T lymphocytes, and neutrophils (Li et al., 2023). Furthermore, targeting Macrophage-capping protein (MCP) inhibited both the GPx4 and High mobility group box 1 (HMGB1) pathways, triggering immunogenic ferroptosis to suppress PDAC while promoting the polarization of pro-inflammatory M1-like macrophages (Li et al., 2024). These studies provide strategies to overcome immunosuppression caused by ferroptotic damage when targeting GPx4 in PDAC. Therefore, it is compelling to speculate that combining the MEK inhibitor trametinib with N6F11, or co-targeting MEK and MCP, could offer promising therapeutic

approaches for PDAC. These drug combinations may specifically induce ferroptosis in PDAC cells while preventing immune suppression in the tumor microenvironment. Incorporating immunocompetent models into future investigations will further strengthen the translational relevance of my findings and the proposed therapeutic strategies.

The oncogenic *KRAS* gene is mutated in approximately 85–90% of PDAC cases and serves as the primary driver of pancreatic tumorigenesis (Buscail et al., 2020). Due to the challenges inherent in directly targeting mutant KRAS, the RAF-MEK-ERK signaling axis, the most critical downstream pathway of KRAS, has emerged as a key therapeutic target for PDAC treatment. Our kinome screening in *Ser>4-hit* flies also identified MEK as a crucial target for PDAC treatment, with chemical testing identifying trametinib as a potential therapeutic option (Sekiya et al., 2023; Fukuda et al., 2024). However, the anti-tumor efficacy of MEK inhibitors is frequently hindered by adaptive resistance in RAS-driven tumors (Ahmed et al., 2019). A common approach to overcoming this resistance is to combine MEK inhibitors with other agents that exploit synthetic lethal interactions. In this study, I identified the concurrent targeting of GPx4 and MEK as a novel therapeutic strategy, providing a foundation for leveraging MEK inhibitors to induce ferroptosis in PDAC. Although RAF-MEK-ERK pathway was initially linked to lipid peroxidation (Hattori et al., 2017), my findings revealed that MEK inhibition elevated iron levels in PDAC cells. This suggests that targeting the activated RAF-MEK-ERK signaling may promote iron accumulation in RAS-driven PDAC. On the other hand, a previous study reported that trametinib induced ferritinophagy in PDAC cells, supplying iron to support mitochondrial function and cell survival, suggested that disrupting ferritinophagy through iron chelation could prevent the development of adaptive resistance to MEK inhibitors (Ravichandran et al., 2022). In contrast, I propose an alternative therapeutic strategy that exploits the increased free iron levels resulting from MEK inhibition to sensitize PDAC cells to ferroptosis. The simultaneous inhibition of MEK and GPx4 in PDAC cells resulted in elevated intracellular iron and ROS levels, which may account for the pronounced

ferroptosis observed in this study.

In summary, my findings reveal a new frontier in pancreatic cancer therapeutics by exposing a critical vulnerability in PDAC's redox defenses. By pinpointing GPx4 and MEK as dual targets, I exploit the metabolic dependency of PDAC cells on NAD synthesis pathway and introduce a robust mechanism to induce ferroptotic cell death. Looking forward, the combination of ferroptosis-inducing agents with targeted therapies offers a promising strategy to overcome PDAC's notorious treatment resistance, bringing renewed hope to combat this formidable cancer.

Conclusion

1. New findings in this research.

① Through genetic screening using our *4-hit Drosophila* model, I identified the NAD synthesis pathway as a potential therapeutic vulnerability in PDAC, suggesting new metabolic targets for intervention.

② *GPx4* emerged as a suppressor gene in genetic screening, and the chemical testing demonstrated that combining the GPx4 inhibitor ML210 with the MEK inhibitor trametinib significantly improved survival of the *4-hit* flies.

③ Moreover, I confirmed that the combination of ML210 and trametinib effectively suppresses tumor growth in the AsPC-1 xenograft model, which carries *4-hit* mutations, underscoring the translational potential of this daual inhibition approach.

④ Additionally, I demonstrated that dual inhibition of GPx4 and MEK successfully induces ferroptosis in AsPC-1 cells providing a promising strategy for overcoming resistance to conventional therapies.

⑤ Finally, my study broadens the utility of *Drosophila* platform beyond traditional protein and kinase screening. By demonstrating its applicability in investigating both metabolic and signaling pathways in PDAC, our *Drosophila* model offers a versatile model for exploring complex oncogenic processes and potential therapeutic targets.

2. Significance of the new findings

The dual inhibition of GPx4 and MEK offers a targeted approach for selectively inducing ferroptosis in PDAC cells, addressing a critical therapeutic gap in the treatment of *KRAS*-driven tumors. This approach exploits the metabolic vulnerability of PDAC cells, effectively enhancing oxidative stress and overcoming the antioxidant defenses crucial for PDAC cell survival.

3. Future research based on this study

Regarding the immunosuppressive impact of ferroptosis on immune system,

investigating inhibitors that selectively target tumor cells while sparing immune cells could provide a therapeutic advantage. Hence, future research could explore combining trametinib with compounds specifically targeting GPx4, such as N6F11, to refine dual inhibition strategies and further assess their effects on immune cell populations within the tumor microenvironment. Additionally, research could extend to explore the interaction between ferritinophagy, MEK inhibition, and iron metabolism in PDAC to optimize drug combinations that potentiate ferroptosis.

Acknowledgements

This research was funded by the Japan Society for the Promotion of Science through grants 20H03524, 23H02759, 24K17810, 20K07558, and Takeda Science Foundation. Additional support was provided by the Junior Scientist Promotion and Photo-Excitonix projects at Hokkaido University, the Joint Research Program of the Institute for Genetic Medicine, Hokkaido University, the Suhara Memorial Foundation, and the FY19 Support System for the Interdepartmental Collaborative Research of Young Researchers, Hokkaido University.

I would like to express my deepest gratitude to my supervisor, Professor Masahiro Sonoshita, of the Division of Biomedical Oncology, Institute for Genetic Medicine, Hokkaido University, for his continuous support, guidance, and encouragement throughout my PhD journey. His expertise and insights have greatly shaped both my research and personal development. I am also deeply thankful for his patience and understanding during the challenging phases of this work.

My sincere thanks also go to Assistant Professors Takako Ooshio and Ryodai Yamamura for their invaluable guidance and support. Their instruction in research techniques and their cooperation were crucial to the successful completion of this study.

I am also deeply grateful for the financial support provided by the JST SPRING scholarship (Grant Number JPMJSP2119), which made this research possible.

Finally, I extend my heartfelt appreciation to my family and friends. Their unwavering support and belief in me, especially during difficult times, kept me motivated and focused on completing this journey.

Disclosure of conflicts of interests

The author declares no conflict of interest.

References

Ahmed TA, Adamopoulos C, Karoulia Z, Wu X, Sachidanandam R, Aaronson SA and Poulikakos PI (2019) SHP2 drives adaptive resistance to ERK signaling inhibition in molecularly defined subsets of ERK-dependent tumors. Cell Rep. 26 (1), 65-78.e5.

Bangi E, Ang C, Smibert P, Uzilov AV, Teague AG, Antipin Y, Chen R, Hecht C, Gruszczynski N, Yon WJ, et al. (2019) A personalized platform identifies trametinib plus zoledronate for a patient with KRAS-mutant metastatic colorectal cancer. Sci Adv. 5 (5), eaav6528.

Bangi E, Smibert P, Uzilov AV, Teague AG, Gopinath S, Antipin Y, Chen R, Hecht C, Gruszczynski N, Yon WJ, et al. (2021) A Drosophila platform identifies a novel, personalized therapy for a patient with adenoid cystic carcinoma. iScience. 24 (3), 102212.

Barile M, Giancaspero TA, Leone P, Galluccio M and Indiveri C (2016) Riboflavin transport and metabolism in humans. J Inherit Metab Dis. 39 (4), 545–557.

Bier E (2005) Drosophila, the golden bug, emerges as a tool for human genetics. Nat Rev Genet. 6 (1), 9–23.

Birnbaum DJ, Finetti P, Lopresti A, Gilabert M, Poizat F, Raoul J-L, Delpero J-R, Moutardier V, Birnbaum D, Mamessier E, et al. (2017) A 25-gene classifier predicts overall survival in resectable pancreatic cancer. BMC Med. 15 (1).

Buscail L, Bournet B and Cordelier P (2020) Role of oncogenic KRAS in the diagnosis, prognosis and treatment of pancreatic cancer. Nat Rev Gastroenterol Hepatol. 17 (3), 153–168.

Caunt CJ, Sale MJ, Smith PD and Cook SJ (2015) MEK1 and MEK2 inhibitors and cancer therapy: the long and winding road. Nat Rev Cancer. 15 (10), 577–592.

Chen C-C, Li B, Millman SE, Chen C, Li X, Morris JP 4th, Mayle A, Ho Y-J, Loizou E, Liu H, et al. (2020) Vitamin B6 addiction in acute myeloid leukemia. Cancer Cell. 37 (1), 71-84.e7.

Chini CCS, Guerrico AMG, Nin V, Camacho-Pereira J, Escande C, Barbosa MT and Chini EN (2014) Targeting of NAD metabolism in pancreatic cancer cells: Potential novel therapy for pancreatic tumors. Clin Cancer Res. 20 (1), 120–130.

Conroy T, Desseigne F, Ychou M, Bouché O, Guimbaud R, Bécouarn Y, Adenis A, Raoul J-L, Gourgou-Bourgade S, de la Fouchardière C, et al. (2011) FOLFIRINOX versus Gemcitabine for Metastatic Pancreatic Cancer. N Engl J Med. 364 (19), 1817–1825.

Dai E, Han L, Liu J, Xie Y, Zeh HJ, Kang R, Bai L and Tang D (2020) Ferroptotic damage promotes pancreatic tumorigenesis through a TMEM173/STING-dependent DNA sensor pathway. Nat Commun. 11 (1).

Dar AC, Das TK, Shokat KM and Cagan RL (2012) Chemical genetic discovery of targets and anti-targets for cancer polypharmacology. Nature. 486 (7401), 80–84.

DeNicola GM, Karreth FA, Humpton TJ, Gopinathan A, Wei C, Frese K, Mangal D, Yu KH, Yeo CJ, Calhoun ES, et al. (2011) Oncogene-induced Nrf2 transcription promotes ROS detoxification and tumorigenesis. Nature. 475 (7354), 106–109.

Duffy JB (2002) GAL4 system in Drosophila: a fly geneticist's Swiss army knife. Genesis. 34 (1–2), 1–15.

Eaton JK, Furst L, Ruberto RA, Moosmayer D, Hilpmann A, Ryan MJ, Zimmermann K, Cai LL, Niehues M, Badock V, et al. (2020) Selective covalent targeting of GPX4 using masked nitrile-oxide electrophiles. Nat Chem Biol. 16 (5), 497–506.

Efimova I, Catanzaro E, Van der Meeren L, Turubanova VD, Hammad H, Mishchenko TA, Vedunova MV, Fimognari C, Bachert C, Coppieters F, et al. (2020) Vaccination with early ferroptotic cancer cells induces efficient antitumor immunity. J Immunother Cancer. 8 (2), e001369.

Eling N, Reuter L, Hazin J, Hamacher-Brady A and Brady NR (2015) Identification of artesunate as a specific activator of ferroptosis in pancreatic cancer cells. Oncoscience. 2 (5), 517–532.

Fukuda J, Kosuge S, Satoh Y, Sekiya S, Yamamura R, Ooshio T, Hirata T, Sato R,

Hatanaka KC, Mitsuhashi T, et al. (2024) Concurrent targeting of GSK3 and MEK as a therapeutic strategy to treat pancreatic ductal adenocarcinoma. Cancer Sci. 00, 1–13.

Fukuwatari T and Shibata K (2007) Effect of nicotinamide administration on the tryptophan-nicotinamide pathway in humans. Int J Vitam Nutr Res. 77 (4), 255–262.

Galluzzi L, Vacchelli E, Michels J, Garcia P, Kepp O, Senovilla L, Vitale I and Kroemer G (2013) Effects of vitamin B6 metabolism on oncogenesis, tumor progression and therapeutic responses. Oncogene. 32 (42), 4995–5004.

Goldinger SM, Gobbi Bischof S, Fink-Puches R, Klemke C-D, Dréno B, Bagot M and Dummer R (2016) Efficacy and safety of APO866 in patients with refractory or relapsed cutaneous T-cell lymphoma: A phase 2 clinical trial. JAMA Dermatol. 152 (7), 837–839.

Halbrook CJ, Lyssiotis CA, Pasca di Magliano M and Maitra A (2023) Pancreatic cancer: Advances and challenges. Cell. 186 (8), 1729–1754.

Han L, Bai L, Qu C, Dai E, Liu J, Kang R, Zhou D, Tang D and Zhao Y (2021) PPARG-mediated ferroptosis in dendritic cells limits antitumor immunity. Biochem Biophys Res Commun. 576, 33–39.

Hangauer MJ, Viswanathan VS, Ryan MJ, Bole D, Eaton JK, Matov A, Galeas J, Dhruv HD, Berens ME, Schreiber SL, et al. (2017) Drug-tolerant persister cancer cells are vulnerable to GPX4 inhibition. Nature. 551 (7679), 247–250.

Hattori K, Ishikawa H, Sakauchi C, Takayanagi S, Naguro I and Ichijo H (2017) Cold stress-induced ferroptosis involves the ASK1-p38 pathway. EMBO Rep. 18 (11), 2067–2078.

Hingorani SR, Petricoin EF, Maitra A, Rajapakse V, King C, Jacobetz MA, Ross S, Conrads TP, Veenstra TD, Hitt BA, et al. (2003) Preinvasive and invasive ductal pancreatic cancer and its early detection in the mouse. Cancer Cell. 4 (6), 437–450.

Hingorani SR, Wang L, Multani AS, Combs C, Deramaudt TB, Hruban RH, Rustgi AK, Chang S and Tuveson DA (2005) Trp53R172H and KrasG12D cooperate to promote chromosomal instability and widely metastatic pancreatic ductal adenocarcinoma in

mice. Cancer Cell. 7 (5), 469–483.

Illés E, Patra SG, Marks V, Mizrahi A and Meyerstein D (2020) The FeII(citrate) Fenton reaction under physiological conditions. J Inorg Biochem. 206 (111018), 111018.

Jiang H, Kimura T, Hai H, Yamamura R and Sonoshita M (2022) Drosophila as a toolkit to tackle cancer and its metabolism. Front Oncol. 12, 982751.

Jiang L, Kon N, Li T, Wang S-J, Su T, Hibshoosh H, Baer R and Gu W (2015) Ferroptosis as a p53-mediated activity during tumour suppression. Nature. 520 (7545), 57–62.

Ju H-Q, Zhuang Z-N, Li H, Tian T, Lu Y-X, Fan X-Q, Zhou H-J, Mo H-Y, Sheng H, Chiao PJ, et al. (2016) Regulation of the Nampt-mediated NAD salvage pathway and its therapeutic implications in pancreatic cancer. Cancer Lett. 379 (1), 1–11.

Karim FD and Rubin GM (1998) Ectopic expression of activated Ras1 induces hyperplastic growth and increased cell death in Drosophila imaginal tissues. Development. 125 (1), 1–9.

Kim R, Hashimoto A, Markosyan N, Tyurin VA, Tyurina YY, Kar G, Fu S, Sehgal M, Garcia-Gerique L, Kossenkov A, et al. (2022) Ferroptosis of tumour neutrophils causes immune suppression in cancer. Nature. 612 (7939), 338–346.

Kincaid JWR and Berger NA (2020) NAD metabolism in aging and cancer. Exp Biol Med (Maywood). 245 (17), 1594–1614.

Kleeff J, Korc M, Apte M, La Vecchia C, Johnson CD, Biankin AV, Neale RE, Tempero M, Tuveson DA, Hruban RH, et al. (2016) Pancreatic cancer. Nat Rev Dis Primers. 2 (1).

Lam Wong KK and Verheyen EM (2021) Metabolic reprogramming in cancer: mechanistic insights from Drosophila. Dis Model Mech.

Lei G, Zhuang L and Gan B (2024) The roles of ferroptosis in cancer: Tumor suppression, tumor microenvironment, and therapeutic interventions. Cancer Cell. 42

(4), 513–534.

Levine BD and Cagan RL (2016) Drosophila Lung Cancer Models Identify Trametinib plus Statin as Candidate Therapeutic. Cell Rep. 14 (6), 1477–1487.

Li C, Yin X, Liu Z and Wang J (2022) Emerging Potential Mechanism and Therapeutic Target of Ferroptosis in PDAC: A Promising Future. Int J Mol Sci. 23 (23).

Li C, Zhang Y, Liu J, Kang R, Klionsky DJ and Tang D (2021) Mitochondrial DNA stress triggers autophagy-dependent ferroptotic death. Autophagy. 17 (4), 948–960.

Li G, Liao C, Chen J, Wang Z, Zhu S, Lai J, Li Q, Chen Y, Wu D, Li J, et al. (2024) Targeting the MCP‐GPX4/HMGB1 Axis for Effectively Triggering Immunogenic Ferroptosis in Pancreatic Ductal Adenocarcinoma. Advanced Science. 11 (21).

Li J, Liu J, Zhou Z, Wu R, Chen X, Yu C, Stockwell B, Kroemer G, Kang R and Tang D (2023) Tumor-specific GPX4 degradation enhances ferroptosis-initiated antitumor immune response in mouse models of pancreatic cancer. Sci Transl Med. 15 (720), eadg3049.

Lienhart W-D, Gudipati V and Macheroux P (2013) The human flavoproteome. Arch Biochem Biophys. 535 (2), 150–162.

Liu J, Kang R and Tang D (2021a) The art of war: Ferroptosis and pancreatic cancer. Front Pharmacol. 12.

Liu Y, Wang Y, Liu J, Kang R and Tang D (2021b) Interplay between MTOR and GPX4 signaling modulates autophagy-dependent ferroptotic cancer cell death. Cancer Gene Ther. 28 (1–2), 55–63.

Luchini C, Brosens LAA, Wood LD, Chatterjee D, Shin JI, Sciammarella C, Fiadone G, Malleo G, Salvia R, Kryklyva V, et al. (2021) Comprehensive characterisation of pancreatic ductal adenocarcinoma with microsatellite instability: histology, molecular pathology and clinical implications. Gut. 70 (1), 148–156.

Ma X, Xiao L, Liu L, Ye L, Su P, Bi E, Wang Q, Yang M, Qian J and Yi Q (2021) CD36-mediated ferroptosis dampens intratumoral CD8+ T cell effector function and

impairs their antitumor ability. Cell Metab. 33 (5), 1001-1012.e5.

Moore MJ, Goldstein D, Hamm J, Figer A, Hecht JR, Gallinger S, Au HJ, Murawa P, Walde D, Wolff RA, et al. (2007) Erlotinib plus gemcitabine compared with gemcitabine alone in patients with advanced pancreatic cancer: a phase III trial of the National Cancer Institute of Canada Clinical Trials Group. J Clin Oncol. 25 (15), 1960–1966.

Morris JP 4th, Wang SC and Hebrok M (2010) KRAS, Hedgehog, Wnt and the twisted developmental biology of pancreatic ductal adenocarcinoma. Nat Rev Cancer. 10 (10), 683–695.

Olivares O and Vasseur S (2016) Metabolic rewiring of pancreatic ductal adenocarcinoma: New routes to follow within the maze. Int J Cancer. 138 (4), 787–796.

Ooshio T, Satoh Y, Jiang H, Liu T, Fujii K, Ishikawa T, Igarashi K, Saitoh K, Kato K, Mashima T, et al. (2024) Identifying simultaneous inhibition of riboflavin metabolism and MEK as a novel therapeutic strategy for pancreatic cancer. *bioRxiv*.

Pandey U and Nichols C (2011) Human disease models in Drosophila melanogaster and the role of the fly in therapeutic drug discovery. Pharmacol Rev. 63, 411–436.

Pinto JT and Zempleni J (2016) Riboflavin. Adv Nutr. 7 (5), 973–975.

Qian ZR, Rubinson DA, Nowak JA, Morales-Oyarvide V, Dunne RF, Kozak MM, Welch MW, Brais LK, Da Silva A, Li T, et al. (2018) Association of alterations in main driver genes with outcomes of patients with resected pancreatic ductal adenocarcinoma. JAMA Oncol. 4 (3), e173420.

Rahib L, Wehner MR, Matrisian LM and Nead KT (2021) Estimated projection of US cancer incidence and death to 2040. JAMA Netw Open. 4 (4), e214708.

Ravichandran M, Hu J, Cai C, Ward NP, Venida A, Foakes C, Kuljanin M, Yang A, Hennessey CJ, Yang Y, et al. (2022) Coordinated transcriptional and catabolic programs support iron-dependent adaptation to RAS-MAPK pathway inhibition in pancreatic cancer. *Cancer discovery*.12 (9) pp.2198–2219.

Richardson H, O'Keefe LV, Marty T and Saint R (1995) Ectopic cyclin E expression induces premature entry into S phase and disrupts pattern formation in the Drosophila eye imaginal disc. Development. 121 (10), 3371–3379.

Sams-Dodd F (2005) Target-based drug discovery: is something wrong? Drug Discov Today. 10 (2), 139–147.

Sekiya S, Fukuda J, Yamamura R, Ooshio T, Satoh Y, Kosuge S, Sato R, Hatanaka KC, Hatanaka Y, Mitsuhashi T, et al. (2023) Drosophila screening identifies dual inhibition of MEK and AURKB as an effective therapy for pancreatic ductal adenocarcinoma. Cancer Res. 83 (16), 2704–2715.

Siegel RL, Miller KD, Wagle NS and Jemal A (2023) Cancer statistics, 2023. CA Cancer J Clin. 73 (1), 17–48.

Sonoshita M, Scopton AP, Ung PMU, Murray MA, Silber L, Maldonado AY, Real A, Schlessinger A, Cagan RL and Dar AC (2018) A whole-animal platform to advance a clinical kinase inhibitor into new disease space. Nat Chem Biol. 14 (3), 291–298.

Su Y, Zhao B, Zhou L, Zhang Z, Shen Y, Lv H, AlQudsy LHH and Shang P (2020) Ferroptosis, a novel pharmacological mechanism of anti-cancer drugs. Cancer Lett. 483, 127–136.

Sung H, Ferlay J, Siegel RL, Laversanne M, Soerjomataram I, Jemal A and Bray F (2021) Global Cancer Statistics 2020: GLOBOCAN Estimates of Incidence and Mortality Worldwide for 36 Cancers in 185 Countries. CA Cancer J Clin. 71 (3), 209–249.

Tham HP, Xu K, Lim WQ, Chen H, Zheng M, Thng TGS, Venkatraman SS, Xu C and Zhao Y (2018) Microneedle-assisted topical delivery of photodynamically active mesoporous formulation for combination therapy of deep-seated melanoma. ACS Nano. 12 (12), 11936–11948.

Ung PMU, Sonoshita M, Scopton AP, Dar AC, Cagan RL and Schlessinger A (2019) Integrated computational and Drosophila cancer model platform captures previously unappreciated chemicals perturbing a kinase network. PLoS Comput Biol. 15 (4),

e1006878.

Varghese F, Bukhari AB, Malhotra R and De A (2014) IHC Profiler: an open source plugin for the quantitative evaluation and automated scoring of immunohistochemistry images of human tissue samples. PLoS One. 9 (5), e96801.

Vidal M, Wells S, Ryan A and Cagan R (2005) ZD6474 suppresses oncogenic RET isoforms in a Drosophila model for type 2 multiple endocrine neoplasia syndromes and papillary thyroid carcinoma. Cancer Res. 65 (9), 3538–3541.

Von Hoff DD, Ervin T, Arena FP, Chiorean EG, Infante J, Moore M, Seay T, Tjulandin SA, Ma WW, Saleh MN, et al. (2013) Increased Survival in Pancreatic Cancer with nab-Paclitaxel plus Gemcitabine. N Engl J Med. 369 (18), 1691–1703.

Werba G, Weissinger D, Kawaler EA, Zhao E, Kalfakakou D, Dhara S, Wang L, Lim HB, Oh G, Jing X, et al. (2023) Single-cell RNA sequencing reveals the effects of chemotherapy on human pancreatic adenocarcinoma and its tumor microenvironment. Nat Commun. 14 (1), 797.

Wu H, Gonzalez Villalobos R, Yao X, Reilly D, Chen T, Rankin M, Myshkin E, Breyer MD and Humphreys BD (2022) Mapping the single-cell transcriptomic response of murine diabetic kidney disease to therapies. Cell Metab. 34 (7), 1064-1078.e6.

Wu M, Wu L, Wu W, Zhu M, Li J, Wang Z, Li J, Ding R, Liang Y, Li L, et al. (2023) Phagocytosis of glioma cells enhances the immunosuppressive phenotype of bone marrow-derived macrophages. Cancer Res. 83 (5), 771–785.

Xie Y, Hou W, Song X, Yu Y, Huang J, Sun X, Kang R and Tang D (2016) Ferroptosis: process and function. Cell Death Differ. 23 (3), 369–379.

Xu X, Zhang X, Lin Q, Qin Y, Liu Y and Tang W (2023) Integrated single-cell and bulk RNA sequencing analysis identifies a prognostic signature related to ferroptosis dependence in colorectal cancer. Sci Rep. 13 (1), 12653.

Xue Q, Yan D, Chen X, Li X, Kang R, Klionsky DJ, Kroemer G, Chen X, Tang D and Liu J (2023) Copper-dependent autophagic degradation of GPX4 drives ferroptosis. Autophagy. 19 (7), 1982–1996.

Yaku K, Okabe K, Hikosaka K and Nakagawa T (2018) NAD metabolism in cancer therapeutics. Front Oncol. 8, 622.

Yamamura R, Ooshio T and Sonoshita M (2021) Tiny Drosophila makes giant strides in cancer research. Cancer Sci. 112 (2), 505–514.

Yang WS, SriRamaratnam R, Welsch ME, Shimada K, Skouta R, Viswanathan VS, Cheah JH, Clemons PA, Shamji AF, Clish CB, et al. (2014) Regulation of ferroptotic cancer cell death by GPX4. Cell. 156 (1–2), 317–331.

Yang Y and Sauve AA (2016) NAD + metabolism: Bioenergetics, signaling and manipulation for therapy. Biochim Biophys Acta Proteins Proteom. 1864 (12), 1787–1800.

Zarkovic N (2003) 4-hydroxynonenal as a bioactive marker of pathophysiological processes. Mol Aspects Med. 24 (4–5), 281–291.

Zhang X, Sui S, Wang L, Li H, Zhang L, Xu S and Zheng X (2020) Inhibition of tumor propellant glutathione peroxidase 4 induces ferroptosis in cancer cells and enhances anticancer effect of cisplatin. J Cell Physiol. 235 (4), 3425–3437.

Zhao Y, Li Y, Zhang R, Wang F, Wang T and Jiao Y (2020) The role of erastin in ferroptosis and its prospects in cancer therapy. Onco Targets Ther. 13, 5429–5441.

Zheng Y, Lin T-Y, Lee G, Paddock MN, Momb J, Cheng Z, Li Q, Fei DL, Stein BD, Ramsamooj S, et al. (2018) Mitochondrial one-carbon pathway supports cytosolic folate integrity in cancer cells. Cell. 175 (6), 1546-1560.e17.